공학박사 학위논문

Single-layer metasurfaces for full-space optical phase modulation

단층 메타표면을 통한 전 공간 광 위상 제어

2021 년 8 월

서울대학교 대학원

전기정보공학부

성 장 운

Single-layer metasurfaces for full-space optical phase modulation

지도 교수 이 병 호

이 논문을 공학박사 학위논문으로 제출함
2021 년 8 월

서울대학교 대학원
전기정보공학부
성 장 운

성장운의 공학박사 학위논문을 인준함
2021 년 8 월

위 원 장 _____

부위원장 _____

위 원 _____

위 원 _____

위 원 _____

Abstract

Single-layer metasurfaces for full-space optical phase modulation

Jangwoon Sung
Department of Electrical and Computer Engineering
College of Engineering
Seoul National University

Metasurfaces have received enormous attention thanks to their unique ability to modulate electromagnetic properties of light even in various frequency regimes. In recent years, exploiting their potentials of fabrication ease and modulation strength, unprecedented and unique controlling of light that surpasses conventional optical devices has been suggested so far. They are providing new paradigm for optical system thanks to not only their planar form factor, but their outgoing ability of light control compared to the bulk optic components. Considering that the current wearable devices and smart devices require lighter and better optical devices, it is no exaggeration to say that we cannot talk about future optical devices without them.

In this regard, this dissertation presents the metasurfaces designed to control the phases at both the transmission and reflection spaces. Compared to the conventional metasurfaces that consider only transmitted or reflected light from metasurfaces, this proposed platform enhances the information capacity of metasurface into full-space. Therefore, it can be regarded as a new paradigm in metasurface design and system design as well. Contrary to the

intuitive point of view, it is designed to independently control the scattered light in full-space, especially the phase of light imparted into two spaces, with a single layer and a simple structured metasurface.

In this dissertation, total three platforms are introduced. Firstly, a novel metasurface that enables full-space light control is realized, offering an unconventional functionality that provides a new foothold for metasurface integration in optics. Multipolar interference and Pancharatnam–Berry phase are combined with each other and suggested as a physical background for the proposed device. As an example of the functionality, asymmetric beam steering and hologram generation are proposed and measured experimentally. To author's knowledge, this is the first work achieving independent phase control of full-space in visible range.

Secondly, a metasurface platform consisting of interleaved L-shaped meta-atoms is presented. Basically, this metasurface is designed to operate by Pancharatnam-Berry phase (controlled by incident circularly polarized light) as above and transmits different phase values in the transmission and reflection directions. In addition, when the polarization handedness of the incident light is altered, the phases transmitted in each direction are designed to reverse each other, which, to author's knowledge, has never been proposed before.

Finally, the author presents a design method that enables polarization-dependent full-space control, in which two independent and arbitrary phase profiles can be addressed to each space. Upon introducing a phase gradient value to realize the critical angle condition, conversion of transmissive into reflective operation is realized. Then, rectangular nanopillars are utilized to

facilitate polarization beam splitting with the desired phase. Three samples were fabricated and measured based on the proposed scheme.

In conclusion, this full-space control is meaningful in three ways: 1) it showed an unprecedented control method that is possible only through metasurfaces, 2) increased the amount of information that metasurfaces can have, and 3) showed potential for future optical devices through new control.

Keywords: metasurface, full-space control, phase modulation, nanostructure, space conversion, polarization control
Student Number: 2016-20921

Contents

Abstract ..... **i**

Contents ..... **iv**

List of Tables ..... **vi**

List of Figures ..... **vii**

Chapter 1 Introduction **1**

1.1 Overview of metasurfaces for optical modulation 1

1.2 Motivation of this dissertation: metasurface for full-space control 4

1.3 Scope and Organization 9

Chapter 2 Simultaneous full-space visible light control **12**

2.1 Introduction 12

2.2 Metasurface design 15

2.2.1 Design strategy and numerically calculated results 15

2.2.2 Determined structure and numerical demonstration 19

2.3 Experimental demonstration 27

2.3.1 Experimental setup and fabrication 27

2.3.2 Asymmetric beam deflection 30

2.3.3 Asymmetric hologram generation 34

2.4 Conclusion 37

Chapter 3 Polarization dependent space conversion with L-shaped meta-atom **38**

3.1 Introduction 38

3.2 L-shaped meta-atom for space conversion 40

3.3 Simulation results 46

3.3.1 determined parameters and multipole decomposition 46

3.3.2 Polarization-dependent phase behavior of LSMA 51

3.4 Experimental demonstration 54
3.4.1 Unit cell determination 54
3.4.2 Hologram generation and beam deflection using LSMA 57
3.5 Conclusion 61

Chapter 4 Switching modulated space by arbitrary polarization pair 62

4.1 Introduction 62
4.2 Basic metasurface design 64
4.3 Phase gradient metasurface for reflective operation 70
4.4 Experimental demonstration 79
4.5 Conclusion 87

Chapter 5 Conclusion 89

Bibliography 94

Appendix 101

List of Table

Table 2.1 Mapped structural parameters of beam deflection case 1 for w_1.....31

Table 2.2 Mapped structural parameters of beam deflection case 1 for w_2.....31

Table 2.3 Mapped structural parameters of beam deflection case 1 for θ.....31

Table 2.4 Mapped structural parameters of beam deflection case 2 31

Table 2.5 Hologram conversion efficiency (unit: %) calculated from numerical result.....36

Table 4.1 Total diffraction efficiency obtained with FDTD results. a) El_1 (El_2) is the elliptical polarization state determined to operate in transmission (reflection). b) Written in bracket is the efficiency at target diffraction order. 82

Table 4.2 Numerically retrieved hologram conversion efficiency.....86

List of Figures

Figure 1.1 Conceptual diagram of metasurface and its unit, meta-atom.....1

Figure 1.2 Diagram showing two major operations of conventional metasurfaces 4

Figure 1.3 Diagram showing the definition of proposed metasurface with respect to the comparison with conventional full-space control 8

Figure 1.4 Schematic operation for comparison of each chapter. From left to right, described ones are Chapter 2, 3 and 4. Blue and red colors are for expression of distinct imparted phase values. Note that in Chapter 4, arbitrary polarization pair can be adopted for same kind of function. 9

Figure 2.1 Diagram showing Kerker effect. (a) When the ED mode and MD mode exist with equal magnitude, it is possible to generate a scattering source that has no backscattering. That stems from the disparity of phase symmetry of each mode: ED has even parity, and MD has odd parity. (b) Generalized Kerker effect as the proposed scheme in this paper. If it is possible to generate arbitrary values for even and odd parity, it contributes to modulation of phase difference between transmission and reflection spaces. 15

Figure 2.2 Schematic diagram showing building blocks. It is composed of amorphous silicon nanopillar array fabricated on commercial quartz wafer. Lower diagram shows structural parameter of meta-atom as well as the simulation space used when obtaining phase difference value. 19

Figure 2.3 (a) The simulation space used for multipolar decomposition (b) Colored map and black arrows expressing induced current density for four selected parameters. Left four blue plots show current density when x-polarized light is incident while right reds are resulted from y-polarized light incidence. Scale bar: 100 nm 21

Figure 2.4 (a) Effective amplitudes by bar graph, which denote contributions of each multipole mode with l being less than three. (b) Bar graph shows effective efficiency, which is calculated by adding each mode by parity, then squaring. (c) Complex plane showing E_{even}, E_{odd}, transmission and reflection coefficients expressed by colored arrows. 22

Figure 2.5 Dot graph showing phase difference value calculated by numerical result (red circle) and multipole expansion (blue triangle).....22

Figure 2.6 Colored map showing structural parameters of a) w_1, b) w_2, and c) θ of which meta-atom imparts desired phases to transmission and reflection spaces. Structural parameters are calculated numerically in periodic boundary condition when right CP wave is incident from bottom of the structure. As an example, for desired phase of 4 and 2 rad each at transmission and reflection spaces, a structural parameter set of (230 nm, 115 nm, 165°) is obtained by the same positions on these three graphs (marked with gray diamonds). 23

Figure 2.7 Line graph denoting structural parameters with respect to phase difference of transmission and reflection. 24

Figure 2.8 Dispersive characteristics of selected meta-atoms. (a–d) Transmission and reflection spectra of conversion efficiency for selected parameters of dashed squares from above graphs. Here conversion efficiency stands for the cross-polarized components scattered by incident CP wave. Inset shows the top view of the structures. Red and blue circles are conversion efficiency of transmission and reflection in target wavelength. (e) Phase difference between transmitted and reflecte light for four selected parameters. Gray vertical line is located at 660 nm, showing identical phase difference. 26

Figure 2.9 Fabrication process with simplified explanation 27

Figure 2.10 Measurement setup for proposed metasurface. (a) 2-f setup for capturing beam deflection images (b) 4-f setup for holographic image retrieval. Pol: polarizer (circular) BS: beam splitter, MS: metasurface, CCD: charge coupled device 28

Figure 2.11 Conceptual illustration of the first device which deflects transmitted wave into +*y*-direction, while it sends reflected one to +*x*-direction. (b) Fabrication result for the first deflection device. Scale bar: 400 nm 30

Figure 2.12 (a, b) Experimental result showing intensity captured by CCD camera as well as the line graph expressing the intensity value of desired diffraction orders. 32

Figure 2.13 Conceptual diagram for the second device that induces the transmitted wave direction into the first diffraction order and reflected wave to the minus second diffraction order. (b) Fabricated second device sample. Scale bar: 800 nm. 32

Figure 2.14 Experimental result showing intensity captured by CCD camera as well as the line graph expressing the intensity value of desired diffraction orders and unwanted one together. (a) is captured in transmission space, and (b) is in reflection space. 33

Figure 2.15 Illustrations of Fresnel-type hologram generation via proposed metasurface. It shows the operation of hologram generating device possessing two faces. 34

Figure 2.16 (a) Phase profile of each face obtained by ASM. (b) Fabricated sample captured in CCD. Scale bar: 400 nm. 34

Figure 2.17 Amplitude profile of (a) transmission and (b) reflection space. Upper eight images are numerical results by ASM, while lower eight images are captured by CCD camera. Scale bar: 30 μm 35

Figure 3.1 Schematic diagram showing operation of single LSMA and its structural parameters 41

Figure 3.2 Schematic diagram showing one example of LSMA and its enantiomeric counterpart. Lower two field distributions show when x-polarized wave is used as excitation source. Black arrows show the vector expression of induced current distribution. Scale bar: 100 nm 43

Figure 3.3 Schematic diagram for explanation of the role of LSMA (a) Comparison of a LSMA and its enantiomeric counterpart. Scattered light in red color is the resultant light from + polarized light, while blue colors are scattered light when – polarized light is illuminated. (b) Interleaved case and its corresponded operation by polarization. The phase by angle θ (φ) is at transmission (reflection) space when + polarized light is illuminating source and when it is changed to – polarization, the phase by angle θ (φ) proceed to reflection (transmission) space. 44

Figure 3.4 (a) Line plots showing cross-polarized component of transmission (left) and reflection (right) spectrum altered by incident handedness of circular polarization. (b) Extinction ratio spectra of transmission and reflection, respectively. In terms of transmission, it is ratio of – to + polarization, while in reflection, it is ratio of efficiency of cross-polarized light by + to – polarized light. Shadowed region is marked for extinction ratio larger than 10 dB.....46

Figure 3.5 (a) Line plots showing absolute values of electric fields by each multipole modes. Left (right) is the result when + (-) polarized light is used as excitation source. (b) Complex plane expression of each multipole mode except for octupole modes when the wavelength of source is 633 nm. The sum of modes having even and odd parity each is also shown for clarity.....48

Figure 3.6 Schematic diagram for clear understanding of four selected multipole modes by the representative rectangular nanopillar. Note that the

black arrows indicate the desired induced current for outcoupled *y*-polarized wave at each multipole modes. If necessary, in addition to the *yz* cross section, *xy* plane expression is provided.....51

Figure 3.7 Complex plane expression of four dominant multipole modes (a) Expression of the fields decomposed when linearly polarized wave is excitation source. (b) Multipole modes that show the contribution to the cross-polarized terms when circularly polarized light impinges, calculated from upper line result. The field by the handedness of polarization is shown together. 52

Figure 3.8 Representative SEM image with schematics shows the unit cell of the structure. The yellow dotted rectangle is unit cell and repeated left and right and up and down to form final device. Scale bar: 550 nm 54

Figure 3.9 Schematic illustration for the experimental demonstration of proposed metasurface. Pol: polarizer, BS: beam splitter, MS: metasurface.55

Figure 3.10 (a) schematic diagram showing electric field distribution varied by incident light direction and rotation angle. (b) Reflection and transmission curve by rotation angle of LSMA. 56

Figure 3.11 Hologram generation using proposed metasurface. (a) Schematic diagram showing operation of sample for hologram generation (b) Phase profiles for “ABCD” (left) and “abcd” (right), respectively, retrieved by GS algorithm. (c) Experimental results using sample for hologram. Upper two images are from transmission space, and lower two are from reflection spaces. White arrows indicates the input polarization of incident light.....57

Figure 3.12 CCD-captured images varied by the wavelength of incident light.....58

Figure 3.13 (a) Schematic diagram showing the operation of the beam deflection sample by proposed scheme. The polarization sensitive operation

is shown by color differentiation: when the source is LCP (RCP), it is blue (red). (b) SEM images of fabricated sample. The LSMA and its enantiomeric counterpart show different direction-dependent rotating property. Scale bar: 500 nm. (c) Line plot showing SNR varied by wavelengths. Each plot graphs are retrieved in transmission and reflection spaces, respectively. (d) CCD captured results distinguished by space and input polarization. Upper two are results in transmission, and lower two are in reflection. Dotted yellow circles are for clarification of desired diffraction order. 59

Figure 4.1 Schematic diagram and transmission coefficients of nanopillar, which is used as unit structure throughout this article. (a) Schematic diagram of rectangular nanopillar expressed with structural parameters. The structure is illuminated from the bottom. (b) Schematic diagram and SEM captured image showing how the meta-atom is structured and made in simulation and experiment. (c) Simulation results of amplitude and phase of transmission T_{xx}, while varying L_x and L_y of single nanopillar. 64

Figure 4.2 Structural parameter and amplitude data set used in the main text sorted by the desired phase values of T_{xx} and T_{yy}. (a) Colored plot graphs of structural values of L_x and L_y. Coordinate values indicate the lengths of corresponded phase values of T_{xx} and T_{yy}. (b) Colored plot graphs of amplitudes, corresponding to the Fig. 4.2a. 65

Figure 4.3 Conceptual schematic for explanation of mechanism of phase modulation of arbitrary polarization pair. When the nanopillar rotation is introduced, the phase modulation at arbitrary polarization pair is possible with flipped handedness as described in the text. 67

Figure 4.4 Conceptual diagrams of proposed phase gradient metasurfaces for explanation of mechanism of desired scheme. (a) Schematic illustration of transmissive PGM consisting of two meta-atoms (m=2). The period of supercell is a, assuming that the meta-atom is transmissive and having

gradient value of $2\pi/a$, the light is bent by addition of corresponding momentum as shown. (b) Schematic illustration for showing transmissive PGM of m=2 and phase behavior when the direct transmission (L=1) and induced reflection (L=2) appear. 70

Figure 4.5 Procedure of how diffraction occurs when critical angle condition is met. (a) The condition when the diffraction can be explained with GSL. (b) Equifrequency contour. From bottom, the light is normally illuminating to structure, yielding anomalous refraction. (c) Schematic of obliquely incident light when critical angle condition is met. (d) Equifrequency contour described by GSL. (e) Schematic diagram showing the induced reflection. (f) Corresponded equifrequency contour.....72

Figure 4.6 The equifrequency contours of PGM when a=2P. Red circles are transmission contour graphs and the green circles are the reflection contours. The solid (dashed) circles are coupling-possible (-impossible) contours of diffraction orders solved by eq. 4.10. The blue arrows show the directions of incident and output light. Since the surroundings are different at transmission and reflection spaces, the radii of contours differ from each other.....74

Figure 4.7 Simulated results showing the induced reflection. (a) The light field intensity patterns from ten selected structural parameter sets. The electric field is directed in y. The interference pattern shows the light is mostly reflected. The square nanopillars in one set have phase values that are out-of-phase to each other, which means identical phase gradient. Their original phase values in transmission can be observed in (b), and they are increasing values maintaining identical phase gradient. Green triangles are phase values from right nanopillar, and red circles are from left. The reflected phase values of (i-x) are also shown in black squares, which are two times of the transmissive phase shift. (c) Transmission and reflection

amplitudes from (i-x). Red squares are reflection and green circles are transmission.....75

Figure 4.8 Schematic diagram and colored plot graphs for explanation of reflected phase values designed in linear polarization pair. (a) Schematic diagram of two-fold meta-atom unit cell design, and scattered wavefronts from each meta-atom is marked by yellow-colored circle and triangle, respectively. (b) Examples of structural parameters of two meta-atoms exhibiting transmission at *x*-polarized shined condition, and reflection at *y*-polarized shining. They should meet the condition of out-of-phase condition at T_{yy}, while T_{xx}s are in-phase. As results, line that passes circle and triangle both is parallel to *y*-axis. Note that the yellow circle can only be displaced in the red-shaded area, which is for evading the overlapped parameter set. That is in fact related to the reflected: Reflected phase of R_{yy} is determined by the two times of T_{yy} of circle and triangle. (c) Determined phase and amplitude values of T_{xx} and R_{yy} extracted from resultant two-fold meta-atom, calculated by simulation. As shown in the graphs, it is noteworthy mentioning that the scale of *y*-axis is half of the scale in *x*-axis. At the same time, the phase values of T_{xx} and R_{yy} are changing with identical gradients, which means that the phase of R_{yy} changes two times faster than that of T_{xx}. 78

Figure 4.9 (a) Schematic diagram of optical setup for capturing Fourier images of fabricated samples with diode laser of 980 nm wavelength. The input polarizers are subject to change according to the purposes. The two lenses before metasurface are used for collimating the light, and the lenses after metasurfaces are for 2-f system for obtaining the Fourier image of the metasurface. MS: metasurface, CCD: charge coupled device, BS: beam splitter, Pol.: polarizer. (b) Schematic diagram of unit cell composed of two rectangular nanopillars. (c) SEM captured image from sample operating in linear polarization pair. Scale bar: 1 μm (d) Schematic diagrams of three

fabricated samples distinguished by polarization pair in operation. For beam steering and hologram generation samples, this notation is preserved. 79

Figure 4.10 Beam steering results from experiment (a-c) CCD-captured images as well as the line graph extracted near the zeroth order diffraction, showing experimental results of diffraction order efficiency. (a) is from sample 1, operating in linear polarization pair, (b) from sample 2 operating in circular polarization pair and (c) from sample 3 operating in elliptical polarization pair. White arrows indicate the polarization states of the input light. (d) Polarization extinction ratio obtained from three fabricated samples. Simul.: simulation result, Meas.: Measured result.....81

Figure 4.11 Beam deflection schematic diagram and results from simulation and experiment. (a) Schematic diagram showing beam deflection with parameters for diffraction order and polarization states. (b-d) Dot plot showing simulation and experiment result of diffraction order efficiency. (b) is from sample 1, operating in linear polarization pair, (c) from sample 2 operating in circular polarization pair and (d) from sample 3 operating in elliptical polarization pair. Arrows indicate the polarization states of the input light. The written numbers in graph are the diffraction efficiency of desired components. Blue squares are the simulated results and red diamonds are from measured results.....83

Figure 4.12 Hologram generation results from simulation and measurement. From top to bottom, they operate in (a) linear (sample 1), (b) circular (sample 2), and (c) elliptical (sample 3) polarization states. Arrows indicates how the polarizer is directed at input end.....85

Figure 4.13 Polarization extinction ratio of hologram generation sample....86

Chapter 1 Introduction

1.1 Overview of metasurfaces for optical modulation

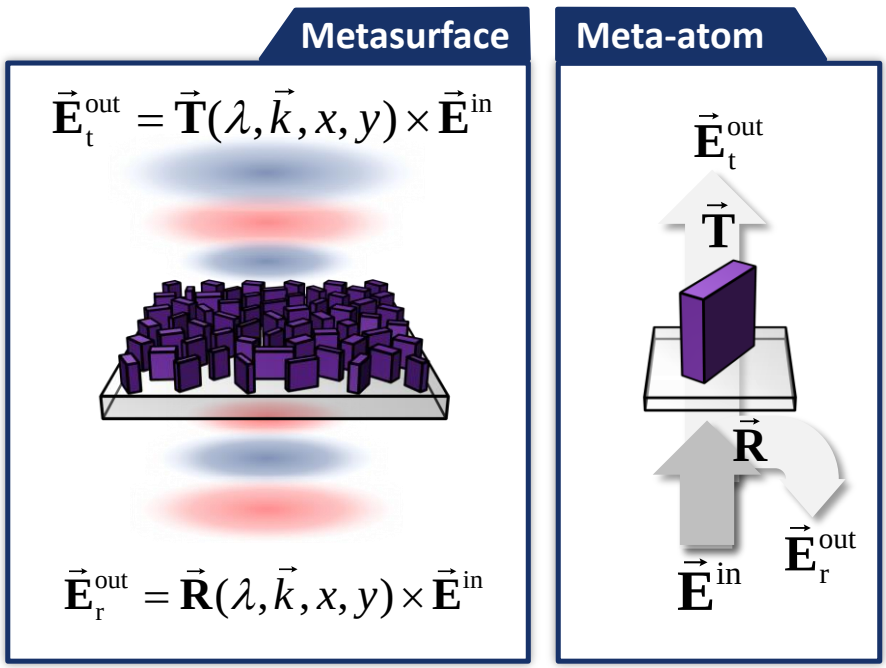

Figure 1.1 Conceptual diagram of metasurface and its unit, meta-atom.

With the recent increase in the weight of smartphones and the activation and development of the wearable smart device market, new types of displays and cameras that can be applied thereto have been actively developed. Especially, optical components represented by cameras have an adverse effect on consumers' choice due to the increase in weight and form factor followed by the advancement of performance. The well-known solution for these problems, holographic optical elements, diffractive optical elements, or waveguide system assembled with conventional refractive optical components is now suffering from the limit including trade-off of

performance and form factor, which delays the applicability and potential to become real-life device. In this regard, machine-learning involved technology has become the breakthrough of some abovementioned issues, but some major problems that are related to the performance of physical factor of integrated device, such as numerical aperture, resolution, aberration etc. cannot be resolved by the speculation produced by software. Accordingly, it is essential to develop or introduce a new optical system with performance and miniaturization to improve the consumer environment.

The prefix meta- means to transcend the following suffix, which implies that one can think of the optical metasurface as something that surpasses the normal surface. Metasurfaces are different from normal surfaces because light reacts abnormally at their boundary in an unexpected manner [1-5]. Practically, they are composed of artificial subwavelength structures that utilize light-matter interactions for specific and user-choosing purposes. As planar counterparts of metamaterials, meta-atoms, which are structural unit of metasurfaces, are engineered to have abnormal electric permittivity and magnetic permeability that are not shown in natural materials. As the atoms determine the optical properties (*i.e.* permittivity, permeability) by their electronic characteristics with their size, the scale of meta-atoms is designed to become smaller than the wavelength of interests, so that the early research on metamaterials or metasurfaces was performed in microwave range, which has a wavelength in centimeter scale [6, 7]. Since recent nanofabrication technology makes it possible to manufacture tens of nanometer-scale building blocks on wafer, this enables to make metasurfaces in the optical regime by scaling down the meta-atoms. Considering that the light-matter interaction is

related to the forward/backward scattering ($E_{out,t}$ $E_{out,r}$) and the absorption by the imaginary index of matter is usually regarded as the unwanted loss, the main purpose and goal of design of metasurfaces have been concentrated on the control of transmission (**T**) and/or reflection (**R**), as depicted in Figure 1.1. The design objectives include but are not restricted to the constituents of light, such as wavelength, wavevector, polarization and nonlinearity. Meanwhile, as mentioned above, employing the fact that the light-matter interaction decides the resultant wavefront elsewhere, shapes and distribution, which also affects the scattering characteristics owing to the spatial dispersion between adjacent structures, are used as design parameters.

Furthermore, metasurfaces attract much attention thanks to their easier fabrication than metamaterials and compactness thanks to two-dimensional shapes [8, 9]. This makes metasurfaces applied to the optical components in the recent decades with their main advantage: their unprecedented capability of light manipulation. Notably, keeping going from strength to strength, light manipulation through meta-atom has surpassed the conventional optic components in terms of their compactness as well as their performances [2, 10]. For example, they were employed to realize the desired wavefront such as complex hologram generation, a piece of planar achromatic lens, beam steering by abrupt phase discontinuity and mimicking the traditional optical elements with superior performance [11-17]. In addition, these properties have developed to go beyond the conventional device, such as polarization multiplexing, multifunctionality with respect to the light properties, multiwavelength functionality, and dispersion engineering, which create and open the potential for the future optical platform [18-23].

1.2 Motivation of this dissertation: metasurface for full-space control

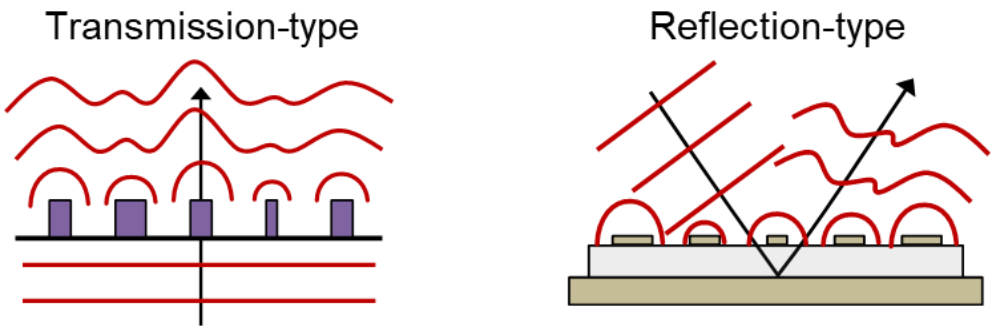

Figure 1.2 Diagram showing two major operations of conventional metasurfaces

Among various research fields branched out, expansion of the information capacity by metasurfaces has been pioneered so far, inspired by their performance and ultrasmall form factor compared to conventional optical elements [24, 25]. In this regard, the illuminating condition of incident light should be modulated for verification of desired operation, and the condition has been polarization, wavelength, incident angle, etc [20, 21, 25-27]. For example, when the meta-atom has shape of the rectangular pillar, anisotropic property emerges and these structural characteristics are used to generate light reaction sensitive to polarized direction of input light wave [21, 28]. This is contrasted with when square or circular pillar is adapted as meta-atom, as they exhibit polarization insensitive operation [29-31]. It is notable mentioning that the former rectangular pillar has merits on the doubling information capacity controlled by polarization, while the latter can be thought to be more versatile since it does not care the polarization of input light. The point is that the numerous structures can be selected by researchers for the unprecedented

multifunctional natures, other than simple structures [1, 2, 6, 8, 24-26]. The development of multifunctional metasurfaces also produces a lot of methods to describe physical proofs of them, proposed by Jones matrix calculus, mode analysis, etc. Meanwhile, apart from them, it is well-known that fixing the observation plane and illumination condition of incident light can add functionality onto metasurfaces without special structural modification or physical origin [32, 33]. As far as we know, the maximum number of holographic images was 63 (2^6-1) which are encoded in the spin and wavelength of incident light [33]. However, this kind of metasurface lacks in versatility because the operation is only restricted to the hologram generation and the strict and careful light incident condition should be guaranteed for desired number of functions. For example, the maximal number of independent controllable phases is known to be three, but if polarizer at the output end is unacceptable, it reduces to two [34, 35].

As one branch of the effort to increase functionality, there have been researches on full-space control using metasurfaces [36-49]. Full-space control means the intentional modulation of forward and backscattering, extending the degree of freedom of metasurface in terms of controlling space. It is different from the conventional metasurfaces in that their controlled spaces are usually restricted to transmission or reflection spaces only. That is, as shown in Figure 1.2, the conventional metasurfaces are designed to operate in transmission- or reflection-type, which controls the wavefront at transmission and reflection spaces, respectively. When a metasurface are designed into transmission-type, for example, the remnant space, in this case, reflection space, will be left undesigned, only to demonstrate meaningless

information. It is notable that the dimension and shape of metasurfaces for full-space control are not unconventional ones compared to conventional metasurfaces. For example, in visible frequency regime, the full-space control can be presented with silicon nanopillar or metal nanorod, which is very common design of metasurface, and when it is realized in terahertz or gigahertz frequency regime, their meta-atoms are popular form of cascaded metallic structure [36, 41, 43, 46, 47, 49]. However, except for several studies that suggest exact usage and the followed design, the full-space control in optical frequency regime has not covered independent control of two spaces. For example, in ref [49], the measuring position and illuminating condition should be rigorously fixed for desired operation. Metasurface platform proposed in refs. [46, 48] cannot make two independent phase profiles into transmission and reflection spaces, respectively. On the other hand, when the full-space control is realized in long wavelength region (centimeters scale), the imparted phase values at transmission and reflection can become different in the majority of researches showing full-space modulation, which improves versatility compared to counterparts in visible region. This types of metasurfaces have merits on the complete separation of transmission and reflection. However, it will have severe problems in efficiency and difficulty in fabrication, if the layered metallic structures are scaled down to the hundreds of nanometers.

In this dissertation, the metasurface platforms that can control the wavefronts (conveyed phase values) of transmission and reflection space independently in optical frequency regime are presented [38, 40]. They are distinguished from conventional metasurfaces in that they only care about

transmission or reflection space as mentioned above. Note that proposed metasurfaces have fundamental difference from full-space control realized in optical frequency regime by other groups. For instance, in the case of ref [46], since it is designed so that transmitted light and the reflected light have the same intensity and phase, it can be rather classified as a conventional metasurface. But it is sufficiently meaningful in that they show the exact usage of structural light extension, and anyway it exhibits the full-space control of light. Also, since it is designed for specific purpose, it has common with proposed metasurfaces in the increasing designable space. Meanwhile, in the case of ref [49], different images can be observed in the transmission and reflection directions only under certain illumination and measurement conditions. Conversely, the proposed metasurface can be used for manipulation of entire space, and the imparted phase values at each space can be independently modulated. To help clear understanding, the discrepancy is shown in Figure 1.3.

It is expected that proposed metasurface platform contributes to the potential of metasurface as a novel light modulator thanks to several reasons: Since there have been a lot of studies that make use of the phase modulation metasurfaces to implement the unconventional mechanism, the proposed metasurface platform can be used to mimic them at full-space. Secondly, considering recent electronic device markets as above, the novel metasurface system shall pave the way to design platform of unprecedented form factor, which is impossible with conventional bulk optic elements.

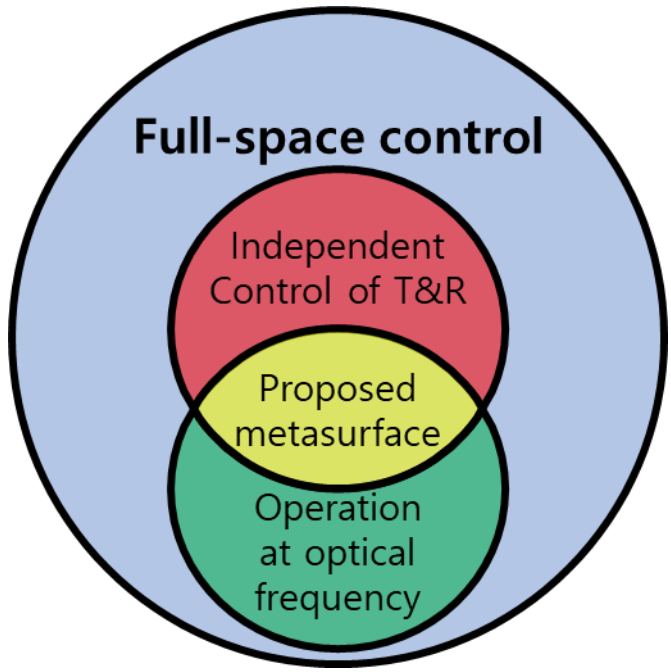

Figure 1.3 Diagram showing the definition of proposed metasurface with respect to the comparison with conventional full-space control

1.3 Scope and Organization

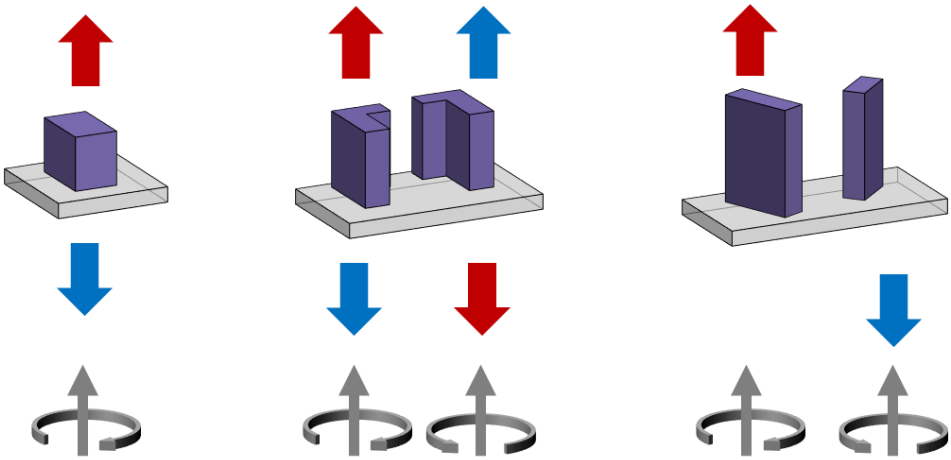

Figure 1.4 Schematic operation for comparison of each chapter. From left to right, described ones are Chapter 2, 3 and 4. Blue and red colors are for expression of distinct imparted phase values. Note that in Chapter 4, arbitrary polarization pair can be adopted for same kind of function.

The main body of this dissertation consists of three chapters. Note that in each chapter, the different types of metasurface that enables independent phase control at transmission and reflection spaces in optical frequency regime will be shown. The methodology of experimental demonstrations in three chapters is same by holographic image generation and beam deflection. To show experimental proofs that are not possible with conventional metasurfaces, the generated holographic images are totally different in transmission and reflection spaces and the imparted phase gradients are also dissimilar by the phase gradient strength or direction.

In Chapter 2, a novel metasurface that enables full-space light control is presented, offering simultaneous and independent transmission and reflection when circularly polarized light is illuminated. Multipolar interference and Pancharatnam–Berry phase are combined with each other

and suggested as a physical background for the proposed device. As far as it is known, this is the first work achieving full-space control in visible range.

In Chapter 3, a metasurface platform consisting of interleaved L-shaped meta-atoms is presented, imparting different and independent phase values to the transmission and reflection directions. In addition, when the handedness of circular polarization of incident light changes, the phase values imparted to each direction are designed to be switched to each other, and this scheme, as far as we know, has never been proposed before. The Jones calculus and multipolar decomposition as above are suggested for physical proofs.

In Chapter 4, a metasurface platform that can decide scattering direction into transmission and reflection by polarization is presented. The designed phase gradient is utilized to flip the transmissive operation into reflection, which becomes possible using the special critical angle condition when normally incident light impinges to meta-atom. Linearly birefringent nanopillars enable two independent phase values with an arbitrary polarization pair. Interleaving two nanopillars in a unit cell makes it possible to realize polarization-selective space control: in contrast to the conventional interleaved metasurface, where each meta-atom operates separately, the operation of a metasurface is determined by its gradient. Three samples were fabricated and measured based on the proposed scheme, and they are distinguished by their operational polarization pair: linear, circular and elliptical polarization.

To avoid confusion while discrimination of proposed studies, the illustration is shown in Fig. 1.4. It shows the structural unit of each study that possesses the ability of phase modulation at transmission and reflection

spaces. The corresponded operation is also depicted with input light condition, showing the differences in point by point. In short, the metasurface in Chapter 2 operates in only one selected circular polarization for simultaneous phase control at full-space, and Chapter 3 works by circularly polarization pair to realize both simultaneous phase control and space conversion together. Platform in Chapter 4 can function normally by arbitrary polarization pair changed user's choice and by polarization change, the light proceeding direction can be tuned, which is like polarizing beam splitter (PBS). Note that their function is still preserved despite the reduction to the structural unit, which is a primary advantage of proposed metasurfaces.

Chapter 2 Simultaneous full-space visible light control

2.1 Introduction

In electromagnetism, multipole expansion has revealed that all kinds of charge distributions in nature can be described as superposition of various eigenmodes, including electric and magnetic modes [50, 51]. Among the various properties of the modes, one of the representative physics is that electric and magnetic modes have distinct parity in terms of optical phase symmetry in transmission and reflection spaces. For example, electric dipole (ED) mode radiation has even parity, so that scattered wavefronts have the same phase values in both front and rear spaces. On the other hand, magnetic dipole (MD) mode radiation has odd parity, so the radiated lights at forward scattering and backward scattering are out-of-phase [52]. This parity rules are related to backscattering intensity expression by Mie scattering coefficients a_n and b_n of order n, $\left|\sum_{n=1}^{\infty}(2n+1)(-1)^n(b_n-a_n)\right|^2$, which also indicates the phase symmetric nature changes at every expansion order. Based on this parity, zero backward scattering is achievable under the condition that electric permittivity and magnetic permeability of the scattering body are equal to each other [50, 52]. This effect is dubbed as Kerker effect, known to be due to destructive interference of the electric and magnetic mode radiation in the reflection space, which stems from various expansion orders of Mie scattering coefficients [50, 52-54].

Recently, thanks to widespread attention of metamaterials in nanophotonics, the scattering radiation patterns including abovementioned multipolar phase effects are utilized for various optical or physical applications [55-59]. For extended functionalities with respect to radiating pattern and corresponding efficiency to desired direction, generalized Kerker effect is exerting its influence as one of the important methods in the field of metaoptics. For instance, by overlapping ED and MD mode with identical value, Huygens' metasurface is proposed to suppress backward radiation, leading to high transmission efficiency [59]. Further interference of multipole mode radiations also enables directive radiation to reflection space, such as perfect magnetic mirrors as well [57]. By fine-tuning of the phase and amplitude ratio of each multipole mode, polarization-control metasurface, high-order diffraction control, and even directive dispersive device have been implemented so far [60-62].

Previously, full-space control has been studied as one of the significant metasurface researches; transmission–reflection integrated bifunctional and trifunctional metasurfaces were demonstrated by multilayered structure which operates in gigahertz range [37, 47]. However, this more-than-one function device demands additional degrees of freedom in terms of design, so that the meta-atom should have large dimensions as well as subsidiary layered structure. Therefore, the difficulty in fabrication makes hard to accomplish scaling down of this scheme to visible region. Here, we propose a simply constructed single-layer metasurface that can control optical phase in full-space, which refers to simultaneous wavefront control at reflection and transmission through imparting distinct phase values. For the desired phase

difference between transmission and reflection, the amplitudes and phases of the multipole expansion modes excited in the meta-atom are adjusted, respectively. Each mode is divided into even parity and odd parity, and an adequate superposition is arbitrarily created into achieving desired phase difference. Consequently, as far as we know, full-space control scheme at visible light is demonstrated with metasurface for the first time.

2.2 Metasurface design

2.2.1 Design strategy and numerically calculated results

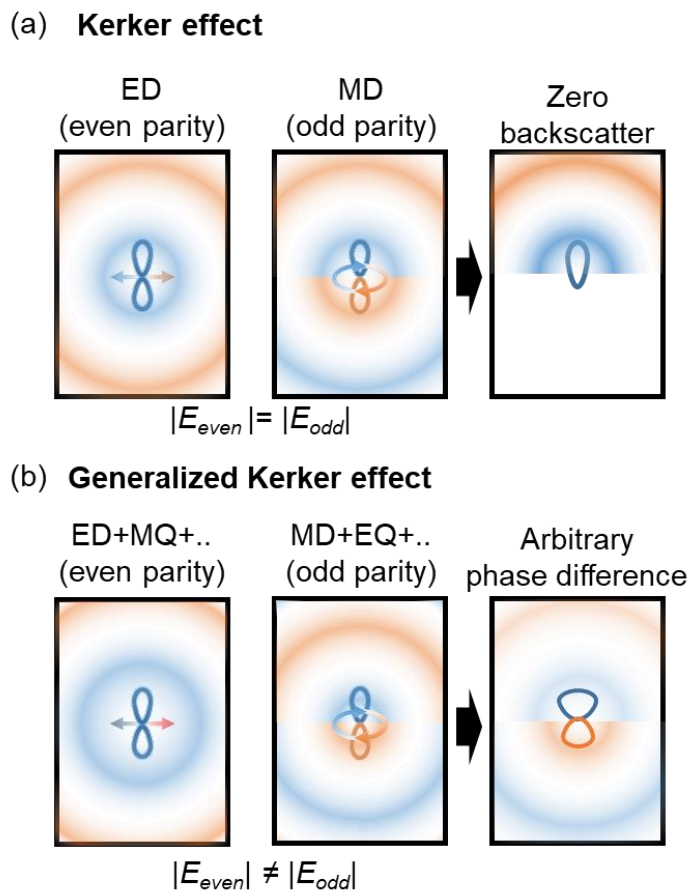

Figure 2.1 Diagram showing Kerker effect. (a) When the ED mode and MD mode exist with equal magnitude, it is possible to generate a scattering source that has no backscattering. That stems from the disparity of phase symmetry of each mode: ED has even parity, and MD has odd parity. (b) Generalized Kerker effect as the proposed scheme in this paper. If it is possible to generate arbitrary values for even and odd parity, it contributes to modulation of phase difference between transmission and reflection spaces.

For implementation of full-space modulation of light at visible region, a novel proposition for manipulation of transmission and reflection coefficient is essential. To do this, generalized Kerker effect is exploited as a means of

metadevice design (see Fig. 2.1) [52]. In common, Kerker effect refers to the condition of zero backward scattering, which can be achieved when the ED mode as the representative of even parity (E_{even}) and MD mode as odd parity (E_{odd}) have the same complex values, as shown in Fig. 2.1a [51]. Likewise, as shown in Fig. 2.1b, when the E_{even} and E_{odd} are designed to have distinct amplitude and phase value, arbitrary phase value difference at transmission and reflection can be provided. Therefore, this shows that if it is possible to manipulate scattered multipolar modes as desired, unconstrained manipulation of transmission and reflection coefficients is achievable, including asymmetric radiation direction control and achieving distinct phase difference between both spaces. Due to orthogonality of vector spherical harmonics, far-field radiated distribution of scattered light from one meta-atom can be projected to ED and MD radiations, and higher-order radiations, such as electric and magnetic quadrupole or octupole mode radiation [51]. These multipolar mode radiations have different phase symmetric natures and distinct contributions to amplitude or scattering cross section [52]. That is, after examining how these values affect the actual transmission or reflection coefficient, the desired phase difference can be achieved through appropriate adjustment of the values. Note that the polarization considered is cross-polarization, which makes expression of transmission and reflection coefficients different as written below,

$$t = E_{even}(z) + E_{odd}(z), \tag{2.1}$$

$$r = E_{even}(z) - E_{odd}(z), \tag{2.2}$$

where E_{even} is composed of the linear combination of even parity modes of scattered light, such as ED, magnetic quadrupole (MQ), and electric octupole

(EO), while E_{odd} consists of odd parities like MD, electric quadrupole (EQ), magnetic octupole (MO), etc. Plus, the multipolar coefficients via decomposition, which can be calculated through induced current density distribution or far-field radiation pattern, offer portions of each mode in transmitted and reflected amplitude. Here, the analytic method to retrieve multipolar coefficients is introduced. At first, note that the arbitrary radiation can be expressed by sum of the vector spherical harmonics $\mathbf{X}_{lm}$ (normalized form) thanks to their orthogonality, where l and m demotes the azimuthal and magnetic quantum numbers of harmonics.[1] Vector spherical harmonics have complex values, and have interesting characteristics: they have inversion behavior under spatial inversion, and this feature is divided into two, one is odd parity and the other even parity in terms of phase symmetry. For arbitrary scattered field **E**, multipolar expansion (or decomposition) is expressed as below,

$$\begin{aligned}\mathbf{E}(r,\theta,\phi) = \sum_{l=1}^{\infty}\sum_{m=-l}^{l} i^{l}\sqrt{\pi(2l+1)}\Big[\frac{a_E(l,m)}{k}\nabla\times\{h_l^{(1)}(kr)\mathbf{X}_{lm}(\theta,\phi)\} \\ + a_M(l,m)h_l^{(1)}(kr)\mathbf{X}_{lm}(\theta,\phi)\Big],\end{aligned} \tag{2.3}$$

where r, θ, ϕ are parameters of a spherical coordinate system, and $h_l^{(1)}$ is spherical Hankel function of the first kind, and k is the wavenumber. Here, the multipole coefficients consist of two kinds: one is a_{E} for electric modes and the other is a_{M} for magnetic modes. In eq. (2.3), the field made by a_{E} at l=1 is called ED mode, and for l=2, EQ mode. Likewise, the field made by a_{M} is also called MD mode. As abovementioned, these multipole modes generated by each coefficient have phase symmetry determined by order l. For example, field by a_{E} has even parity when l is an odd number, and odd

parity when l is an even number. On the other hand, field by a_M has odd parity when l is an odd number, and even parity when l is an odd number. From this nature, definition of E_{even} and E_{odd} referring to the phase parity is made.[1] For multipolar decomposition, obtaining a_E and a_M is not an option, so from induced current density it is calculated from silicon nanopillar by referring to previous studies [61, 63]. And from eq. (2.3), we calculate the effective amplitude of each mode, considering one polarization which is affected by PB phase. Since we only consider the normal incidence, polar angle and azimuthal angle are set to zero, then desired polarization is extracted. For this, a_E and a_M are calculated twice at incident polarization of x- and y-polarized light. Cross-polarized component which is affected by PB phase can be expressed through scattering parameters by x- or y-polarized light incident as t_x–t_y or r_x–r_y. For instance, when x-polarized light is matter of interest, E_θ from $\mathbf{E}(r, \theta, \phi)$ is effective t_x with condition of kr>>1, θ=0, and ϕ=0. Likewise, y-polarized transmission t_y is E_ϕ effectively. These can be expressed from eq. (2.3) like below,

$$E_{x,electric} = -a_E(l,m)\frac{1}{r}\frac{\partial}{\partial r}\left(rh_l^{(1)}(kr)\right)\{\mathbf{X}_{l,m}(\theta=0,\phi=0)\}_\phi,$$

$$E_{y,electric} = a_E(l,m)\frac{1}{r}\frac{\partial}{\partial r}\left(rh_l^{(1)}(kr)\right)\{\mathbf{X}_{l,m}(\theta=0,\phi=0)\}_\theta,$$

$$E_{x,magnetic} = a_M(l,m)h_l^{(1)}(kr)\{\mathbf{X}_{l,m}(\theta=0,\phi=0)\}_\theta,$$

$$E_{y,magnetic} = a_M(l,m)h_l^{(1)}(kr)\{\mathbf{X}_{l,m}(\theta=0,\phi=0)\}_\phi. \quad (2.4)$$

The simplified form with polarization can be derived from above,

$$E_E(l) = (2l+1)\{i[a_E(l,-1)-a_E(l,1)]_x - [a_E(l,-1)+a_E(l,1)]_y\},$$

$$E_M(l) = (2l+1)\{-i[a_M(l,-1)+a_M(l,1)]_x + [a_M(l,-1)-a_M(l,1)]_y\}, \quad (2.5)$$

where subscripts x and y are for incident polarization direction. After acquisition of desired phase difference between transmission and reflection spaces, horizontal movement for covering independent phase control is enabled via Pancharatnam–Berry (PB) phase method, which assign the same phase retardation to transmission ($\angle t$) and reflection ($\angle r$) space. PB phase provides the phase delay which depends on the rotation angle of structure and affects only the cross-polarized component in condition of circularly polarized light incident. Hence, this makes the phase difference $\Delta\phi = \angle r - \angle t$ stationary for cross-polarized light. Thanks to the rotation angle dependence of PB phase, 2π coverage comes feasible with constant phase difference between spaces. Thus, this indicates that when the difference $\Delta\varphi$ is adjustable as desired, the phases of the transmitted and reflected lights can be modulated independently.

2.2.2 Determined structure and numerical demonstration

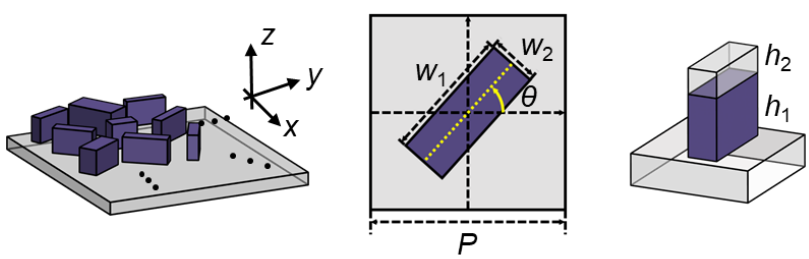

Figure 2.2 Schematic diagram showing building blocks. It is composed of amorphous silicon nanopillar array fabricated on commercial quartz wafer. Lower diagram shows structural parameter of meta-atom as well as the simulation space used when obtaining phase difference value.

As a building block, amorphous silicon nanopillar with spatially distinct structural parameters is distributed by square periodicity (Fig. 2.2). Proposed

device is designed to operate at visible wavelength of 660 nm. Here, pixel pitch is chosen as 400 nm in order for suppressing unwanted high diffraction order components. Each nanopillar is capped with oxide layer, which is used as etch mask during fabrication. This oxide layer can be removed by using buffered oxide etchant, and barely affects functionality regardless of its existence. This layer is regarded to have thickness (h_2) fixed at 90 nm considering the fabrication recipe, while nanopillar thickness (h_1) is 250 nm that is intended thickness. Fig. 2.2 also shows the three spatially varying structural parameters for each: w_1, w_2, and in-plane rotation angle θ. As abovementioned, in order for desired phase difference $\Delta\phi$, the structural parameters w_1 and w_2 of silicon nanopillars should be variant values for additional degrees of freedom on design. These variable structural parameters w_1 and w_2 serve to alter the contribution of excited modes in nanopillar, and this, in turn, changes the occupation of each multipolar mode at radiation. In short, the rotation angle corresponds to the phase coverage and varying w_1 and w_2 contribute to maneuvering the values $E_{\mathrm{E,M}}(l)$ of eq. (2.5), to obtain desired phase difference $\Delta\phi$. Firstly, for analytic verification of multipolar decomposition, a set of four structure parameters, designated with index from 1 to 4, is selected to cover 0 to 2π phase difference with equal difference $\pi/2$: w_1 is 265, 220, 300, 295 nm, and w_2 is 60, 110, 85, 60 nm, each. These values are calculated by a commercial numerical analysis tool of finite element method, COMSOL Multiphysics 5.3a. This is simulated in Floquet boundary condition. It is notable that for calculation of multipole coefficients, induced current density which radiates spheric harmonic modes is required, so that the simulation space is switched to have spheric shape as blue triangle, shown in

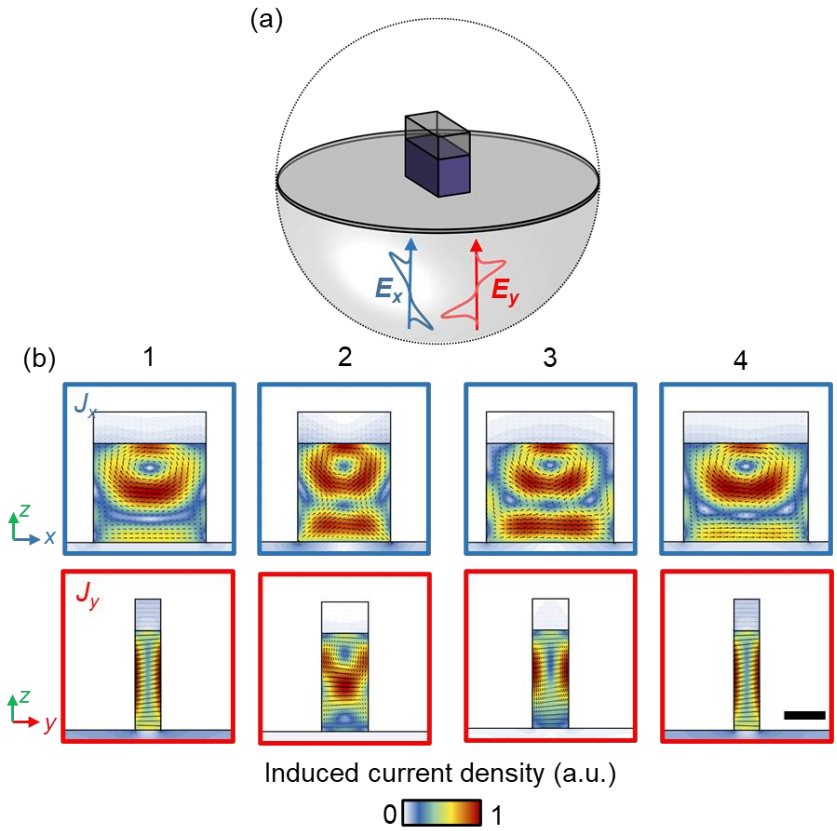

Figure 2.3 (a) The simulation space used for multipolar decomposition (b) Colored map and black arrows expressing induced current density for four selected parameters. Left four blue plots show current density when x-polarized light is incident while right reds are resulted from y-polarized light incidence. Scale bar: 100 nm

Fig. 2.3a. After acquiring the induced current density as shown in Fig. 2.3b, each field portion of multipolar components is calculated, depicted by bar graph in Fig. 2.4a. This shows that the mode distributions vary depending on dimensions, which enables to control $E_{\mathrm{E,M}}(l)$ to some extent. Next, the effective efficiency from the multipolar modes is expressed by phase symmetry parity, as shown in Fig. 2.4b. When the phase difference is 0 (index 1), the even parity shows predominant value. As the phase difference approaches to π (index 3), the odd parity becomes dominant. In contrast,

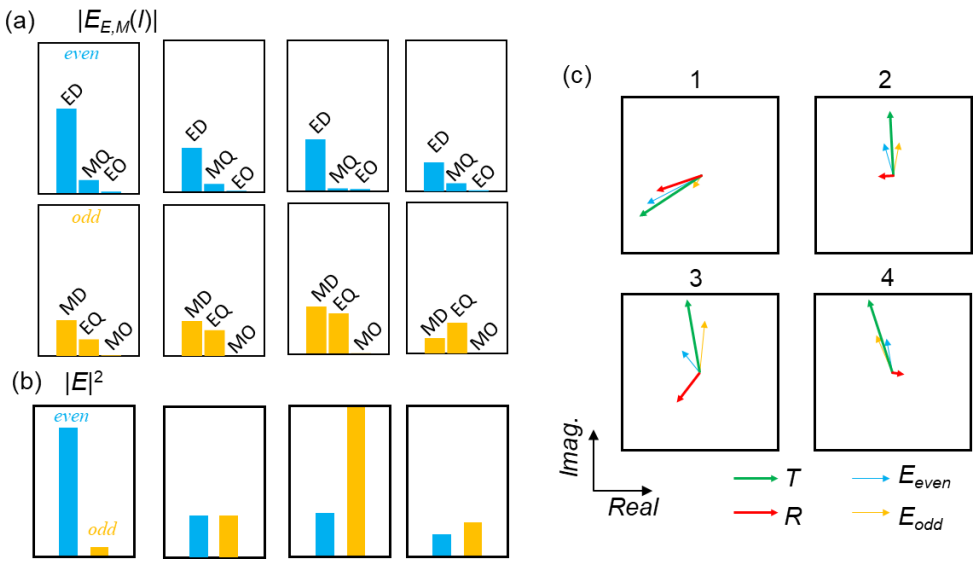

Figure 2.4 (a) Effective amplitudes by bar graph, which denote contributions of each multipole mode with l being less than three. (b) Bar graph shows effective efficiency, which is calculated by adding each mode by parity, then squaring. (c) Complex plane showing E_{even}, E_{odd}, transmission and reflection coefficients expressed by colored arrows.

when the phase difference is $\pm\pi/2$, their contributions to efficiency do not show any intuitive ease. For intuitive and detailed result, the complex plane is also shown with arrow graph denoting E_{even}, E_{odd}, transmission and reflection, as shown in Fig. 2.4c. Finally, from the results of eqs. (2.1) and

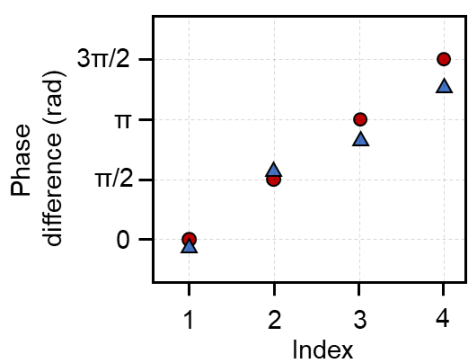

Figure 2.5 Dot graph showing phase difference value calculated by numerical result (red circle) and multipole expansion (blue triangle).

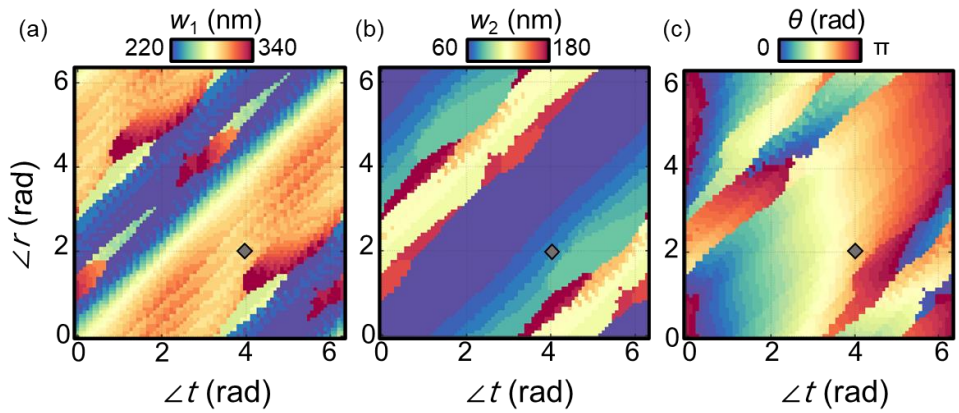

Figure 2.6 Colored map showing structural parameters of a) w_1, b) w_2, and c) θ of which meta-atom imparts desired phases to transmission and reflection spaces. Structural parameters are calculated numerically in periodic boundary condition when right CP wave is incident from bottom of the structure. As an example, for desired phase of 4 and 2 rad each at transmission and reflection spaces, a structural parameter set of (230 nm, 115 nm, 165°) is obtained by the same positions on these three graphs (marked with gray diamonds).

(2.2), the phase differences can be obtained, which can be seen in Fig. 2.5. It can be seen that the analytically obtained phase differences are almost the same as the phase differences obtained by numerical results. There is a slight difference due to higher-order terms as well as the different simulation space that is used in each case. As such, it is possible to derive the desired phase difference by calculating how much the multipolar expansion order affects the cross-polarization component.

From abovementioned method, two methods for lookup table of structural parameters are suggested. First, the results shown in Fig. 2.6a–c are structural parameter sets that cover the full phase at both spaces independently. For acquisition of these graphs, cross-polarized transmission and reflection in circularly polarized (CP) light incident condition are firstly calculated while changing w_1, w_2, and θ. Next, from these aggregated data

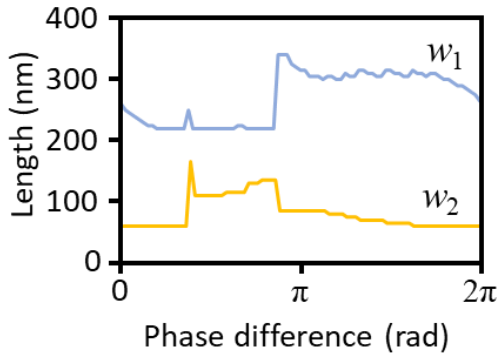

Figure 2.7 Line graph denoting structural parameters with respect to phase difference of transmission and reflection.

table, the parameter set (w_1, w_2, θ) is obtained having the minimum error value,

$$E = \frac{1}{2}\left|[(t(w_1, w_2, \theta) - C_t e^{j\angle t}) / C_t e^{j\angle t}]^2 + [(r(w_1, w_2, \theta) - C_r e^{j\angle r}) / C_r e^{j\angle r}]^2\right| \quad (2.6)$$

with $\angle t$ and $\angle r$ varying from 0 to 2π. C_r and C_t are pre-desired amplitude values, which are properly selected as 0.36 and 0.45, respectively, for high efficiency within minimum error. Note that C_r and C_t are chosen to have efficiency of 10% and 20% at reflection and transmission space, respectively, and the values are also chosen as ones close to the calculated average efficiency of structural parameter set, which are 12.8% and 12.1%, each. Here, note that the w_1 and w_2 are set to meet the condition of $w_1 > w_2$. As second method, apart from the lookup table result of Fig. 2.6a-c, the desired phase of transmission and reflection can also be obtained following: First, if phases of *a, b* for transmission and reflection is required, w_1 and w_2 is determined by the graph of Fig. 2.7. Fig. 2.7 can also be acquired from eq. 2.6, having one difference of decrease in calculation load. Then, the θ is rotated until reaching *a* and *b*. From these mapped values, the phase imparting to both spaces as

desired is achieved through proposed metasurface. It is also notable mentioning that this metasurface only operates at one polarization state, either right-handed circularly polarized light or left-handed. Additionally, from selected parameters which are same as abovementioned indexed parameters, the transmission and reflection spectra are also calculated to present spectral characteristic of the proposed scheme (Fig. 2.8a–d), of which structures are indices of Fig. 2.3. In addition, it is notable that the proposed structure only operates in narrow band near target wavelength of 660 nm due to the dispersive nature of phase difference value, as shown in Fig. 2.8e.

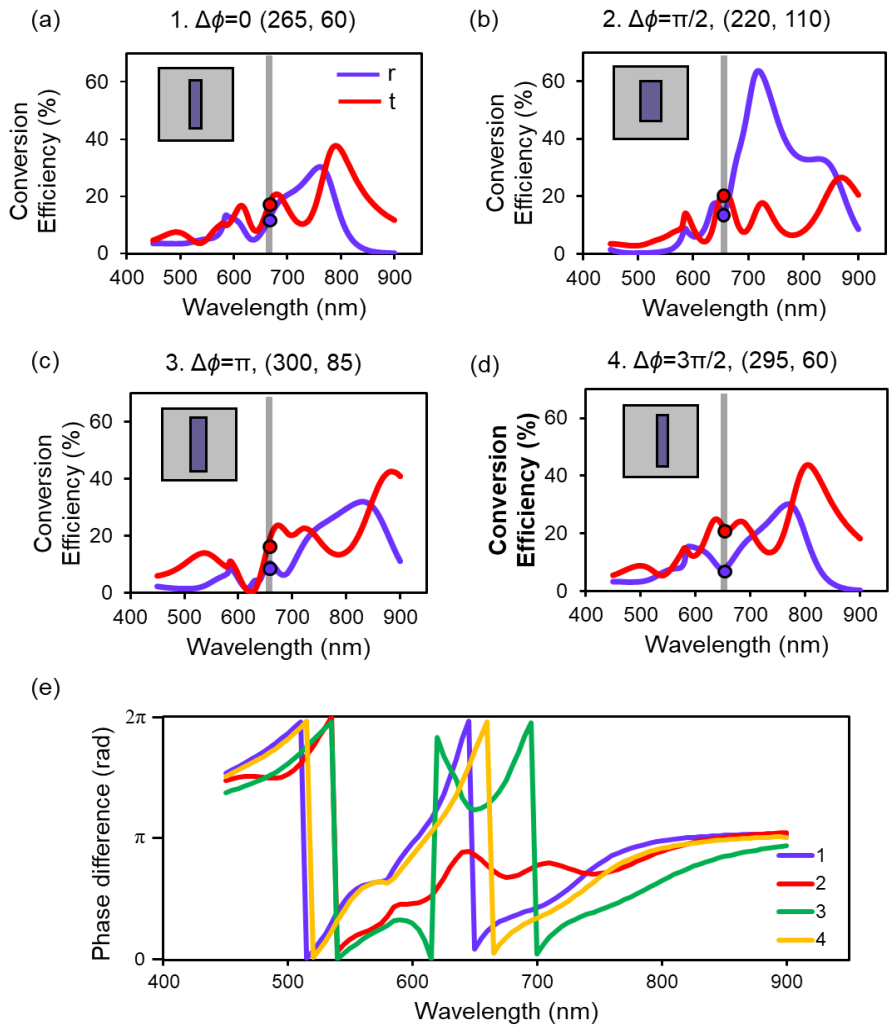

Figure 2.8 Dispersive characteristics of selected meta-atoms. (a–d) Transmission and reflection spectra of conversion efficiency for selected parameters of dashed squares from above graphs. Here conversion efficiency stands for the cross-polarized components scattered by incident CP wave. Inset shows the top view of the structures. Red and blue circles are conversion efficiency of transmission and reflection in target wavelength. (e) Phase difference between transmitted and reflecte light for four selected parameters. Gray vertical line is located at 660 nm, showing identical phase difference.

2.3 Experimental demonstration

2.3.1 Experimental setup and fabrication

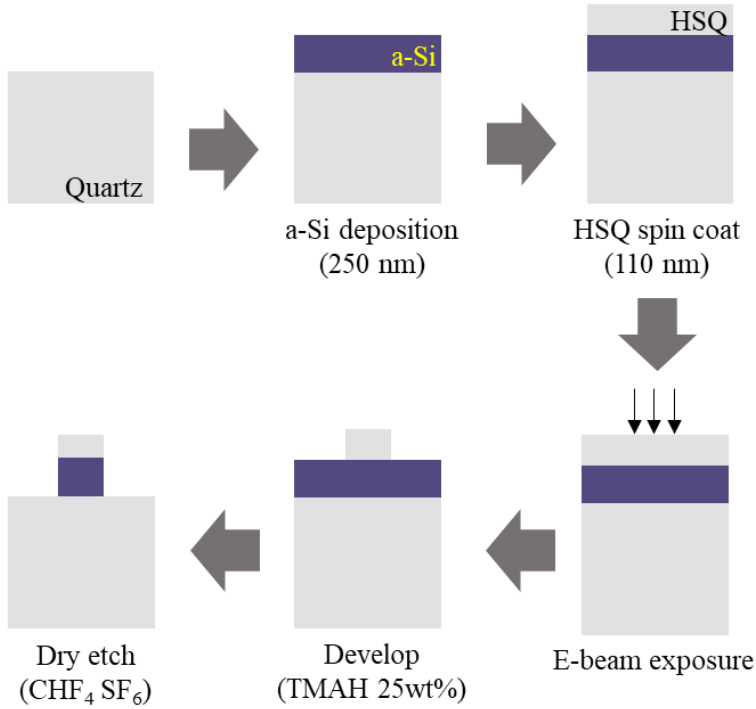

Figure 2.9 Fabrication process with simplified explanation

As explained in the previous section, the proposed metasurface enables to realize any kind of flat optics controlling both transmission and reflection simultaneously. In this article, we propose two applications as examples to experimentally verify the functionality of the proposed structure: one is for generalized refraction and reflection law, and the other is 3D holograms with distinct holographic images according to the transmission or reflection mode. By the virtue of simple structure of proposed metasurfaces, they are fabricated by conventional nanofabrication method. In detail, the device used in experiments was fabricated on quartz wafer substrate by standard electron

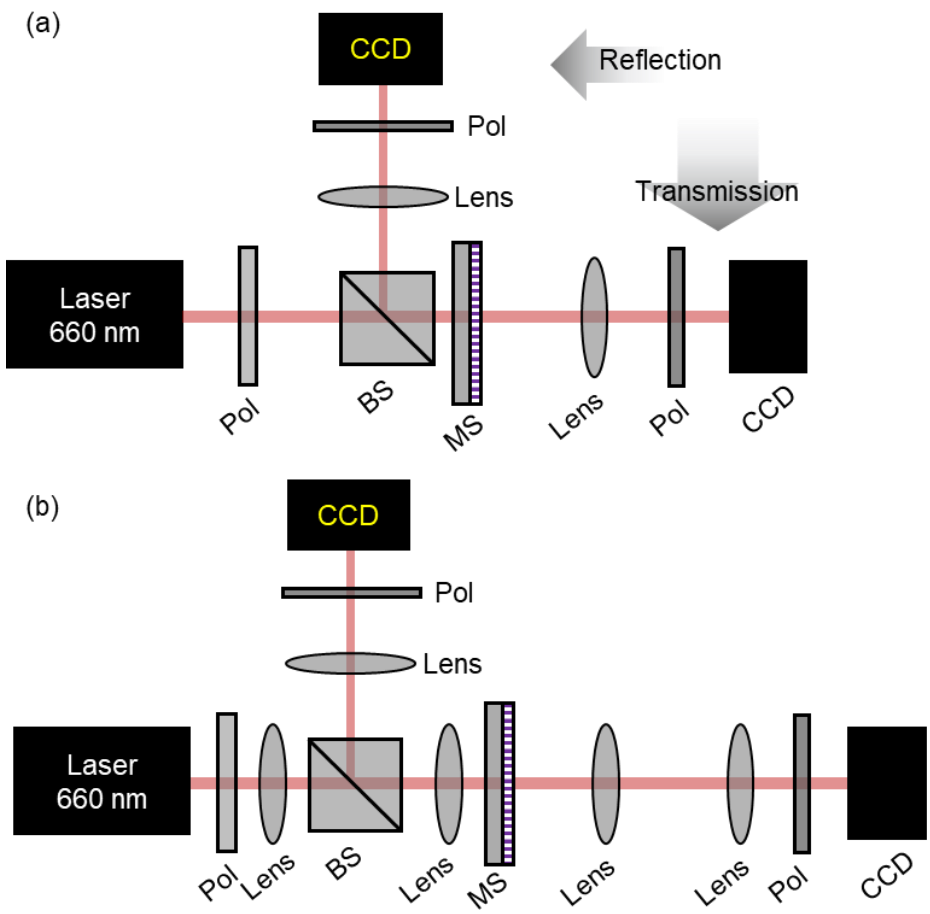

Figure 2.10 Measurement setup for proposed metasurface. (a) 2-f setup for capturing beam deflection images (b) 4-f setup for holographic image retrieval. Pol: polarizer (circular) BS: beam splitter, MS: metasurface, CCD: charge coupled device

beam lithography process. At first, the silicon oxide of 100 nm and the following amorphous silicon of 250 nm were deposited using PECVD (Applied Materials P5000, OEM Group) based on SiH_4 and helium. Next, a single-layer negative-tone resist hydrogen silsesquioxane (HSQ, XR-1541-006, Dow Corning) was spun on sample at rotation speed of 4000 rpm, then post-baked for 4 min at 80 °C. This resulted in oxide layer of about 110 nm. Nanopatterning was performed with commercial electron beam lithography

system (JBX-6300FS, JEOL) at 100 kV condition. Exposed sample was developed using tetramethylammonium hydroxide solution (TMAH 25 wt% in H_2O, Sigma Aldrich) for 30 seconds, and then rinsed in flowing water for 15 seconds. Finally, sample was etched via inductively coupled plasma – reactive ion etching (ICP-RIE) tool to get the final device. The process is briefly shown in Fig. 2.9. All samples used in experiments were fabricated with same dimension of 160 × 160 μm^2. Experimental measurements were conducted with charge-coupled device (CCD) sensor and commercial 660 nm laser and the setup is illustrated in Fig. 2.10. To mention in advance, experimental verification of the two methods was conducted, and accordingly, both the 2-f (2.10a) and 4-f (2.10b) systems were schematically illustrated. Unlike conventional metasurface devices, it requires two times of measurements, which are carried out in transmission and reflection space.

2.3.2 Asymmetric beam deflection

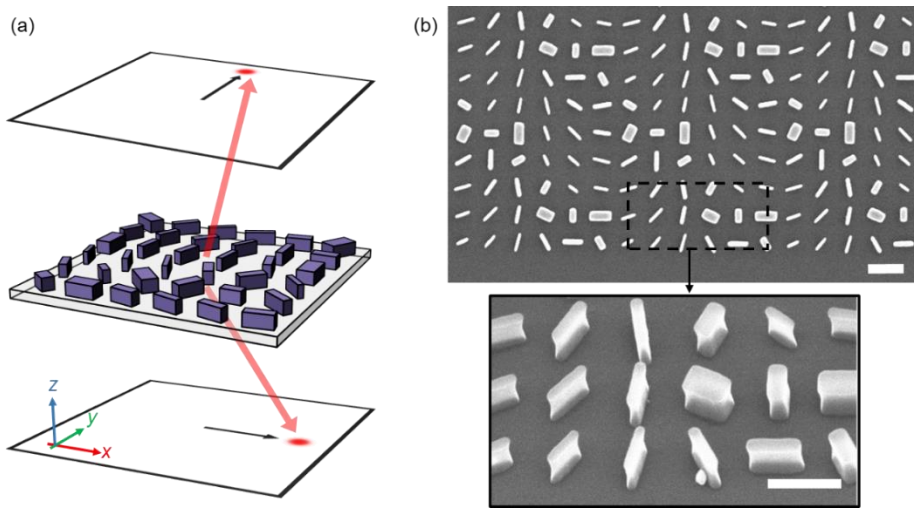

Figure 2.11 Conceptual illustration of the first device which deflects transmitted wave into +*y*-direction, while it sends reflected one to +*x*-direction. (b) Fabrication result for the first deflection device. Scale bar: 400 nm

As the first example, asymmetric beam deflection is demonstrated. Unlike conventional metasurface, the proposed metasurface enables the output beam to have distinct propagating directions to both spaces. This can be achieved by imparting different phase gradient values to each space, which is possible through independent phase control. Here, two samples are implemented to experimentally verify this scheme. When the CP light is incident onto the sample of Fig. 2.11a, the transmitted light deflects into +y-axis direction while the reflected one bends to +*x* direction. For realization of this scheme, the sample is designed via supercell structure which contains 6×6 meta-atoms, as shown in Fig. 2.11a. Their structural parameter set can be found in Table 2.1 (w_1), 2.2 (w_2) and 2.3 (θ). Considering the principle of generalized Snell's law, the deflection angle of each space is 15.96°, which is calculated by asin(λ/Λ), where λ is wavelength of incident light (which is 660 nm) and Λ is

Table 2.1 Mapped structural parameters of beam deflection case 1 for w_1

***x* (nm)** / ***y* (nm)**	w_1 **(nm)**					
	0	400	800	1200	1600	2000
0	305	295	320	225	220	260
400	295	265	225	335	260	310
800	305	225	220	260	300	300
1200	225	220	260	305	295	320
1600	335	260	310	295	265	225
2000	260	300	300	305	225	220

Table 2.2 Mapped structural parameters of beam deflection case 1 for w_2

***x* (nm)** / ***y* (nm)**	w_2 **(nm)**					
	0	400	800	1200	1600	2000
0	60	75	85	115	60	60
400	70	175	115	160	60	60
800	80	115	60	60	60	75
1200	115	60	60	60	75	85
1600	160	60	60	70	175	115
2000	60	60	75	80	115	60

Table 2.3 Mapped structural parameters of beam deflection case 1 for θ

***x* (nm)** / ***y* (nm)**	θ **(deg)**					
	0	400	800	1200	1600	2000
0	165	30	90	30	115	140
400	170	65	0	90	110	135
800	10	150	55	80	105	145
1200	120	25	50	75	120	0
1600	0	20	45	80	155	90
2000	170	15	55	100	60	145

Table 2.4 Mapped structural parameters of beam deflection case 2

***x* (nm)**	0	400	800	1200	1600	2000	2400	2800	3200	3600	4000	4400
w_1 **(nm)**	305	300	225	225	310	295	225	225	300	310	225	225
w_2 **(nm)**	60	75	115	60	60	80	115	60	60	85	115	60
θ **(deg)**	165	15	150	35	45	80	30	95	105	160	90	155

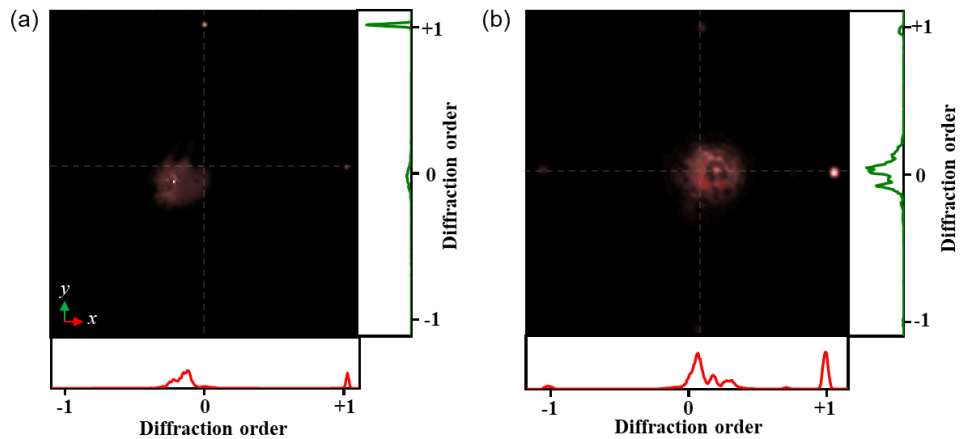

Figure 2.12 (a, b) Experimental result showing intensity captured by CCD camera as well as the line graph expressing the intensity value of desired diffraction orders.

periodicity of supercell structure that possesses 2π phase gradient. It is notable that any supercell structure that has two phase gradient values for transmission and reflection spaces can be made with proposed scheme, such as 3 × 3 or 9 × 9 as well. After fabricating the sample (Fig. 2.11b), we captured the Fourier transformed image using CCD camera in 2-f system, as shown in Fig. 2.12a, b. Unwanted high diffraction order terms also exist at both spaces, and they lead to lower extinction ratio of 4.49 and 8.85 dB each, which are defined as desired signal (desired diffraction order) to noise (unwanted term designed to appear at other side) ratio. These are intrinsically due to the imperfect amplitude fluctuation at design phase and length parameter of

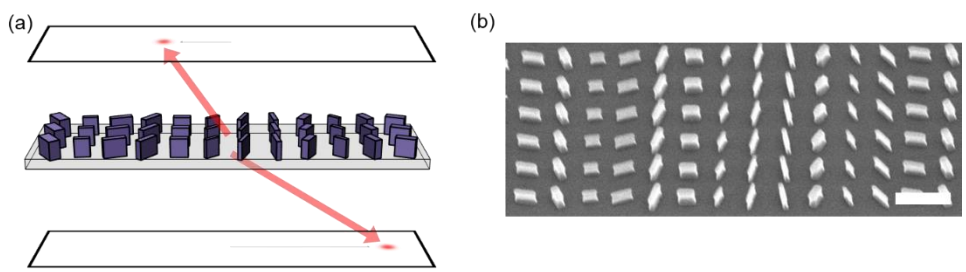

Figure 2.13 Conceptual diagram for the second device that induces the transmitted wave direction into the first diffraction order and reflected wave to the minus second diffraction order. (b) Fabricated second device sample. Scale bar: 800 nm.

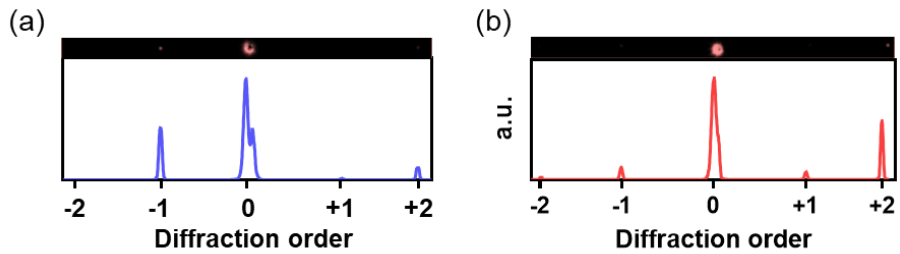

Figure 2.14 Experimental result showing intensity captured by CCD camera as well as the line graph expressing the intensity value of desired diffraction orders and unwanted one together. (a) is captured in transmission space, and (b) is in reflection space.

sample from numerical simulation, which stems from fabrication error. Another unprecedented function is imparting phase gradient of opposite sign and dissimilar value to both spaces, presented in Fig. 2.13a. Here, the deflection angles are determined like abovementioned as 7.903° and −15.96° for transmission and reflection space, respectively. This sample consists of 1D supercell of 12 meta-atoms, deflecting transmitted light into the first diffraction order while reflected light into the minus second diffraction order. Like above device, this is fabricated and shown in Fig. 2.13b. The structural parameters are shown in Table 2.4 as above. The transmitted and reflected amplitudes are detected by CCD camera as shown in Fig. 2.14a, b, showing extinction ratio of 6.33 and 6.81 dB, respectively. The zeroth order portions found in both samples attribute to the finite extinction ratio of the polarizer used in our measurement setup.

2.3.3 Asymmetric hologram generation

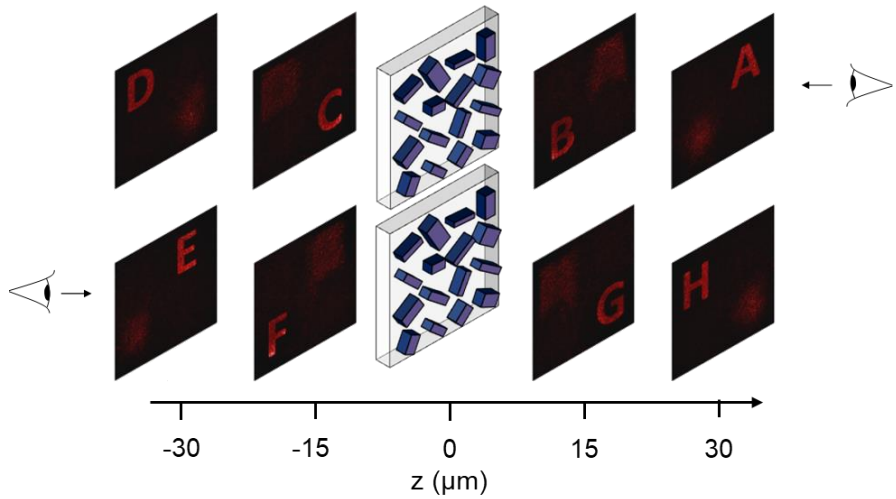

Figure 2.15 Illustrations of Fresnel-type hologram generation via proposed metasurface. It shows the operation of hologram generating device possessing two faces.

As a second category, the proposed metasurface is implemented to generate Fresnel-type holograms with different depth perceptions in both spaces. As shown in Fig. 2.15, the device is designed to reproduce eight different alphabet letters with respect to the z-axis and viewing direction. We designed computer-generated hologram (CGH) assuming normal incidence of right circularly polarized plane wave. The phase profile used here was obtained through angular spectrum method (ASM), which is a method based

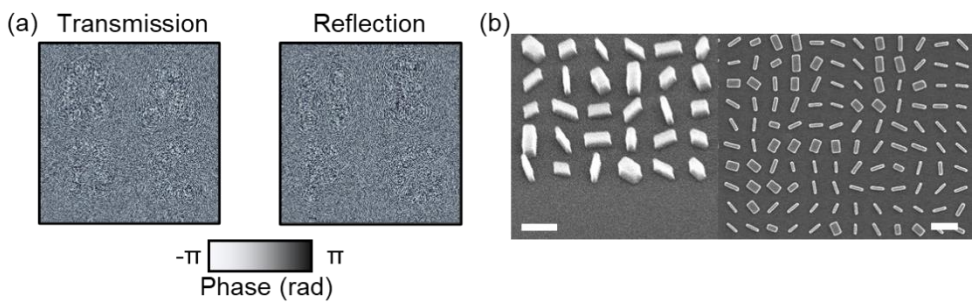

Figure 2.16 (a) Phase profile of each face obtained by ASM. (b) Fabricated sample captured in CCD. Scale bar: 400 nm.

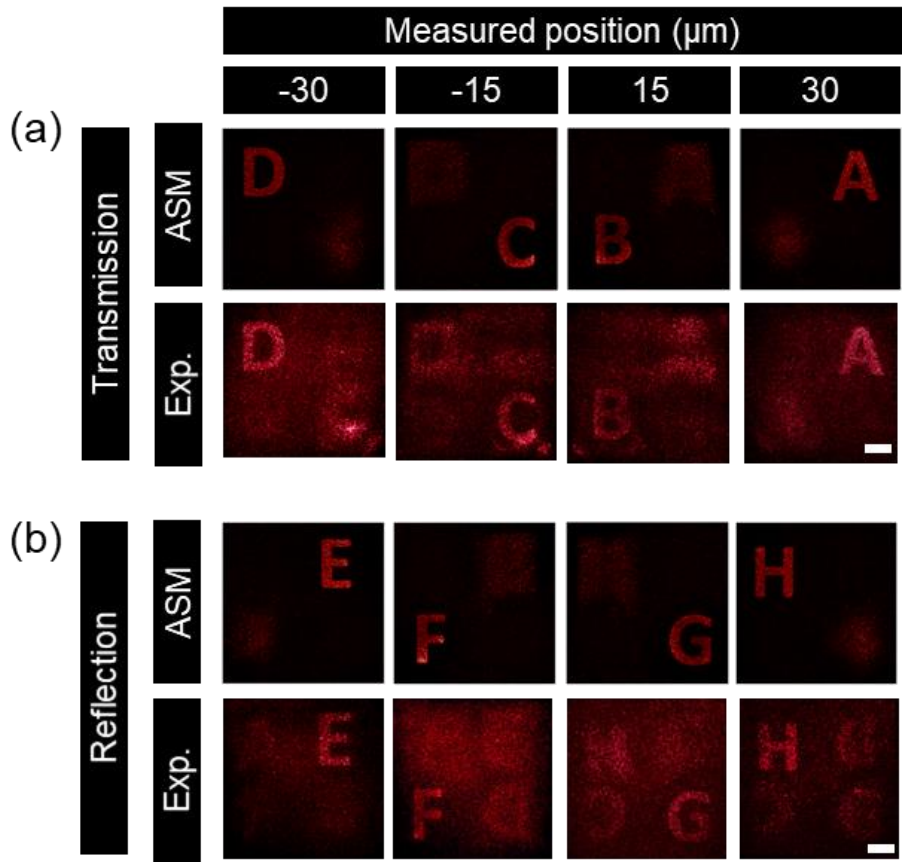

Figure 2.17 Amplitude profile of (a) transmission and (b) reflection space. Upper eight images are numerical results by ASM, while lower eight images are captured by CCD camera. Scale bar: 30 μm

on the diffraction optics for obtaining diffracted light field [13]. ASM is repeated four times per one phase profile for a letter, and adding these four profiles results in one profile. The resulting phase profile at both faces is shown in Fig. 2.16a. By mapping phase profile to parameter set, the images of the fabricated sample are shown in Fig. 2.16b. Interestingly, because of the way the hologram is generated through the virtual image, one can see that different letters are displayed when we focus on the same spot on both sides. This is one of possible functionalities that cannot be produced through conventional holographic devices including spatial light modulators and

metasurfaces. The hologram conversion efficiency is calculated by ASM using the amplitude and phase value which are retrieved by Fig. 2.6. Hologram conversion efficiency is obtained by four planes, calculated with $\eta = P_h/P_i$, where P_h is power from hologram and P_i is incident power of light. The determined value is shown in Table 1. Experimental result has lower conversion efficiency in comparison with numerical result. For observing of holographic images, the modified microscopy setup was employed to see holographic images on both transmission and reflection (Refer to Fig. 2.10b). We captured the holographic images through a CCD camera with an objective lens and a tube lens by adjusting the z position of the device. Experimental and numerical results are depicted together in Fig. 2.17. For numerical results, ASM is used again for acquisition of the hologram. Specifically, from the phase profile at the origin point (z = 0 μm) shown in Fig. 2.16a, the amplitude profile is calculated at the desired position, z = −30, −15, 15, 30 μm. In the case of transmission-type, the experimental results are reproduced at almost the same level as the numerical result. The letters on the reflection side are reproduced at a good level, but the letters of the transmission side are visible with some noise. This appears to be due to the imperfect polarization filtering of the hologram on the reflection side.

Table 2.5 Hologram conversion efficiency (unit: %) calculated from numerical result.

***z* (μm)**		**-30**	**-15**	**15**	**30**
Hologram conversion efficiency (%)	**Reflection**	8.84	9.79	9.85	8.93
	Letter	E	F	G	H
	Transmission	14.2	15.6	16.1	14.6
	Letter	D	C	B	A

2.4 Conclusion

In this article, the simple-structured silicon metasurface is reported for the simultaneous full-space control of light for visible wavelength. For independent phase control at each space, the concept of generalized Kerker effect is proposed, and this is verified both analytically and numerically together. Here, simple structure of amorphous silicon nanopillar is adopted as meta-atom, which has merits of well-known nanofabrication feasibility. The proposed scheme is tested by experimental result, applied in asymmetric beam deflection as well as hologram generation. Thanks to versatility of proposed metasurface, the generalized Snell's law is extended to transmission and reflection together, allowing phase gradient values. Hologram generation is also demonstrated, reinforcing its ability to be employed in further optic applications. The metasurface research is paving its way to consumer electronics and commercial optics applications such as biomedical imaging or augmented reality platform. Researchers are using the metasurface in a way that replaces one part of the bulk optics to keep up with this trend [64]. In this context, considering the versatile nature of proposed method to control both spaces, the scheme presented in this article can be advantageous in further miniaturization and advance in light-weight future devices.

Chapter 3 Polarization dependent space conversion with L-shaped meta-atom

3.1 Introduction

As mentioned above, most of metasurfaces for full-space control have been proposed on frequency regime of terahertz and gigahertz, and due to their structural characteristics of stacked metallic design, applying them to optical frequency seems to have still long way to go [14, 36, 37, 42, 47]. Some design for full-space control for optical frequency has been proposed, but they are mostly devised for specific purposes [46, 49]. Also, metasurfaces as depicted in Chapter 2, which can control the transmission and reflection independently in optical frequency, have been proposed as a multifunctional full-space wavefront manipulator. However, full-space control metasurfaces including Chapter 2 lack in versatility that most of conventional metasurfaces possess thanks to their polarization dependent functionality, compared to the powerful and multifunctional counterpart designed at terahertz and gigahertz frequency. In this chapter, for extending versatility of full-space metasurface, we proposed a novel metasurface platform. It is composed of the periodically arranged L-shaped meta-atoms (LSMAs) of which the cross-polarized components when circularly polarized light shines go out alternatively into transmission or reflection spaces by the handedness of polarization state. Phase is encoded using PB phase, which is determined by the in-plane rotation angle of the meta-atom. Here, to control the phase of transmission and reflection space independently by the handedness of circular polarization, the spatial multiplexing method is employed, which is typical way to append

the freedom on metasurface design. We employed Jones matrix and multipolar decomposition method to reveal the inherited physics of LSMA. For experimental demonstration of proposed scheme, two types of samples are fabricated: One is for holographic image generation, and the other is for asymmetric beam deflection. We expect that this research will contribute to the development of new types of optical devices, especially in fields that require new form factors thanks to its polarization-dependent nature.

3.2 L-shaped meta-atom for space conversion

When the arbitrary meta-atoms interact with incident light, their light-matter interaction can be expressed by Jones calculus as follows:[65]

$$\begin{pmatrix} o_x \\ o_y \end{pmatrix} = \begin{pmatrix} A & B \\ C & D \end{pmatrix} \begin{pmatrix} i_x \\ i_y \end{pmatrix}, \tag{3.1}$$

where the Jones matrix is substituted for polarizing output characteristics of reflection or transmission of meta-atom, and the relation between incident wave $(i_x\ i_y)^T$ and transmitted (or reflected) wave $(o_x\ o_y)^T$ is demonstrated by matrix calculus. Note that two *ABCD* matrices exist per one meta-atom, and one of them is for transmission and the other is reflection. The shape and dimension of meta-atom determine the entries of the Jones matrix, *A*, *B*, *C* and *D*. For example, the meta-atom shaped of rectangular pillar lets the Jones matrix become diagonal matrix, which is chiefly selected meta-atom for polarization selectivity or generation of PB phase. Using Jones calculus makes the analysis of rotating effect of the meta-atom obvious, and this derivation also reveals the PB phase expression:

$$\begin{aligned} \begin{pmatrix} o_+ \\ o_- \end{pmatrix} &= \mathbf{\Lambda}^{-1}\mathbf{R}_\theta \begin{pmatrix} A & B \\ C & D \end{pmatrix} \mathbf{R}_{-\theta}\mathbf{\Lambda} \begin{pmatrix} i_+ \\ i_- \end{pmatrix} \\ &= \frac{1}{2} \begin{pmatrix} A+D+i(B-C) & [A-D-i(B+C)]e^{-j2\theta} \\ [A-D+i(B+C)]e^{j2\theta} & A+D-i(B-C) \end{pmatrix} \begin{pmatrix} i_+ \\ i_- \end{pmatrix}, \end{aligned} \tag{3.2}$$

where subscripts + and – stand for the handedness direction of the circular basis: With linear basis expression, + is $(1\ i)^T$, and – is $(1\ -i)^T$. It is noteworthy mentioning that + polarized light is left-handed circularly polarized (LCP) light in transmission, but it becomes right-handed polarized (RCP) light when viewed from the direction of reflection. Here for convenience when

considering polarization taken effects by PB phase, the notation of + and – polarized light rather than RCP or LCP is preferred. $\mathbf{\Lambda}$ is basis change matrix from linear to circular basis, and $\mathbf{R}_\theta$ is the rotation matrix with respect to angle θ written as:

$$\mathbf{\Lambda} = \frac{1}{\sqrt{2}}\begin{pmatrix} 1 & 1 \\ i & -i \end{pmatrix}, \tag{3.3}$$

$$\mathbf{R}_\theta = \begin{pmatrix} \cos\theta & -\sin\theta \\ \sin\theta & \cos\theta \end{pmatrix}. \tag{3.4}$$

By eq. (3.2), two points are inferred: First, the handedness of circular polarization determines the sign of the PB phase. Second, *B* and *C* contribute to the amplitude disparity between cross-polarized components in circular basis. The first fact has been employed by many groups to build polarization contrast for increasing information capacity of phase modulation metasurfaces, but hardly was the second one. In this paper, we use the LSMA as structural unit which has non-zero *B* and *C*, and it, as discussed later, plays a vital role for desired scheme.

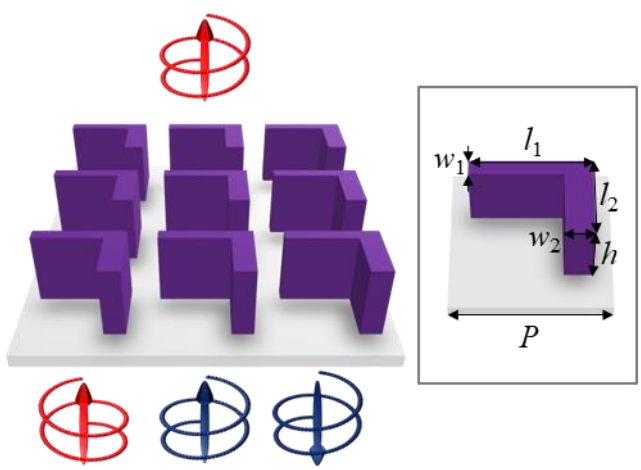

Figure 3.1 Schematic diagram showing operation of single LSMA and its structural parameters

Next with Jones calculus, the reason for harnessing LSMA is elaborated. The schematic illustration and performance of LSMA is shown in Fig. 3.1. Obviously, the shape of LSMA itself accounts for the entries of Jones matrix. Since LSMA consists of two arms of different lengths ($l_1 > l_2$), this makes the difference of A and D, which are co-polarized components of scattered light. B and C have same value, which is related to the mirror symmetry with respect to the z axis. [65] Finally, LSMA has total three independent complex elements determined by geometric parameters of itself. Putting this into eq. 3.2 provides the expression:

$$\begin{pmatrix} o_+ \\ o_- \end{pmatrix} = \frac{1}{2}\begin{pmatrix} A+D & (A-D-2iB)e^{-j2\theta} \\ (A-D+2iB)e^{j2\theta} & A+D \end{pmatrix}\begin{pmatrix} i_+ \\ i_- \end{pmatrix}. \qquad (3.5)$$

Therefore, using LSMA makes two cross-polarized components differ. Here, the specific condition that $A - D$ equals $2iB$ or $-2iB$, which lets one of cross-polarized components becomes zero, is employed. Here, we assume $A - D$ equals $-2iB$, where the incident – polarized (RCP) light makes high transmission of cross-polarized light while incident + polarized (LCP) light destructively interferes to make zero cross-polarized transmission. At the same time, this design criterion can be extended to reflection as well: the structural parameters are fine-tuned to achieve $A - D = 2iB$. So that in terms of reflection, the inversed relation is realized. That is, the incident + polarized light makes high reflection in cross-polarized component, and – polarized light seldom produces cross-polarized reflection. As a result, if only cross-polarized components from LSMA are considered, forward scattering by – polarized light and backward scattering by + polarization are desired. It can be also understood by the energy conservation: Since the co-polarized

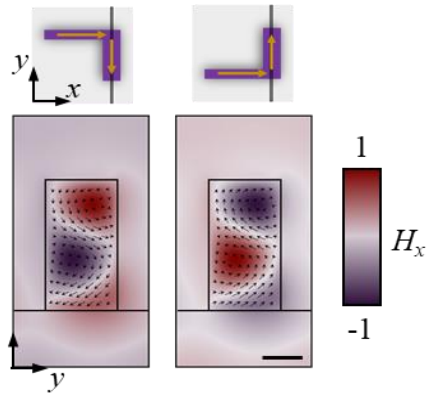

Figure 3.2 Schematic diagram showing one example of LSMA and its enantiomeric counterpart. Lower two field distributions show when x-polarized wave is used as excitation source. Black arrows show the vector expression of induced current distribution. Scale bar: 100 nm

components in transmission and reflection remain unchanged by handedness, the contrast in cross-polarized transmission shall directly affects cross-polarized reflection through opposite sign. Of course, the maximized cross-polarized transmission does not guarantee the almost zero cross-polarized reflection, so optimizing geometric parameter should be accompanied. In short, if the components having PB phase are regarded as signal, its direction will be determined according to the handedness of input circular polarization. Note that polarization-dependent full-space control is achieved, however, single LSMA itself cannot convey independent phase values into transmission and reflection spaces as long as the imparted PB phases are kept the same.

To employ LSMA to devise independent phase control at full-space, the enantiomeric counterpart is introduced. When the *x*-polarized light excites the modes that contribute to the radiation into transmission or reflection, *y*-polarized components such as T_{yx} or R_{yx} (B in eq. (3.1)) will be the result of modes excited at *y*-directed arm. Since the enantiomeric counterpart has the

same dimension and only differs in the *x*-position of *y*-directed arms, the current value of *y*-direction becomes the opposite sign compared to original LSMA, as shown with yellow arrows in Fig. 3.2. How the induced current is distributed proves this fact as well. Using finite element method (COMSOL Multiphysics 5.5), the in-plane components (J_y, J_z, H_x) across *y*-*z* cross-section of LSMA are computed at 633 nm of wavelength through arbitrary LSMA, when *x*-polarized light is illuminated. The results shows that they have spatially same distribution with opposite sign. Since the induced current takes effects on *B*, the *B* (cross-polarized component in linear polarization basis) of enantiomeric counterpart will have same relationship with induced current, and this, in turn, makes the relation of cross-polarized components in circular basis reversed according to eq. (3.5). That is, the cross-polarized components by + polarized light mostly proceed in the transmission space, and those by – polarized light are mostly reflected. It can be explained by schematic illustration as shown in Fig. 3.3a. Here, one can picture putting

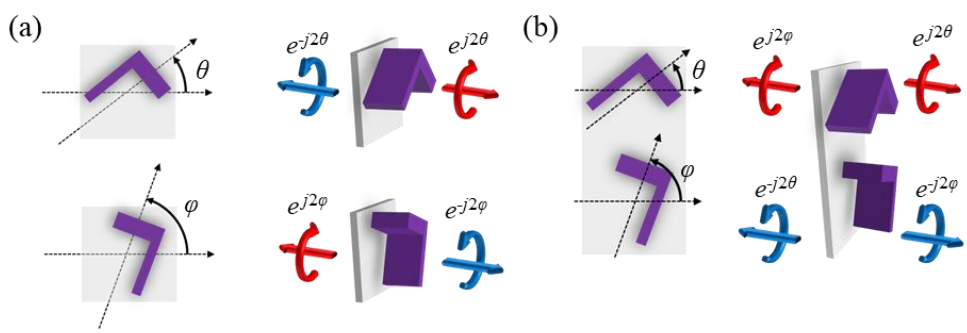

Figure 3.3 Schematic diagram for explanation of the role of LSMA (a) Comparison of a LSMA and its enantiomeric counterpart. Scattered light in red color is the resultant light from + polarized light, while blue colors are scattered light when – polarized light is illuminated. (b) Interleaved case and its corresponded operation by polarization. The phase by angle θ (φ) is at transmission (reflection) space when + polarized light is illuminating source and when it is changed to – polarization, the phase by angle θ (φ) proceed to reflection (transmission) space.

these two structures together to make unit cell (Fig. 3.3b). By virtue of the method of interleaving, the use of PB phase by separate LSMAs makes independent phase profiles. Since the influencing spaces are also irrelevant to each other, the resultant performance becomes independent phase impartment into full-space. Furthermore, when the handedness of incident circular polarization changes, the proceeding direction of scattered light by each LSMA can be altered, which is unprecedented scheme as far as we know with even every frequency range considered. It is well illustrated in Fig. 3.3b, with the point that their signs are flipped due to the nature of PB phase. Throughout this chapter, we call this operation as the polarization dependent space conversion, since the spaces having information expressed by phases are conversed by the polarization.

3.3 Simulation results

3.3.1 Determined parameters and multipole decomposition

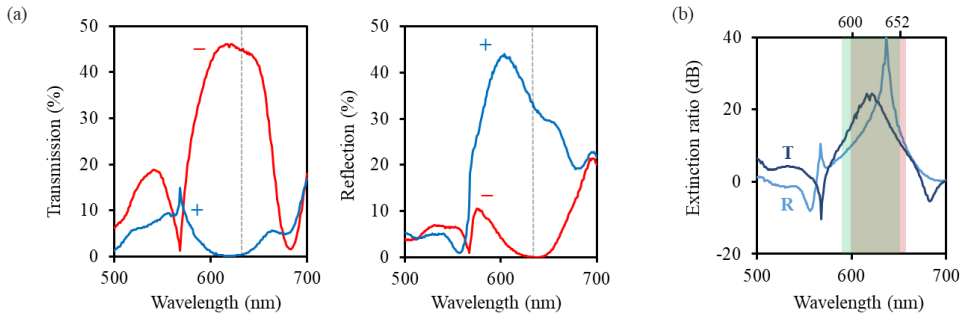

Figure 3.4 (a) Line plots showing cross-polarized component of transmission (left) and reflection (right) spectrum altered by incident handedness of circular polarization. (b) Extinction ratio spectra of transmission and reflection, respectively. In terms of transmission, it is ratio of – to + polarization, while in reflection, it is ratio of efficiency of cross-polarized light by + to – polarized light. Shadowed region is marked for extinction ratio larger than 10 dB.

As mentioned above, the final LSMA should meet the condition of $A - D = -2iB$ for desired operation. First for excitation of the sufficient multiple modes in the LSMA, the thickness h is chosen to 380 nm considering the target wavelength (633 nm) and refractive index of composing material (a-Si:H). Being aware of the fabrication, the LSMA is assumed to be on the quartz wafer. The determined LSMA throughout this paper is l_1: 300 nm, l_2: 200 nm, w_1: 40 nm, w_2: 70 nm, when pixel pitch P is 390 nm for suppressing unwanted diffraction. The simulated conversion efficiency at transmission and reflection varying the polarization is shown in Fig. 3.4a. The simulation space is set to Floquet periodic condition, and the circularly polarized light is incident from the quartz wafer part. At 633 nm marked by line in Fig. 3.4, when the – (+) polarized light is illuminated, conversion efficiency at transmission reaches to 45.1% (0.486%), while at reflection, 0.0386%

(33.5%). The desired efficiency contrast is forming narrow bandwidth around 633 nm both at the transmission and reflection. For showing precise bandwidth of operation of suggested LSMA, the extinction ratio (ER) in dB scale is calculated in Fig. 3.4b. When the specific criterion is regarded that the ER should be 10 dB at least and this condition should be met for transmission and reflection simultaneously, the overall bandwidth is 52 nm (600~652 nm). The wavelength of maximum ER varies at transmission and reflection, which is 622 nm at transmission and 637 nm at reflection, reaching 24.5 dB and 40.5 dB, respectively.

Next for further insight to LSMA, the multipolar decomposition is introduced. There are two reasons why the multipolar decomposition can be exploited in desired scheme: First, the multipole coefficients, which are one of the results that can be obtained from the multipolar decomposition, are directly concerned with the output light from the scatterer. Second, each multipole coefficient has even or odd phase symmetry with respect to the forward and backscattering direction, which can show the excuses of transmission and reflection contrasts by observation of contribution of each coefficient to cross-polarized transmission and reflection. When the contribution of each mode to scattered light is available, it can be well summarized by followed equation.

$$t = E_{\text{even}} + E_{\text{odd}}, \tag{3.6}$$

$$r = E_{\text{even}} - E_{\text{odd}}. \tag{3.7}$$

In eq. (3.6) and (3.7), E_{even} and E_{odd} correspond to the sum of the complex amplitudes included in each parity mode. For example, electric dipole, toroidal dipole, magnetic quadrupole and electric octupole mode belong to

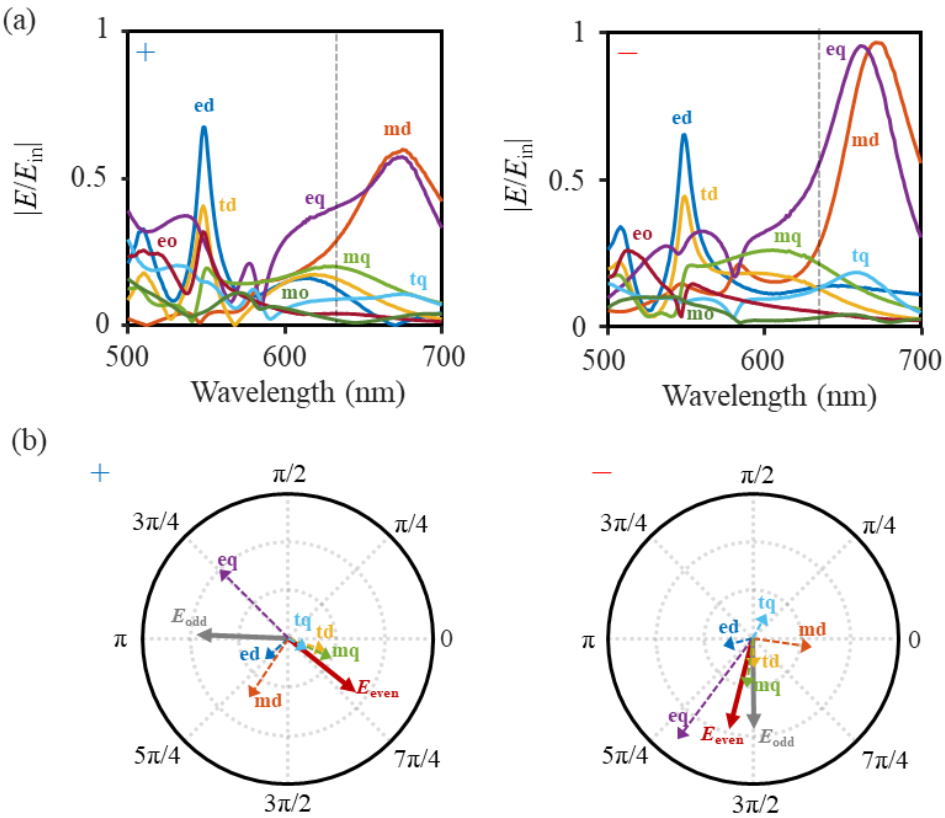

Figure 3.5 (a) Line plots showing absolute values of electric fields by each multipole modes. Left (right) is the result when + (-) polarized light is used as excitation source. (b) Complex plane expression of each multipole mode except for octupole modes when the wavelength of source is 633 nm. The sum of modes having even and odd parity each is also shown for clarity.

even parity, and magnetic dipole, electric quadrupole, toroidal quadrupole and magnetic octupole mode to odd parity. Note that the transmission does not include "1", which is obligatory for representing background wave, because the cross-polarized transmission is of interest. From eq. (3.6) and (3.7), for suppressed reflection, E_{even} and E_{odd} should have same strength and phase. On the other hand, when the zero transmission is desired, they should possess out-of-phase characteristics. Therefore, using the formula suggested in ref. [66], the radiated electric fields by each mode are retrieved for

observing the contribution of multipolar modes to the transmission and reflection. Here, same simulation condition as above except for the absence of quartz substrate is employed for cancellation of the substrate effect. Since the LSMA has thickness of the order of incident wavelength, high order multipolar modes up to octupoles are calculated. Also, with the prediction that L-shape can support substantial toroidal response, toroidal dipolar and quadrupolar moments are considered during calculation.

When comparing two spectra distinguished by incident polarization, it seems no difference near 633 nm in terms of their amplitudes, as shown in Fig. 3.5a. The multipole modes show differences in resonant behavior in terms of the amplitude and position of their resonant peak or dip. The polarization sensitive responses can make the phase behavior of each multipole vary. It is verified in Fig. 3.5b by the complex plane expression in 633 nm wavelength, showing the phase characteristics of each mode and the summed value of E_{even} and E_{odd}. This diagram proves the fact that the multipole modes are excited such that LSMA exhibits the desired scheme. That is, E_{even} and E_{odd} have abovementioned relationship for suppressed transmission and reflection at each incident condition. By their overwhelming lengths, the magnetic dipolar (MD) and electric quadrupolar (EQ) mode are dominant factors of E_{odd}, and they have noteworthy polarization dependent characteristics, they rotate by 90 degrees counterclockwise. In the case of E_{even}, although it does not possess noticeable elements, magnetic quadrupolar (MQ), toroidal dipolar (TD) and electric dipolar (ED) mode have similar contribution in both incident conditions. Their sum is sufficient to be dominant element, and they have opposite polarization sensitive phase

behavior compared to their counterparts: they rotate by 90 degrees clockwise. Considering that in + polarized light incidence condition, the E_{even} and $-E_{odd}$ are parallel to each other (zero transmission), the phase relationship of abovementioned dominant modes makes E_{even} and E_{odd} parallel (zero reflection) in – polarization. This phase relationship can be understandable by detailed analysis performed by field distribution with respect to various excitation sources, which is originally due to the structural nature of LSMA.

3.3.2 Polarization-dependent phase behavior of LSMA

Here, the reason why this special phase behavior occurs is discussed. First, the understanding of the characteristics of each multipole mode should be preceded. For example, the calculation used in MD and EQ mode is nearly same except for the *z*-directed current part of which the detailed expression is shown as below,

$$\mathrm{MD}_y = \frac{1}{2c}\int d^3r[zJ_x - xJ_z] \tag{3.8}$$

$$\mathrm{EQ}_{xz} = \frac{1}{i2\omega}\int d^3r[xJ_z + zJ_x] \tag{3.9}$$

where the integration is performed in the LSMA, and c and ω are light speed at vacuum and angular frequency, respectively. Note that in eq. (3.8) and (3.9), the *y*-polarized MD (MD_y) and *x*-polarized EQ (EQ_{xz}) are considered since they contribute to the same outcoupled *x*-polarized wave. Therefore, their phase relation altered by polarization is same. Also referring to the schematic diagram (Fig. 3.6) showing the three-dimensional current distribution of MD

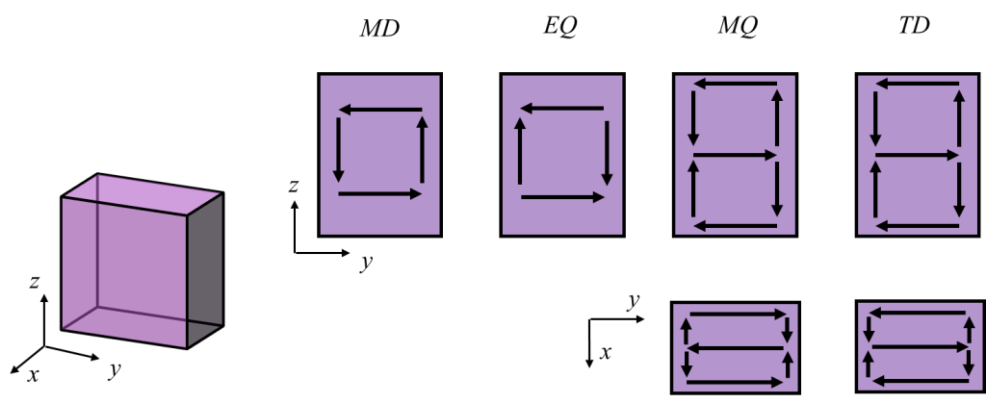

Figure 3.6 Schematic diagram for clear understanding of four selected multipole modes by the representative rectangular nanopillar. Note that the black arrows indicate the desired induced current for outcoupled *y*-polarized wave at each multipole modes. If necessary, in addition to the *yz* cross section, *xy* plane expression is provided.

and EQ, this characteristic is well revealed. Similarly, in the case of components in E_{even}, MQ and TD mode show similar tendency like MD and EQ, as shown in Fig. 3.6. It is noteworthy mentioning that while the values MD and EQ will differ a lot owing to the contribution of *z*-directed induced current, MQ and TD will be nearly the same since the current distribution in *xy* cross section, which causes the difference between the two modes, will not be sufficiently large due to narrow width of proposed LSMA.

Second, as polarization dependent magnitude difference is due to the structural nature of LSMA, $2iB$ in eq. (3.5), the corresponded component is calculated for each mode of interest. In detail, using two orthogonal linearly polarized waves as the excitation source, the multipolar decomposition is executed again. For the result separated by each mode, in *x*-polarized light incidence condition, we carry out the multipolar decomposition and the contribution to outcoupled *x*- and *y*-polarized wave (E_{xx}, E_{yx}) is computed, and in *y*-polarized light, vice versa (E_{yy}, E_{xy}). Note that E_{xx}–E_{yy} can be considered

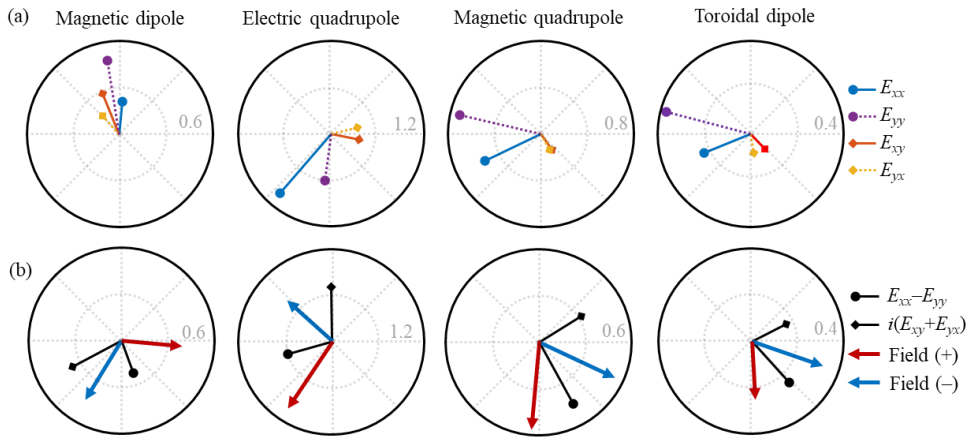

Figure 3.7 Complex plane expression of four dominant multipole modes (a) Expression of the fields decomposed when linearly polarized wave is excitation source. (b) Multipole modes that show the contribution to the cross-polarized terms when circularly polarized light impinges, calculated from upper line result. The field by the handedness of polarization is shown together.

nothing to do with the change of the handedness of circular polarization, while $i(E_{xy}+E_{yx})$ is sensitive part which is directly related to the polarization handedness. From the result in Fig. 3.7a, it is notable that for all considered modes, the strength of E_{xx} and E_{yy} is much greater than the E_{xy} and E_{yx}. Furthermore, for all four modes that the phase of the cross-polarized field (E_{xy}, E_{yx}) is delayed from that of the co-polarized field (E_{xx}, E_{yy}). As shown in Fig. 3.7b, the calculated result of comparing the blue and red arrows that corresponds to $E_{xx}–E_{yy}$ and $i(E_{xy}+E_{yx})$ each shows the similar magnitudes for all modes. When comparing their phase difference, it can be seen that the two phase differences on the left and the other two phase differences are opposite. One can think that the identical arm dimension of LSMA will result in zero contribution of $E_{xx}–E_{yy}$. As a result, it can be known that the distinct arm dimension in LSMA induces polarization dependent behavior at each multipole mode. To fulfill the condition of matching the complex value of A-D and 2iB, the thickness of LSMA should be sufficiently thick to support high order multipole mode such as MQ and TD mode to be comparable with MD and EQ mode. It is also related to the separation of $\underline{E}_{\text{even}}$ and E_{odd}, because distinct phase behavior of each mode is necessary.

3.4 Experimental demonstration

3.4.1 Unit cell determination

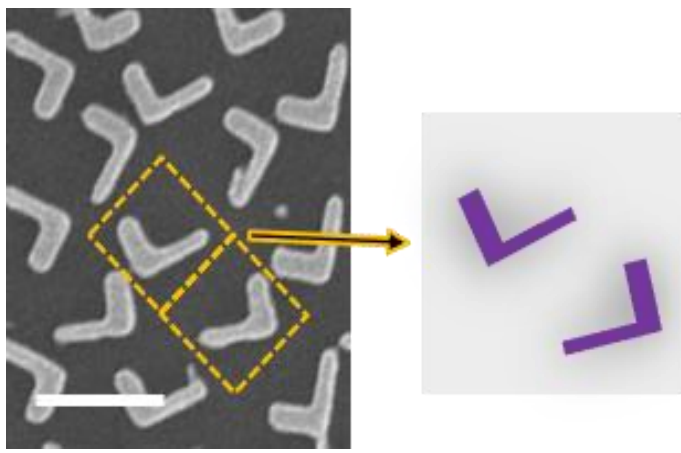

Figure 3.8 Representative SEM image with schematics shows the unit cell of the structure. The yellow dotted rectangle is unit cell and repeated left and right and up and down to form final device. Scale bar: 550 nm

For experimental verification, sample is fabricated using standard electron beam lithography. As shown in Fig. 3.8, unit cell consists of two LSMAs, which have an enantiomeric relationship with each other, and they are arranged in a 45-degree inclined form, rather than a square arrangement, in order to have the smallest period value, which is 551 ($\approx 390\sqrt{2}$)nm. This increases the expression range for the *k*-space of the resulting device. A total number of 501 unit cells are arranged in one direction, resulting in a size of approximately 276 × 276 μm^2. The experimental setup is set as shown in the Fig. 3.9, which is 2-*f* system devised to observe the Fourier domains of transmission space and the reflection space according to different polarization directions. The two lenses in front of the metasurface not only reduce the beam width of the laser, but also help to Fourier transform the reflected information by placing a beam splitter between the two lenses. Two types of

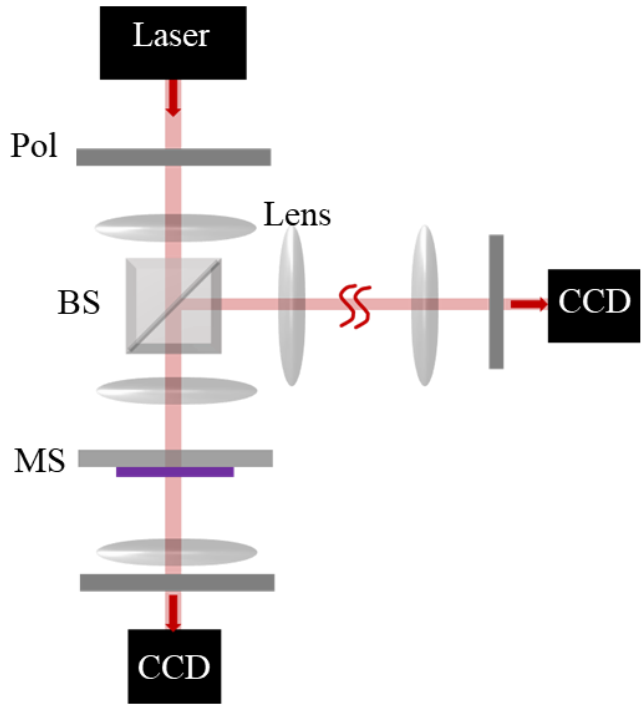

Figure 3.9 Schematic illustration for the experimental demonstration of proposed metasurface. Pol: polarizer, BS: beam splitter, MS: metasurface

samples are made for different purposes. One is a sample that can send different holograms in each direction, and the other is made to have different phase gradient values so that the scattered light at transmission and reflection can vary. The second sample, especially, is for calculating the signal-to-noise ratio (SNR) of proposed metasurface and comparing it with abovementioned ER. The design of the given device was aimed at 633 nm, but the observed wavelength range was specified from 500 to 700 nm in anticipation of a fabrication error.

Notably, from the schematic illustration of Fig. 3.8, one can think that the coupling from adjacent unit cell may result in the degradation of performance, even giving rise to the failure of abovementioned principle of LSMA. It is because in the form of spatially varied arrangement of LSMA,

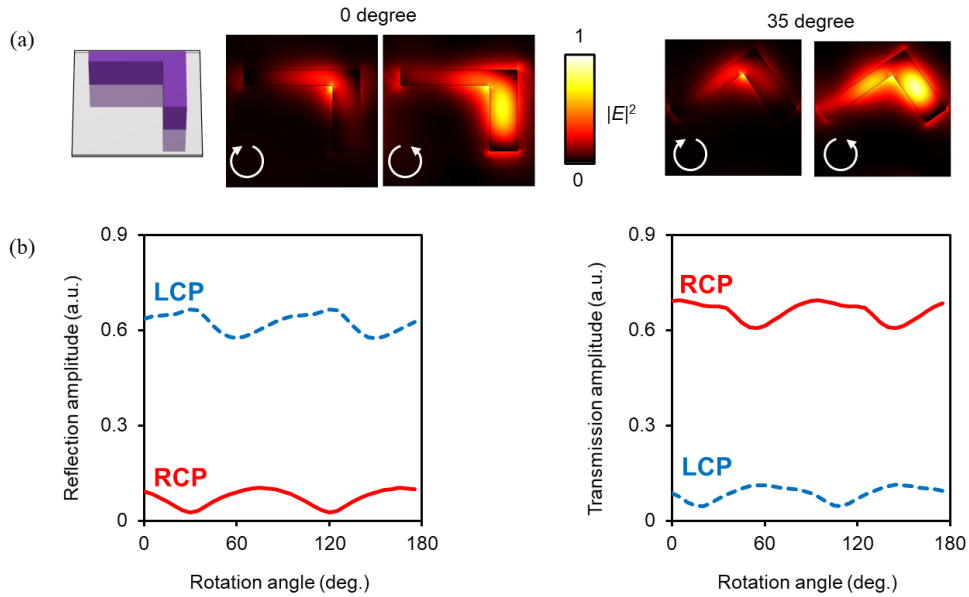

Figure 3.10 (a) schematic diagram showing electric field distribution varied by incident light direction and rotation angle. (b) Reflection and transmission curve by rotation angle of LSMA.

the adjacent LSMAs can be too close together, and this raises concerns that two LSMAs may stick to each other. However, considering the pixel pitch (=390 nm) and maximal length which LSMA can occupy at its most (= 366 nm), the uniting phenomenon cannot happen. Also, it is well-known that if the field is confined in the meta-atom, the meta-atom operates like that it exists in periodic arrangement regardless of rotation [29]. The Fig. 3.10a shows the magnetic field distribution of LSMA when CP light is incident, and most light field is concentrated on the meta-atom, not in the surroundings of meta-atom. Furthermore, when the LSMA is rotated to 35°, which is the condition when LSMA is the closest to the adjacent structures, the operation is preserved, as shown in Fig. 3.10b. Even in other rotation angles, the LSMA operates as expected. As a result, it can be said that the LSMA of the determined parameters is proved to work well in any arrangement condition.

3.4.2 Hologram generation and beam deflection using LSMA

Fig. 3.11a schematically shows how the first sample works. When the polarization direction of the shining light is selected as the + direction, “ABCD” of uppercase letters and different sizes is observed in the transmission space, and lowercase letters “abcd” is observed in the reflection space. When the polarization direction is changed to orthogonal counterpart, letters that have previously at the transmissive space moves to the reflection space, and the characters in the reflection space are measured in the transmission space. The Gerchberg-Saxon (GS) algorithm, a well-known algorithm for computer generated hologram, is used to encode hologram

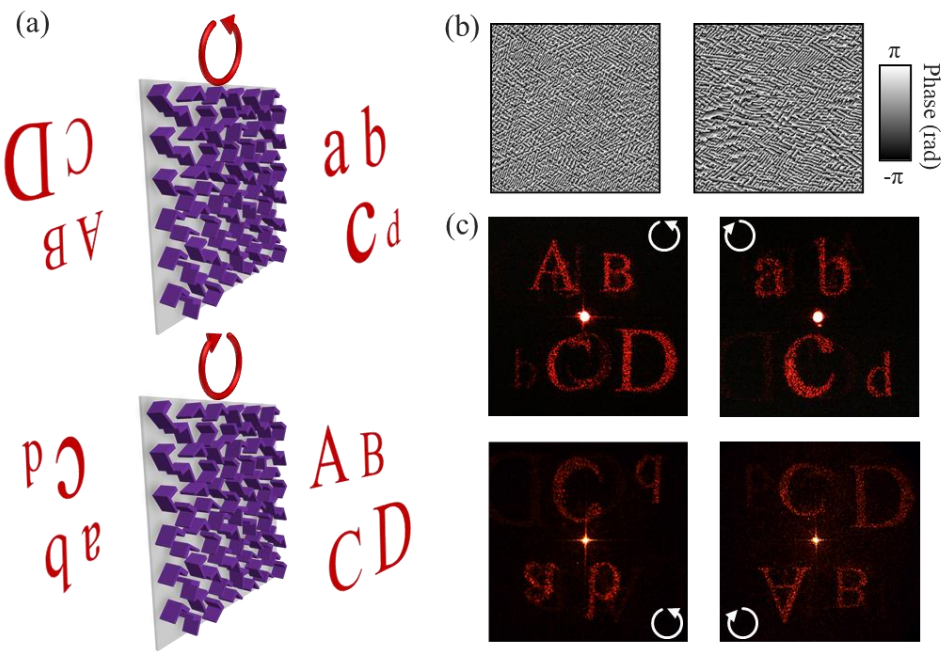

Figure 3.11 Hologram generation using proposed metasurface. (a) Schematic diagram showing operation of sample for hologram generation (b) Phase profiles for “ABCD” (left) and “abcd” (right), respectively, retrieved by GS algorithm. (c) Experimental results using sample for hologram. Upper two images are from transmission space, and lower two are from reflection spaces. White arrows indicates the input polarization of incident light.

profile on the designed metasurface, and the results can be seen in Fig. 3.11b. The results measured at a wavelength of 633 nm through the experimental setup described in Fig. 3.9 are shown in Fig. 3.11c. It shows that not only the reproduced image changes according to the polarization, but also the position at which it is reproduced, which show the desired operation of fabricated device. Interestingly, the unintended images are reproduced together in the form of noise, which seems due to the fabrication error. The strength of this noise varies with the change of the wavelength being measured, as shown in Fig. 3.12, which shows further results showing measured holographic images according to the wavelengths.

The sample for beam deflecting sample is designed as follows: First, to show the feature of proposed metasurface that is differentiated from the

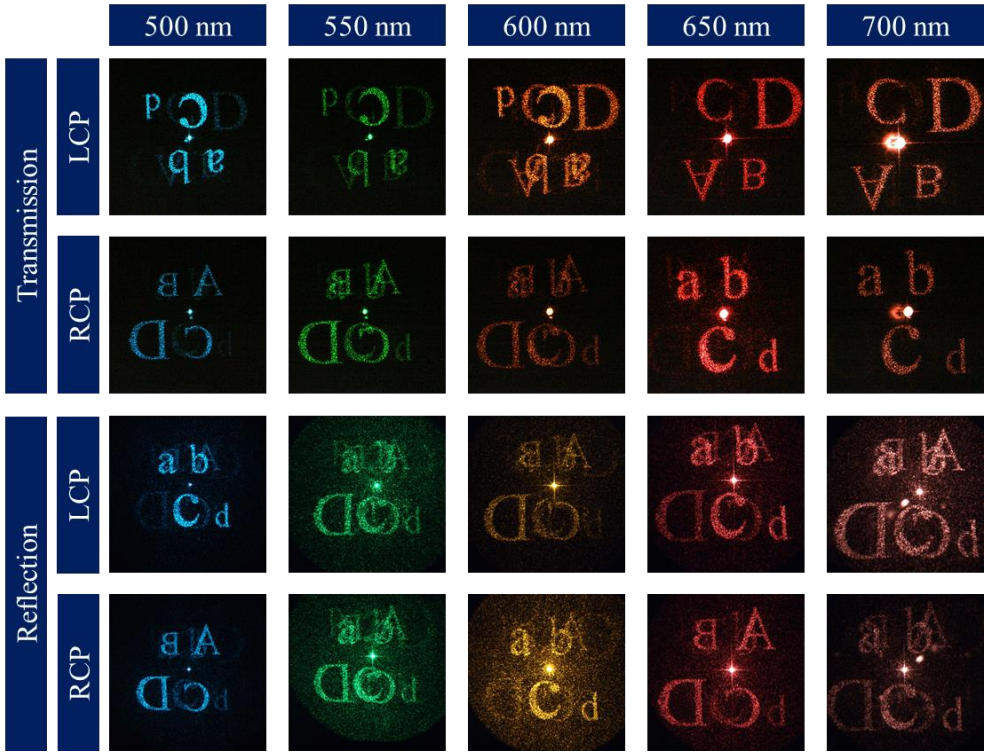

Figure 3.12 CCD-captured images varied by the wavelength of incident light.

conventional metasurface, it makes the transmitted and reflected light propagate to different direction, *x*- and *y*-direction, respectively. Note that it is intended in + polarized light incidence condition, and like above sample, this scheme is reversed by incident handedness. The deflection angle is designed to be 20 degrees to both spaces when normal incidence condition, Therefore, the angle is designed to differ by 53.6 degrees for each LSMA, calculated by $\pi P \sin 20° / \lambda$ by generalized Snell's law. This operation is well summarized in Fig. 3.13a, showing polarization dependent operation by color. Like sample for holographic generation, the propagating direction of *-y* in transmission space at RCP incidence (expressed by red color) is observed in

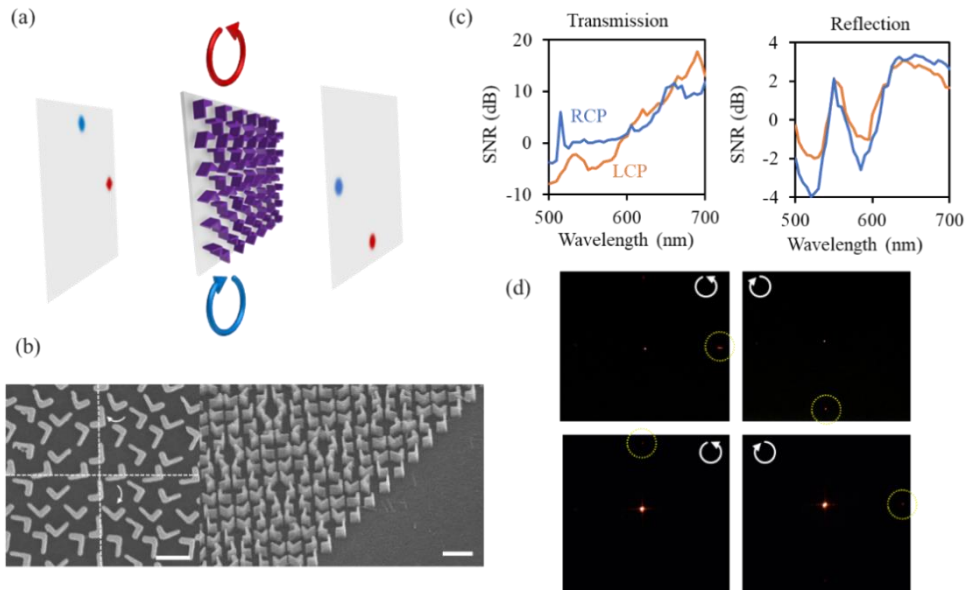

Figure 3.13 (a) Schematic diagram showing the operation of the beam deflection sample by proposed scheme. The polarization sensitive operation is shown by color differentiation: when the source is LCP (RCP), it is blue (red). (b) SEM images of fabricated sample. The LSMA and its enantiomeric counterpart show different direction-dependent rotating property. Scale bar: 500 nm. (c) Line plot showing SNR varied by wavelengths. Each plot graphs are retrieved in transmission and reflection spaces, respectively. (d) CCD captured results distinguished by space and input polarization. Upper two are results in transmission, and lower two are in reflection. Dotted yellow circles are for clarification of desired diffraction order.

reflection space as +*y* at LCP incidence (by blue color). The SEM image of fabricated sample is shown in Fig. 3.13b, and this shows the direction in which the angle is changed differs depending on the structure. As mentioned above, the SNR is calculated for revealing the performance of LSMA. The signal is defined as the diffraction efficiency of desired order, and noise is the intensity sum except for the signal. For example, when SNR is desired in transmission space, the CCD-captured results by two incident polarizations exist. If the incident polarization is + polarized (LCP), desired diffraction order is -1 in *x*-direction. Therefore, the number of resultant SNR is four, which are distinguished by two input polarizations and two spaces per one sample (Fig. 3.13c). At target wavelength of 633 nm, SNR is 6.81 dB (LCP), 5.61 dB (RCP) in transmission, and 2.85 dB, 3.25 dB in reflection. If it was made as intended, it should have a similar result to Fig. 3.4b. The tendency according to wavelength is similar, but the wavelength of maximum value is redshifted in transmission, which is 17.7 dB when LCP light of 690 nm is illuminated. This tendency holds true in SNR of reflection of which the maximal value is 3.08 (3.36) dB when LCP (RCP) light of 640 (655) nm is incident light source. This can happen when the sample is made a little larger than desired. The CCD-captured result at the target wavelength of 633 nm is also shown in the Fig. 3.12d, showing desired operation of asymmetric beam deflection and polarization dependent space conversion as well.

3.5 Conclusion

In this chapter, metasurface that enables polarization dependent space conversion is presented. Using LSMA as unit structure, the magnitude variation of cross-polarized component according to the handedness of CP light is achieved. Especially, it is designed so that when + polarized light is incident, cross-polarized transmission is suppressed, and when – polarized light is used as excitation light source, cross-polarized reflection becomes zero. Using geometric phase and interleaving it with enantiomeric counterpart, independent phase control at transmission and reflection is achieved. Notably, as novel operation, by handedness change of incident CP light, the transmitted phase profile can be transferred to reflection space and at the same time, the reflected phase goes to transmission, which is called space conversion. Using asymmetric beam deflection and holographic image generation, the unique property of proposed metasurface is presented. Note that the space conversing scheme is demonstrated using LSMA, but it can be regarded as a realization by principle. Also, by polarization change of incident light, the space conversion is verified experimentally. We are expecting this scheme can contribute to the suggestion of new form factor in existent optical design by virtue of novel operation.

Chapter 4 Switching modulated space by arbitrary polarization pair

4.1 Introduction

One of the important branches of light control which becomes possible with metasurface is to implement phase gradient. Indeed, the phase gradient metasurfaces (PGMs) have been utilized in the past for acquisition of desired light beam trajectory by generalized Snell's law (GSL) [14, 67-69]. That is because the light rays obtain additional transverse wavevector by phase gradient, which results in the anomalous refraction or reflection [70]. However, GSL is found to be insufficient to explain the light beam path especially when light impinges with critical angle condition. In this condition, the lattice vector of periodic structure replaces the phase gradient and this reveals various interesting phenomena, such as high order diffraction, asymmetric transmission and retroreflection, etc [71-74]. However, while the inherited physics is theoretically revealed in past studies, devices utilizing relevant content are still rare [75, 76]. Since the current research framework of metasurfaces which modulates the full-space lacks in polarization response, the combination of the phase gradient for asymmetric transmission and conventional polarization multiplexing scheme may pave the way to novel polarization-selective full-space control in electromagnetic regime.

In this chapter, a metasurface platform is proposed, which achieves asymmetric transmission according to the polarization states of incident light, and at the same time, conveys two independent phase profiles to each space. We utilize the birefringent nanopillar as unit to impart different phase profiles

at two arbitrary orthogonal polarization. Next, we show that the transmissive metasurface possessing specific phase gradient can be utilized to reflection-type using the critical angle condition [73]. As a result, the control of transmission and reflection can be realized by polarization of the incident light, and at the same time, their phase can be determined independently. The fabrication and measurements of proposed scheme is also conducted with two examples (beam steering and holographic image generation) and verified with three different polarization pairs. Contrary to other implementations, here the proposed scheme considers the full-space modulation. We expect our metasurface design to be applied in a diversity of optical setups thanks to its compact but outstanding ability of light manipulation at full-space, guiding a new way to simplify the existing system. Moreover, as a holographic storage, this scheme may open a new horizon for image encryption, decryption and real 360° vectorial hologram.

4.2 Basic metasurface design

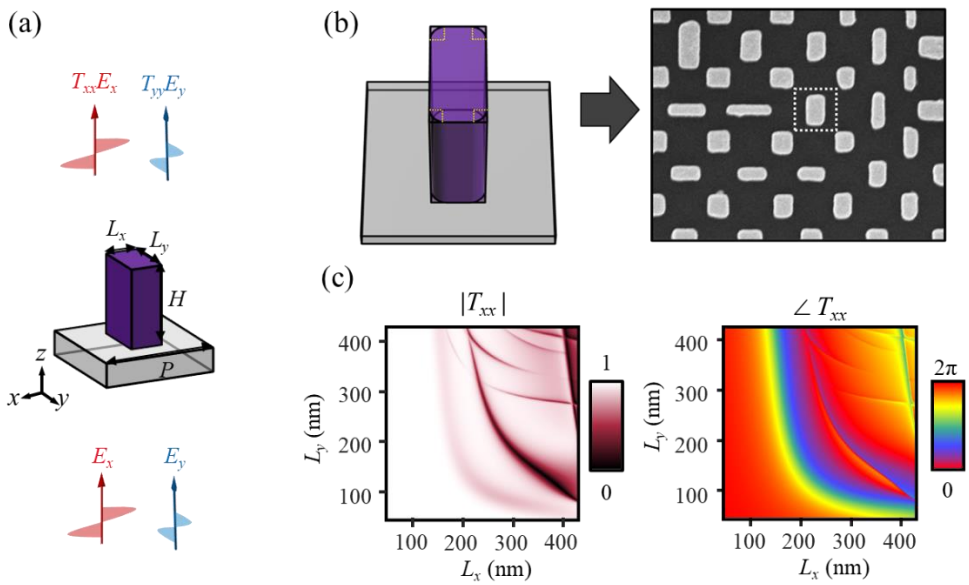

Figure 4.1 Schematic diagram and transmission coefficients of nanopillar, which is used as unit structure throughout this article. (a) Schematic diagram of rectangular nanopillar expressed with structural parameters. The structure is illuminated from the bottom. (b) Schematic diagram and SEM captured image showing how the meta-atom is structured and made in simulation and experiment. (c) Simulation results of amplitude and phase of transmission T_{xx}, while varying L_x and L_y of single nanopillar.

The basic framework of the proposed metasurface consists of amorphous silicon rectangular nanopillar on quartz substrate, as shown in Fig. 4.1a. The material choice is attributed to the high index and low absorptivity at 980 nm wavelength ($n_{\mathrm{Si,980\ nm}}$ = 3.6+0.013i). Unit cell has 450 nm pixel pitch (P in Fig. 4.1a) that is determined not to cause diffraction considering the refractive index of the substrate (SiO_2, n = 1.44). Each nanopillar has 500 nm height (H in Fig. 4.1a), which is about half the wavelength in free space (980 nm), optimized to have high transmittance (0.8~1) and enough birefringence at the same time. Finite element method simulations were performed using a

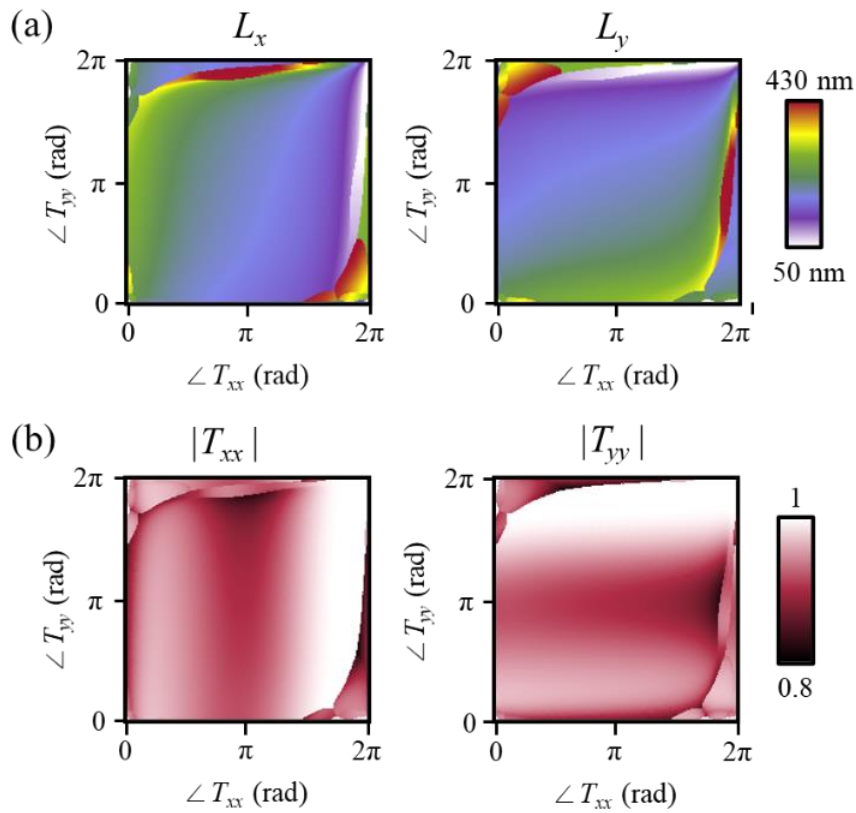

Figure 4.2 Structural parameter and amplitude data set used in the main text sorted by the desired phase values of T_{xx} and T_{yy}. (a) Colored plot graphs of structural values of L_x and L_y. Coordinate values indicate the lengths of corresponded phase values of T_{xx} and T_{yy}. (b) Colored plot graphs of amplitudes, corresponding to the Fig. 4.2a.

commercially available software (COMSOL Multiphysics). To avoid unphysical scattering and provide better agreement with the experimental results, the simulations consider pillar with rounded edges (Fig. 4.1b). The amplitude and phase of T_{xx} and T_{yy} are obtained while varying structural parameters L_x and L_y from 50 nm to 430 nm, as shown in Fig. 4.1c. From this computed result, one can find the nanopillar that minimizes the mean squared error calculated as follows:

$$E = \left|T_{xx} - e^{j\phi_1}\right|^2 + \left|T_{yy} - e^{j\phi_2}\right|^2 \tag{4.1}$$

where ϕ_1 and ϕ_2 are desired phase values. Using eq. (4.1), we obtain the structural information of the nanopillar which delivers the phase of ϕ_1 and ϕ_2 to *x*- and *y*-polarized light, respectively. For detailed parameter set, see Fig. 4.2. This phase shift disparity by incident polarization stems from the effective propagation length difference by the shape of the nanopillar. This property makes the proposed platform sensitive to wavelength changes.

In addition, several previous studies revealed that this linearly birefringent metasurface platform can also impart two different phase shifts into other polarization pairs [21, 28]. It is possible by introducing the in-plane rotation angle to the nanopillar. For example, if the circularly polarized light shines the nanopillar, the cross-polarized component of the transmission is expressed as:

$$T_{\text{cross}} = (T_{xx} - T_{yy})e^{j2\sigma\theta} / 2 \tag{4.2}$$

where σ is the parameter determined by the handedness of circular polarization of the incident light, and θ is the rotation angle of the nanopillar, shown in Fig. 4.3. Herein, σ is +1 or -1 for right or left circular polarization, respectively. According to eq. (4.2), the phase of T_{cross} is dependent on the handedness of polarization due to the part of $e^{j2\sigma\theta}$. As the amplitude and phase of (T_{xx}-T_{yy}) are controllable by the dimension of nanopillar, the maximal value of T_{cross} with two independent phase shift values by input circular polarization can be achieved. When it comes to the elliptical polarization pair, this is also achievable. Derivation can be retrieved by Jones matrix calculation: Since the linear and circularly polarization pair is intuitive and well-known by the several papers, the general case of elliptical polarization basis is explored here.

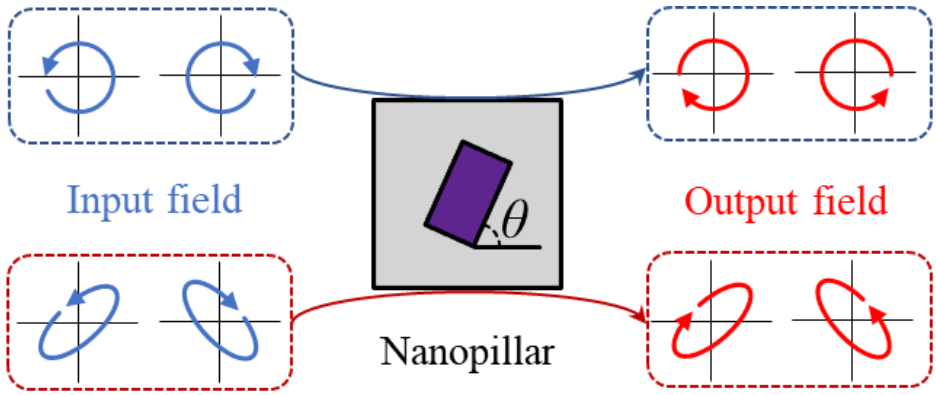

Figure 4.3 Conceptual schematic for explanation of mechanism of phase modulation of arbitrary polarization pair. When the nanopillar rotation is introduced, the phase modulation at arbitrary polarization pair is possible with flipped handedness as described in the text.

We consider the case of generalized elliptical polarization pair, which are expressed as follows through the Jones matrix,

$$\mathbf{E}_{\phi} = (\left|E_{\phi 1}\right\rangle, \left|E_{\phi 2}\right\rangle) = \left(\frac{1}{\sqrt{2}} \begin{bmatrix} 1 \\ e^{i\phi} \end{bmatrix}, \frac{1}{\sqrt{2}} \begin{bmatrix} -1 \\ e^{i\phi} \end{bmatrix} \right), \tag{4.3}$$

where $\mathbf{E}_{\phi}$ denotes the basis matrix of electric field direction of input light that is orthogonal to each other component, and ϕ is the phase difference between *x*- and *y*-directional electric field at incident light. Considering that the phase retardation in linear polarization basis of meta-atoms and rotation angle in *xy*-plane is freely adjustable, Jones matrix of meta-atom that is equivalent to scattering effect can be written as

$$\mathbf{J} = \mathbf{R}(\theta) \begin{pmatrix} e^{j\phi_{xx}} & 0 \\ 0 & e^{j\phi_{yy}} \end{pmatrix} \mathbf{R}(-\theta), \tag{4.4}$$

where θ is rotation angle of each meta-atom with respect to *x*-axis, and **R** is well-known 2 by 2 rotation matrix expressed as

$$\mathbf{R}(\theta)=\begin{pmatrix}\cos\theta & -\sin\theta\\ \sin\theta & \cos\theta\end{pmatrix}. \tag{4.5}$$

Here, when the incident light is expressed by eq. (4.3) and incident onto meta-atom, the scattering matrix expressed by polarization of which the handedness is flipped from incident one can be written as follows,

$$\begin{aligned}\mathbf{T}_{-\phi\phi}&=\mathbf{E}_{-\phi}^{-1}\times\mathbf{J}\times\mathbf{E}_{\phi}=\begin{pmatrix}\langle E_{-\phi1}|E_{\phi1}\rangle & \langle E_{-\phi1}|E_{\phi2}\rangle\\ \langle E_{-\phi2}|E_{\phi1}\rangle & \langle E_{-\phi2}|E_{\phi2}\rangle\end{pmatrix}\\ &=\frac{e^{i\phi}}{2}\begin{pmatrix}ae^{i\phi_{xx}}+be^{i\phi_{yy}} & ce^{i\phi_{xx}}-\bar{c}e^{i\phi_{yy}}\\ ce^{i\phi_{xx}}-\bar{c}e^{i\phi_{yy}} & \bar{b}e^{i\phi_{xx}}+\bar{a}e^{i\phi_{yy}}\end{pmatrix}\end{aligned} \tag{4.6}$$

where a, b, and c are the derived complex coefficients as below,

$$\begin{aligned}a&=\cos\phi+\sin 2\theta-i\cos 2\theta\sin\phi,\\ b&=\cos\phi-\sin 2\theta+i\cos 2\theta\sin\phi,\\ c&=-\cos\phi\cos 2\theta+i\sin\phi.\end{aligned} \tag{4.7}$$

The upper bar in eq. (4.6) indicates the conjugate value of corresponded parameter. It is notable that the non-diagonal components have same values. Therefore, considering the energy conservation law, when the absolute values of non-diagonal components in $\mathbf{T}_{-\phi\phi}$ are zero, the absolute values of diagonal components, which are handedness-flipped polarized components from incident light, become the highest value of unity. From eq. (4.6), the zero absolute value condition of non-diagonal components can be expressed as below,

$$\phi_{yy}-\phi_{xx}=2\angle c \tag{4.8}$$

Furthermore, since the phase difference between two diagonal components is also achievable with fine-tuning of $\phi_{xx}+\phi_{yy}$, it is possible to impart two distinct phases for arbitrary polarization pair with linearly birefringent meta-atom. It

is notable that unlike the condition in which the linearly polarized light is used, the component to which the phase is added is the handedness-flipped version of incident light (see Fig. 4.3). As a result, for arbitrary polarization pair, the polarization multiplexed phase control is realized.

4.3 Phase gradient metasurface for reflective operation

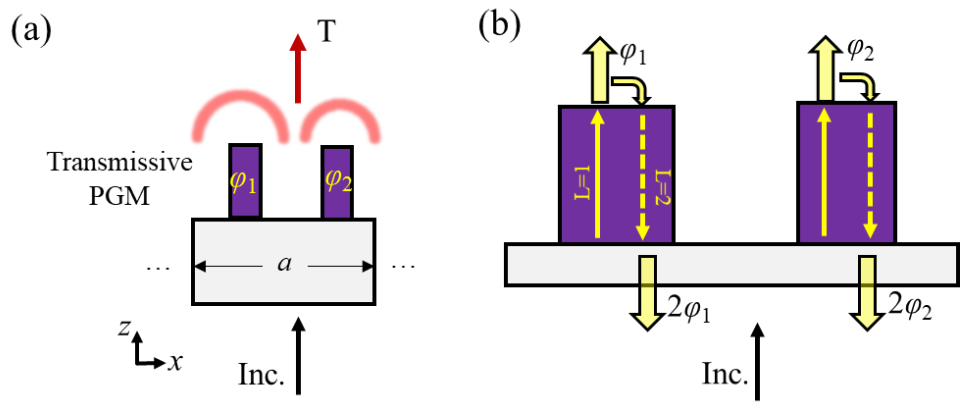

Figure 4.4 Conceptual diagrams of proposed phase gradient metasurfaces for explanation of mechanism of desired scheme. (a) Schematic illustration of transmissive PGM consisting of two meta-atoms (m=2). The period of supercell is a, assuming that the meta-atom is transmissive and having gradient value of $2\pi/a$, the light is bent by addition of corresponding momentum as shown. (b) Schematic illustration for showing transmissive PGM of m=2 and phase behavior when the direct transmission (L=1) and induced reflection (L=2) appear.

In this section, we provide a method which allows us to obtain induced reflection using PGM [73, 75]. Our scheme can be explained with the integer parity design of two meta-atoms, assisted by the diffraction law of parity reversal and critical angle condition to demonstrate the reflective operation from transmissive type device [73]. Suppose that transmissive PGM of periodicity a is designed with gradual phase shift values from m nanopillars, $\varphi_i = 2\pi i / m$ from i-th nanopillar in Fig. 4.4a. Here, the nanopillars could be regarded as light waveguides. The light leakage into the free space between nanopillars is neglected because light scattering is mostly attributed to the modes excited in nanopillar. When the light impinges normally into this PGM,

the diffraction mechanism regarding wavevectors of output rays is well-known to obey the following equation by GSL,

$$k_{t,r} = k_{in} + \xi, \tag{4.9}$$

where $k_{t,r}$ is momentum of light along x-direction in transmission/reflection space, and k_{in} is transverse momentum of incident light, and ξ is the phase gradient of PGM, expressed as $2\pi/a$. It is well-known that according to eq. (4.9), in case of $\xi < |k_0|$, the output light experiences direct transmission of trajectory determined by additional momentum of ξ. Intriguingly, however, if the momentum of PGM is enlarged beyond the wavevector in transmission space ($\xi > k_0$), the wave cannot proceed to transmission space directly. It is called critical angle condition, which makes the resultant diffraction apart from GSL. In the critical angle condition, how the light proceeds cannot be explained by GSL, and it is determined by the following equation called diffraction law of parity reversal [73],

$$k_{t,r} = k_{in} + \xi + (n-1)G = k_{in} + nG, \tag{4.10}$$

where n is the diffraction order and G is reciprocal lattice vector of the supercell structure, which is the same value as ξ, but possesses different physical meaning. Thereupon, the light undergoes the back propagation in nanopillar, as shown in Fig. 4.4b. In this circumstance, this doubles the phase retardation from each nanopillar ($2\varphi_i$) because of the additional propagation in the nanopillar. If the number of this back and forth propagation in nanopillar is parametrized as L, the phase retardation from i-th nanopillar becomes $L\varphi_i$ [73]. It is worth mentioning that among the propagation process, the diffraction occurs if the coupling is possible into corresponding diffraction

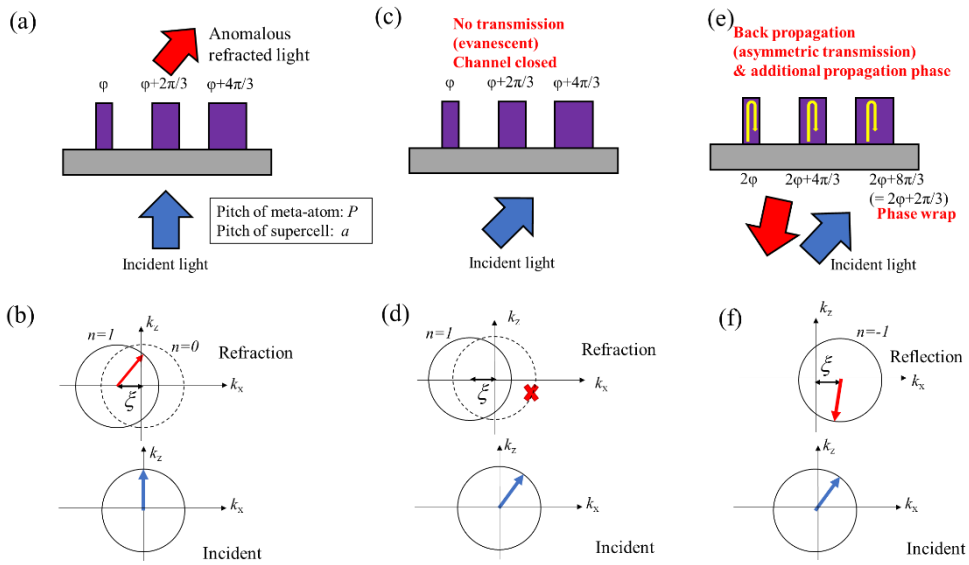

Figure 4.5 Procedure of how diffraction occurs when critical angle condition is met. (a) The condition when the diffraction can be explained with GSL. (b) Equifrequency contour. From bottom, the light is normally illuminating to structure, yielding anomalous refraction. (c) Schematic of obliquely incident light when critical angle condition is met. (d) Equifrequency contour described by GSL. (e) Schematic diagram showing the induced reflection. (f) Corresponded equifrequency contour.

order according to eq. (4.10). In short, this phenomenon can be summarized with abovementioned parameters, which is revealed by previous studies, expressed as:

$$L = m + n. \tag{4.11}$$

In this chapter, we will only deal with the L=1 (direct transmission) and L=2 (induced reflection). The detailed information of how the light trajectory is determined can be understood by equifrequency contour. As shown in the Fig. 4.5a, the diffraction is decided by the GSL when the incident angle is not in the critical angle condition. The solid circle at the bottom (Incident) represents the equifrequency contour of incident light. Blue arrow shows the direction of incident light, and red arrow at the upper graph (Refraction) represents the propagating direction of refracted light. The dashed circle in

refraction is the contour for reference when there is no phase gradient by the structure. On the other hand, the solid circle is the shifted contour by phase gradient ξ, order of n=1 by GSL. As shown by the direction of red arrow, the propagating direction of refraction can be accesssed. The equifrequency contour of diffraction order shows the beam trajectory of refracted beam, as shown in contour at Fig. 4.5b. Note that the contour is described according to eq. (4.9), which is same when n=1 in eq. (4.10). According to the contour, the fact that the refracted beam of the critical condition when k_{in} is bigger than k_0-ξ cannot be explained by GSL (Fig. 4.5c-d). By GSL, the refracted light cannot exist, because the momentum becomes bigger than the free space wavenumber k_0. This is when the light propagates backward because there is no diffraction channel for light beam to proceed. As the refraction by GSL is not possible, the wave propagates back into reflection space, yielding two times of propagation phase. This, in turn, results in the diffraction having order of n=-1. The diffraction order n can be obtained using eq. (4.11), so rather than GSL, diffraction law of parity reversal should be utilized in critical angle condition. With induced reflection, the light is retarded by propagation phase of each nanopillar again. As a result, the diffraction occurs in reflection with opposite sign of transmission, considering the 2π phase wrap as shown in Fig. 4.5e. As a result, the diffraction order becomes n=-1 (Fig. 4.5f). Therefore, the equifrequency of GSL cannot explain the diffraction from induced reflection. In the critical angle condition, diffraction is determined by eq. (4.11) (n = 2(L)-3(n)), and the generated diffraction order n follows the eq. (4.10), which is generalized case of abovementioned example.

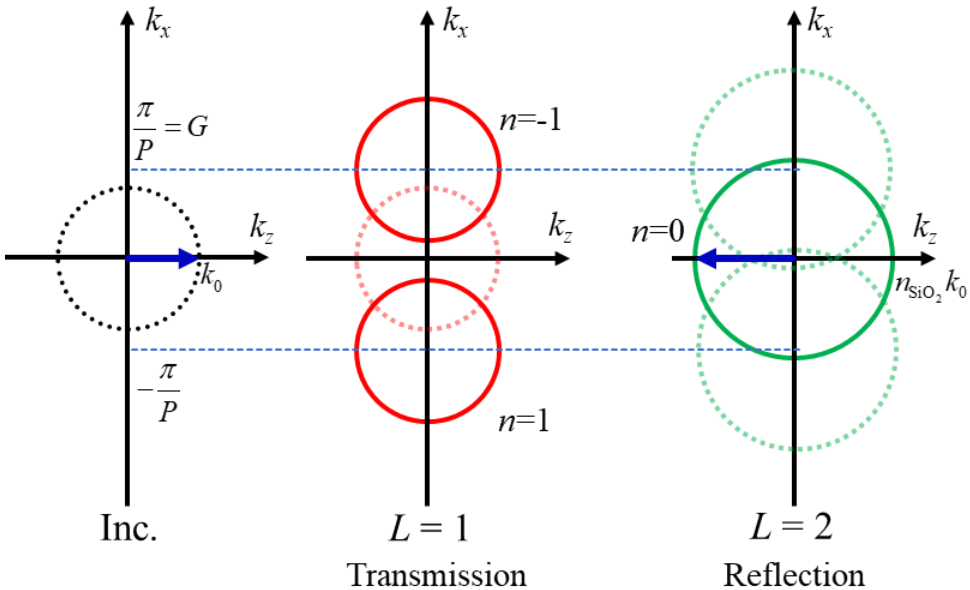

Figure 4.6 The equifrequency contours of PGM when a=2P. Red circles are transmission contour graphs and the green circles are the reflection contours. The solid (dashed) circles are coupling-possible (-impossible) contours of diffraction orders solved by eq. 4.10. The blue arrows show the directions of incident and output light. Since the surroundings are different at transmission and reflection spaces, the radii of contours differ from each other.

Next for numerical demonstration of induced reflection L=2, the supercell structure consists of two meta-atoms (m=2) for exhibiting phase gradient $\xi=\pi/P$. Since the structure is composed of two meta-atoms, the diffraction law of eq. (4.10) is modified as below,

$$k_{t,r} = k_{in} \pm nG. \tag{4.12}$$

Namely, if one nanopillar conveys phase φ to transmission, the other nanopillar is chosen to impart phase of $\varphi+\pi$, which is out-of-phase. According to eq. (4.12) and as shown in the equifrequency contour at Fig. 4.6 of above condition, the incident light (expressed in blue arrows) cannot be coupled to order n=1. This is because the generated phase gradient value π/P (=6.98×10^6 1/m) is slightly greater than the wave momentum at the free space k_0

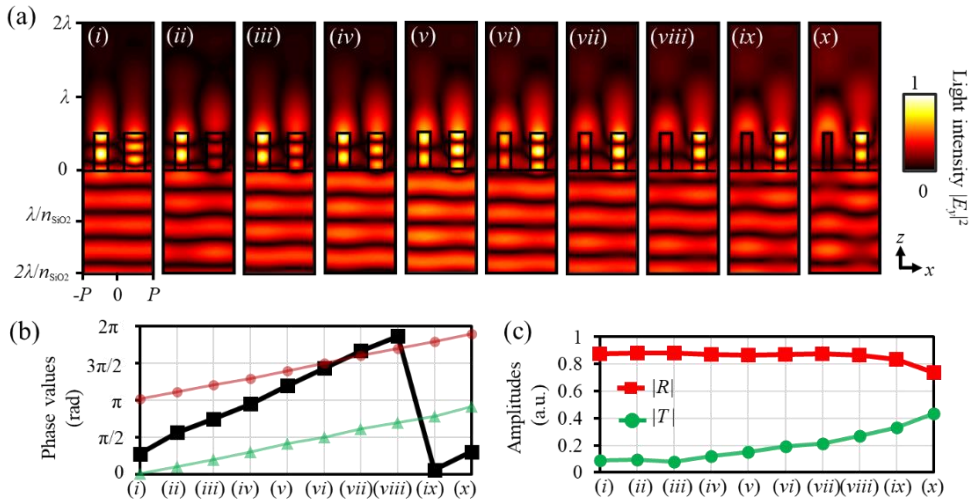

Figure 4.7 Simulated results showing the induced reflection. (a) The light field intensity patterns from ten selected structural parameter sets. The electric field is directed in *y*. The interference pattern shows the light is mostly reflected. The square nanopillars in one set have phase values that are out-of-phase to each other, which means identical phase gradient. Their original phase values in transmission can be observed in (b), and they are increasing values maintaining identical phase gradient. Green triangles are phase values from right nanopillar, and red circles are from left. The reflected phase values of (*i*-*x*) are also shown in black squares, which are two times of the transmissive phase shift. (c) Transmission and reflection amplitudes from (*i*-*x*). Red squares are reflection and green circles are transmission

(=6.41×10^6 1/m), which means the critical angle condition. In this condition, the direct transmission (L=1) cannot occur. As a result, the reflection is induced (L=2), and since the supercell is composed of two meta-atoms (m=2), the light is reflected (n=0). In this condition, the reflected light undergoes phase change of 2φ.

For square pillar which imparts same phase shift values regardless of input polarization, the induced reflection is numerically demonstrated. The structural information is extracted from Fig. 4.2, and their square widths are adopted for imparting phase values showing out-of-phase condition to each other. Total ten structural parameter sets are adopted, and their phase values differ by $\pi/10$. Since the phase values are doubled at induced reflection as

shown in Fig. 4.4b, each nanopillar imparts same phase shift to reflection. As shown in Fig. 4.7a, most of light intensity goes to the reflection spaces at all examples. The reflected phase shifts by two nanopillars are twice the gradient of the original phase shifts ($L\varphi_i$ when L=2) as expected, and it is shown in Figs. 4.7a, b. The light cannot proceed to the transmission space due to abovementioned theory, so the evanescent field can be observed as shown in Fig. 4.7a. Their corresponded reflection and transmission amplitudes are also calculated in Fig. 4.7. The reason for leakage to transmission is the mismatch of the transmission amplitudes of original nanopillars and relatively low light confinement into nanopillars. It is worth mentioning that in reflection, one may think that the wave is able to be coupled into diffraction order n=1 and -1 in reflection space, but it is possible if the light energy (i.e. induced current density, normalized magnetic energy), which dominates the scattering characteristics of each nanopillar, is not confined into PGM but into adjacent free space. This makes the induced reflection hard to be generated, which contributes to the main reason for mismatch between analytical and numerical result. In our design, it means that if the relatively low index materials (i.e. GaN, TiO_2, GaP, etc.) are adopted, the improved feature can be realized.

By using the design method discussed in the previous section and induced reflection here, the metasurface is designed to operate like polarizing beam splitter (PBS). Using the fact that one nanopillar can impart two independent phase values and PGM can be used to induce reflection from transmissive metasurface, two nanopillars are combined to unit cell for realization of unprecedented operation in metasurfaces: Firstly, this metasurface can split incident light into totally different spaces of transmission and reflection,

distinguished by polarization states. Former studies already have succeeded in beam split by polarization, but they hardly divide beam trajectory into full-space, especially in optical frequency regime. Secondly, the phase shift value can be independently imparted to both spaces. It is possible through using linearly birefringent nanopillars where the light reaction varies by the polarization state. As an example, assume that the designer wants to design a nanopillar that imparts the phase values of φ_1 and φ_2 into transmission and reflection, respectively, and at the same time, wants the light to be split by linear polarization basis. Basically, for reflective operation, the unit structure should have two nanopillars. As discussed in this section, two nanopillars are for generation of phase gradient bigger than wavevector at free space. If *x*-polarization is chosen to be at transmission, then two nanopillars are designed to impart the identical phase of φ_1 for *x*-polarized light. On the other hand, for *y*-polarized light, two nanopillars need to operate in reflective type. It is possible by induced reflection of L=2, which is realized by two nanopillars conveying the phase of $\varphi_2/2$ and $\varphi_2/2+\pi$ at *y*-polarization. Since these phase values give the same condition discussed in this section, induced reflection will have the phase value of φ_2. In detail, simulation results with structural parameters are also provided in Fig. 4.8 in case of linear polarization basis. Since the polarization-selective phase retardation is possible at arbitrary polarization basis as discussed in previous section, this makes polarization-selective full-space phase modulation achievable.

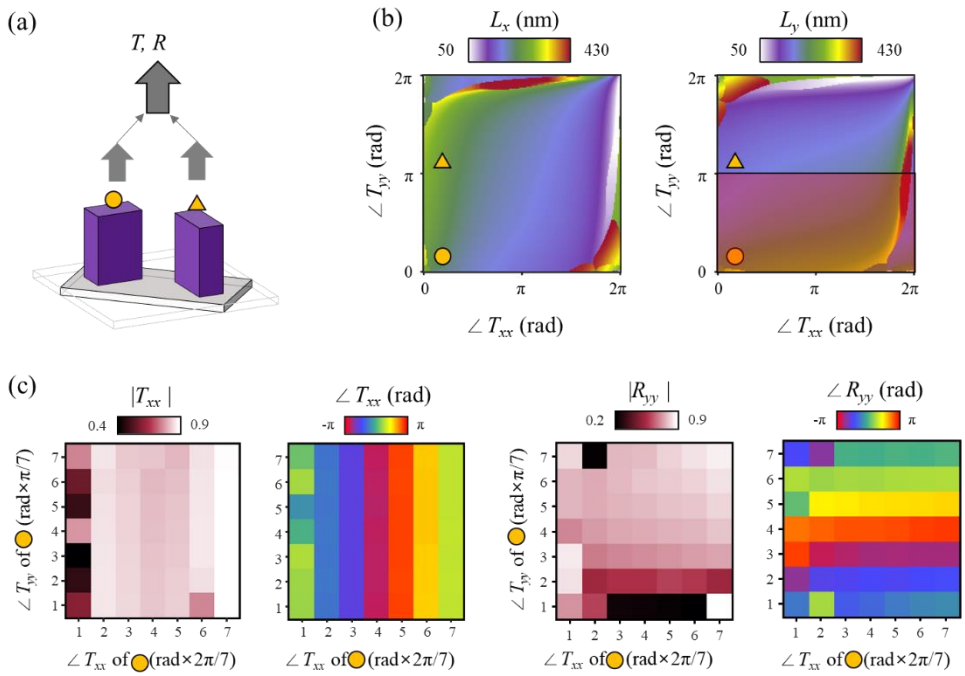

Figure 4.8 Schematic diagram and colored plot graphs for explanation of reflected phase values designed in linear polarization pair. (a) Schematic diagram of two-fold meta-atom unit cell design, and scattered wavefronts from each meta-atom is marked by yellow-colored circle and triangle, respectively. (b) Examples of structural parameters of two meta-atoms exhibiting transmission at *x*-polarized shined condition, and reflection at *y*-polarized shining. They should meet the condition of out-of-phase condition at T_{yy}, while T_{xx}s are in-phase. As results, line that passes circle and triangle both is parallel to *y*-axis. Note that the yellow circle can only be displaced in the red-shaded area, which is for evading the overlapped parameter set. That is in fact related to the reflected: Reflected phase of R_{yy} is determined by the two times of T_{yy} of circle and triangle. (c) Determined phase and amplitude values of T_{xx} and R_{yy} extracted from resultant two-fold meta-atom, calculated by simulation. As shown in the graphs, it is noteworthy mentioning that the scale of *y*-axis is half of the scale in *x*-axis. At the same time, the phase values of T_{xx} and R_{yy} are changing with identical gradients, which means that the phase of R_{yy} changes two times faster than that of T_{xx}.

4.4 Experimental demonstration

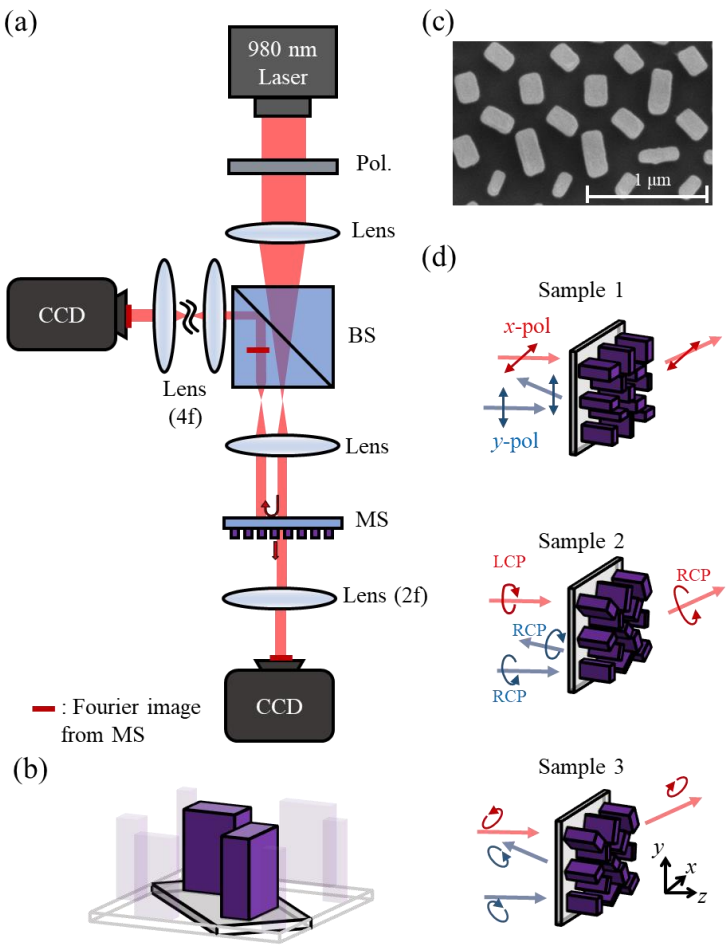

Figure 4.9 (a) Schematic diagram of optical setup for capturing Fourier images of fabricated samples with diode laser of 980 nm wavelength. The input polarizers are subject to change according to the purposes. The two lenses before metasurface are used for collimating the light, and the lenses after metasurfaces are for 2-f system for obtaining the Fourier image of the metasurface. MS: metasurface, CCD: charge coupled device, BS: beam splitter, Pol.: polarizer. (b) Schematic diagram of unit cell composed of two rectangular nanopillars. (c) SEM captured image from sample operating in linear polarization pair. Scale bar: 1 μm (d) Schematic diagrams of three fabricated samples distinguished by polarization pair in operation. For beam steering and hologram generation samples, this notation is preserved.

Throughout this chapter, three types of metasurface are fabricated for experimental demonstration with discussion, distinguished by the operational polarization states. The three selected polarization pair is expressed by phase

difference between electric fields directed at two principal axis of *x*- and *y*-axes, and their values are 0, π/4 and π/2, respectively. The measurement is carried out with optical setup as shown in Fig. 4.9a. The polarizers at output ends are sometimes selectively removed for desired analysis. As mentioned in above section, the unit cell consists of two nanopillars, as shown in Figs. 4.9b, c. The unit cell structure is inclined at 45 degrees, which looks clear in Fig. 4.9b, designed for shortening the period from 2*P* to $\sqrt{2}P$. Samples are fabricated by standard electron beam lithography.

We introduce two operational types for experimental verification of proposed metasurface device: (1) One is beam steering sample which transmits light into transmission and reflection spaces by the input polarization states, and the steering angles at each space are also freely designed. (2) The other is hologram generation sample, and basically same design method is employed with above examples. However, we believe that this sample shows the elemental level of potential of this design scheme because the capacity for holographic generation indicates the possibility of other operation as well, such as orbital angular momentum, lensing, etc. The way that the trajectory of three polarization types is determined is depicted in Fig. 4.9d: The sample operating in linear polarized light splits the *x*-polarized light into transmission space, and *y*-polarized one into reflection space. For sample operating in circular polarization, the incident left-handed circularly polarized (LCP) light transmits to transmission space and polarization is reversed, while right-handed circularly polarized (RCP) light is reflected and reversed in polarization. In case of the elliptical polarized light sample, the polarization direction is just depicted as in-plane arrow in Fig. 4.9d.

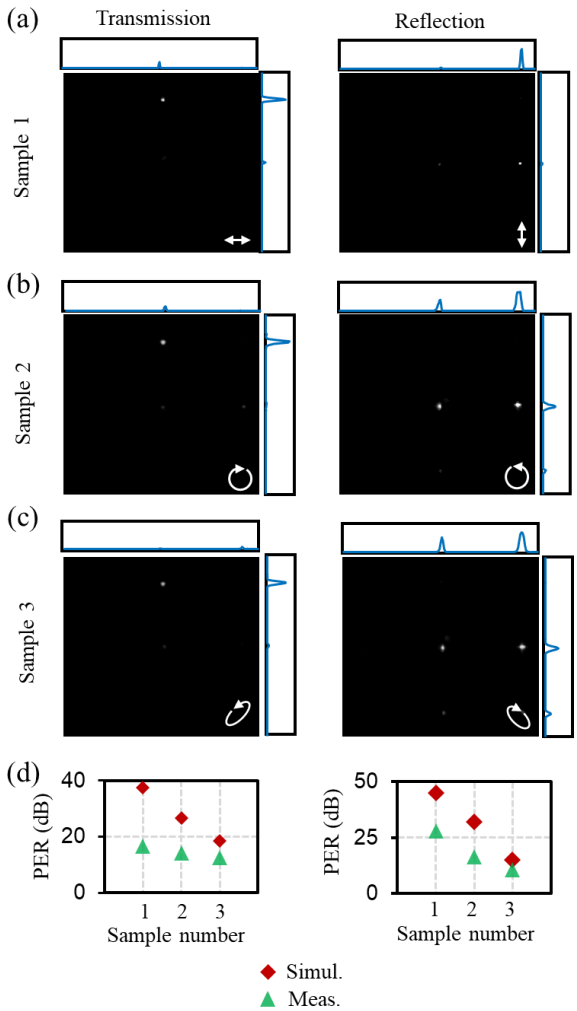

Figure 4.10 Beam steering results from experiment (a-c) CCD-captured images as well as the line graph extracted near the zeroth order diffraction, showing experimental results of diffraction order efficiency. (a) is from sample 1, operating in linear polarization pair, (b) from sample 2 operating in circular polarization pair and (c) from sample 3 operating in elliptical polarization pair. White arrows indicate the polarization states of the input light. (d) Polarization extinction ratio obtained from three fabricated samples. Simul.: simulation result, Meas.: Measured result.

As the first example, we demonstrate beam steering capability of the proposed scheme. Each sample is fabricated with identical operation, having the phase gradient values of which at transmission space, the value is 0.444*P*

Table 4.1 Total diffraction efficiency obtained with FDTD results. a) El_1 (El_2) is the elliptical polarization state determined to operate in transmission (reflection). b) Written in bracket is the efficiency at target diffraction order.

Sample number		**1**		**2**		**3**	
Input polarization		***x*-pol**	***y*-pol**	**LCP**	**RCP**	**El_1**	**El_2**
Total efficiency (%)	**Transmission**	79.34 (76.62)[b)]	21.44	80.46 (77.54)	15.40	77.59 (73.93)	21.41
	Reflection	8.444	57.67 (38.56)	9.376	65.37 (31.04)	11.02	56.95 (14.67)

(=$2\pi/10\sqrt{2}\,P$) to +*y* direction, and in reflection space, it is $0.555P$ (=$2\pi/8\sqrt{2}\,P$) to +*x* direction. Consequently, one periodic structure is composed of total 10×8×2 meta-atoms. Samples are fabricated targeting the size of 200 × 200 μm^2, having about 700 meta-atoms in one line. Their operation is firstly verified by numerical simulation, conducted with a commercial finite domain time difference (FDTD) tool, Lumerical FDTD solutions. In measurement step, the Fourier images are captured by charge coupled device (CCD) camera for obtaining relative diffraction efficiency at each space. In both simulation and experiment, the polarizers at input are altered, while the output polarizer is excluded for verifying beam splitting ability of proposed scheme. As shown in Figs. 4.10a-c, the experimental result shows a desired operation with preconditioned polarization state of incident light. The total efficiency of reflection and transmission varies with samples and polarizations, which can be found in Table 4.1, obtained by FDTD results. The results show the possibility as novel type PBS, considering the beams divided into both spaces by the input polarization states. For analysis as a polarizing beam splitter, the polarization extinction ratio defined as $\mathrm{PER} = P_{\mathrm{pol.1}} / P_{\mathrm{pol.2}}(\mathrm{dB})$ is also calculated at the desired diffraction order (Fig. 4.10d). In our design, PER can be obtained at both spaces, resulting in two PERs by one sample. At each

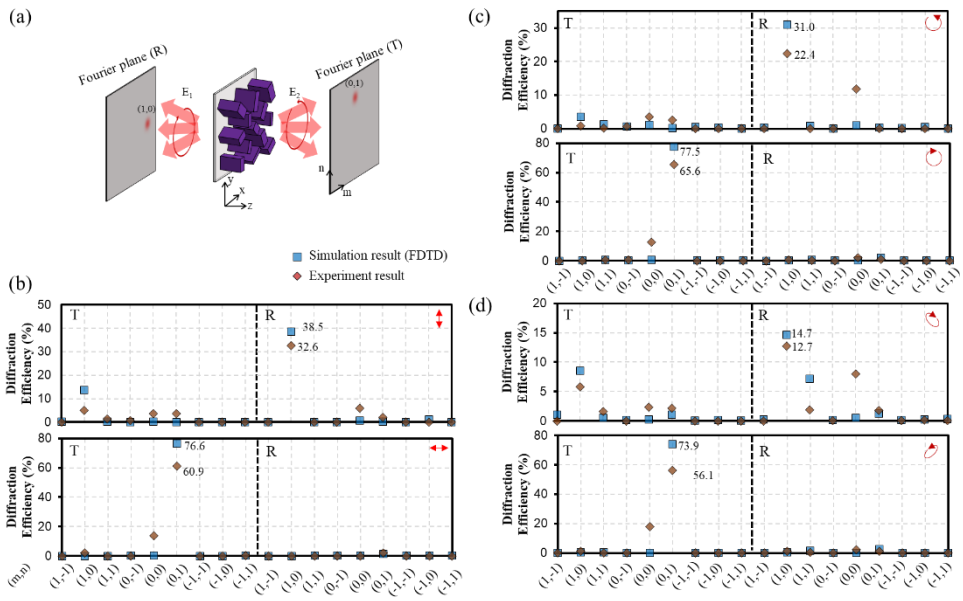

Figure 4.11 Beam deflection schematic diagram and results from simulation and experiment. (a) Schematic diagram showing beam deflection with parameters for diffraction order and polarization states. (b-d) Dot plot showing simulation and experiment result of diffraction order efficiency. (b) is from sample 1, operating in linear polarization pair, (c) from sample 2 operating in circular polarization pair and (d) from sample 3 operating in elliptical polarization pair. Arrows indicate the polarization states of the input light. The written numbers in graph are the diffraction efficiency of desired components. Blue squares are the simulated results and red diamonds are from measured results.

space, $P_{\text{pol.1}}$ and $P_{\text{pol.2}}$ are measured at the same position into which the diffracted beam by the ideal sample propagates. That is, in transmission, the measured position is to $+y$ direction having momentum of $0.444P$. Subscript pol.1 means the wanted polarization state and pol.2 is unwanted state, which is orthogonal to pol.1. For example, in transmission (reflection) mode, when the x(y)-polarized light impinges to sample 1, the efficiency of light which is diffracted to $+y$(x) direction having momentum of $0.444P$ ($0.555P$) is measured, and this is called $P_{\text{pol.1}}$. Next, the input polarization is tuned to y(x)-polarized light, then $P_{\text{pol.2}}$ is measured at the same position as before. We achieved PER of the maximum value up to 16.7 dB at transmission and 27.8

dB at reflection in sample 1. The difference between simulation and experiment is due to the imperfection of the optical elements used in optical setup, and fabrication error of samples. This is notable in that the transmissive metasurface is utilized to send light into reflection spaces by putting local phase gradient. The comparison between simulation and experiment is shown in Fig. 4.11 by the efficiency, showing great agreement with each other. The difference mainly grounds for the inevitable reflection from the substrate, which is shown well in reflection cases at zeroth order.

As the second example for experimental verification, the asymmetric holographic image generation is demonstrated. That is, the holographic image itself as well as the space where it is generated is altered according to the polarization state. Three different samples are fabricated which are distinguished by the operational polarization pair and generated holographic images as well. Fabricated sample is composed of 300×300 pixels, having total 300×300×2 meta-atoms. Two target holographic images are encoded by GS algorithm to be regenerated at the Fourier plane, so as shown in Fig. 4.9a, a lens is put between sample and CCD camera. At encoding step, the image is designed to occupy the area which is determined considering the numerical aperture of Fourier lens used in measurement step in Fig. 4.9a, which is 0.5. In measurement step, the images are captured by CCD camera by changing the polarization state of incident light. The captured images are shown in Figs. 4.12a-c on the right described with input polarization states, and the simulation results are shown on the left. The holograms generated in transmission spaces have the polarization states orthogonal to those of

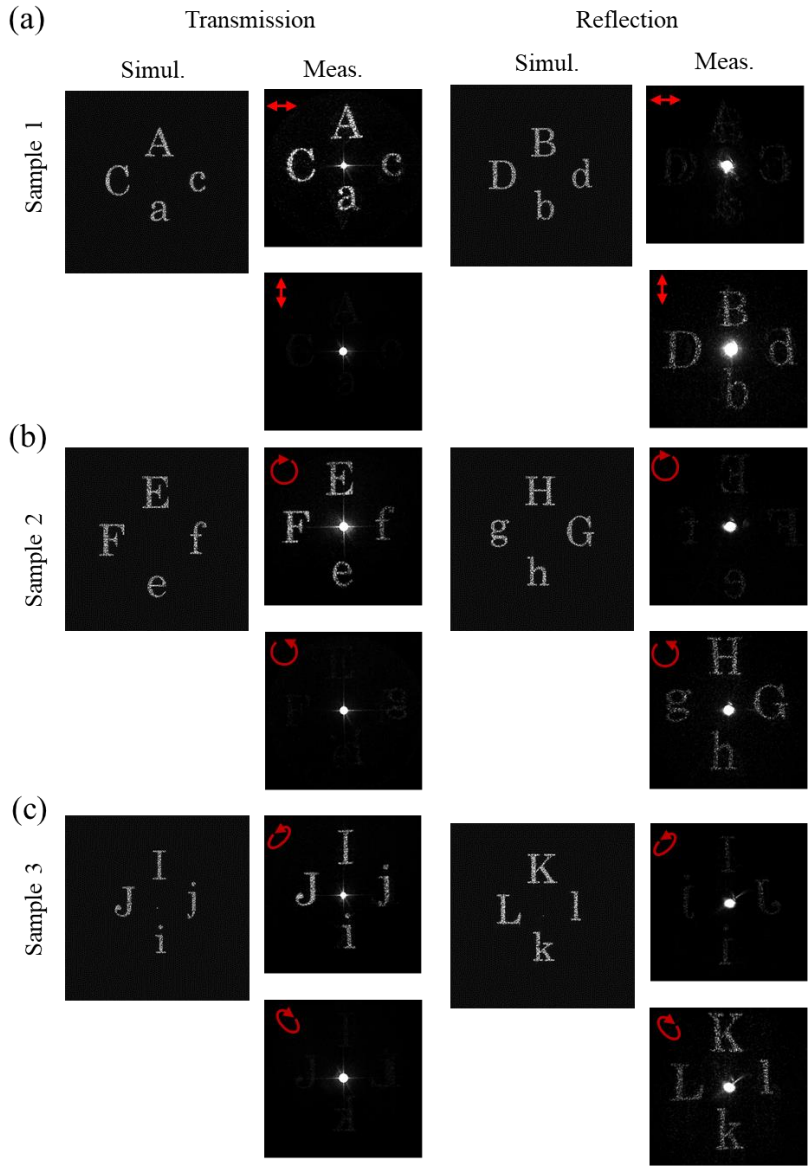

Figure 4.12 Hologram generation results from simulation and measurement. From top to bottom, they operate in (a) linear (sample 1), (b) circular (sample 2), and (c) elliptical (sample 3) polarization states. Arrows indicates how the polarizer is directed at input end.

holographic images in reflection spaces. As shown in the measured results, when the opposite basis of polarized light is incident onto each sample, the holographic images are barely discerned. In terms of the optical power, which is integrated value except for the power at the middle of the resultant image,

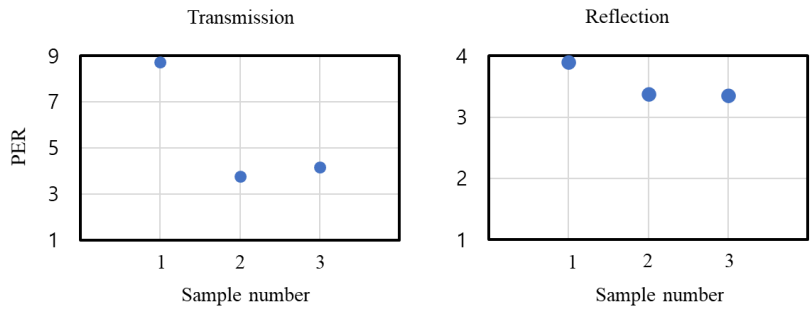

Figure 4.13 Polarization extinction ratio of hologram generation sample

the ratio is calculated by each sample and space. It is determined like PER above by input polarization ($P_{pol.1}/P_{pol.2}$) but not in dB scale (Fig. 4.13). The ER here shows similar trend with the beam steering case. The maximum ratio is achieved at sample 1, which is 8.75 at transmission and 3.902 at reflection. In terms of image generation, the experimental results show the good agreements with the simulation results. The hologram conversion efficiency is calculated numerically, assuming the incident light is plane wave and near-field effect is neglected (Table 2). Considering the zeroth order term that is not found in numerical result, the efficiency of experimental results could be lower than that of simulated result. The main reason of the difference owes to the fabrication error, because the operation of designed metasurface is dependent on the dimensions of the nanopillars. Also, the total beam profile occupies more areas compared to the fabricated sample sizes and this contributes to the increase of zeroth order diffraction.

Table 4.2 Numerically retrieved hologram conversion efficiency

Conversion efficiency (%)	**Sample 1**	**Sample 2**	**Sample 3**
Transmission	80.01	79.87	66.42
Reflection	78.18	79.57	65.79

4.5 Conclusion

In conclusion, the author design and experimentally demonstrate metasurfaces which are capable of controlling the full-space of incident light. Unlike previous studies, the controlled space is flipped by the polarization states of incident light, which is possible by linearly birefringent rectangular nanopillars and integer parity design to realize induced reflection. Transmissive and linearly birefringent nanopillars are employed for distinct phase shift to any pair of orthogonal polarization states, involved with reversed handedness. Two nanopillars are multiplexed into unit cell, and using GSL, critical angle condition with normally incident light is used for mediating reflective operation from transmissive PGM. Next, beam deflection and hologram generation samples are fabricated for experimental verification of proposed scheme. For each operation, three samples operating in linear, circular and elliptical polarization pair are fabricated. They are in good agreements with simulation results, offering their potential to be utilized in various optical applications as novel type PBS. Other than PBS, one can think that the ability to design different beam trajectory according to polarization is comparable with polarization volume grating, composed of liquid crystal. Their diffraction efficiency and polarization contrast could be larger than metasurface, but our scheme has merits in the ultrathin thickness (~λ) and subwavelength pixel pitch. The additional advantage of the proposed scheme with respect to currently employed spatial light modulators is that the proposed scheme is characterized by extremely compact features, and capability of full-space modulation. Furthermore, in terms of vectorial hologram, meaning multichannel hologram generated with various

polarization states, this scheme would be used in demonstration of vectorial holographic images appearing in both spaces, which can be called 360° vectorial hologram. Adding the encryption method of ref. 16 to this scheme would allow the vectorial holographic images to be further encrypted in the generated space. Finally, in terms of applicability, the author expect that this scheme can be more useful in designing novel type optical setups and compatible in various conventional setups, which would result in lightening the weight of optical devices.[64]

Chapter 5 Conclusion

This dissertation presents the studies on improving the metasurface performance into full-space for multifunctionality, especially by independent wavefront control at visible frequency. There have been a lot of studies on metasurfaces regarding full-space control, but they are concentrated on the wavefront control on gigahertz frequency regime, which has a long way to go to be applied in optical frequency. In this regard, for novel form factor with using the whole merits of metasurface for optical engineering, metasurfaces, which enable the independent wavefront control of transmission and reflection, respectively, are newly proposed here. Simultaneous, and often polarization-selective control of full-space can provide the metasurface with the potential to be utilized in novel and existence optical system for reduced form factor. The studies on this dissertation use conventional techniques to control the phases conveyed from meta-atom, but the methodology collaborating them is not ordinary. The structures are designed to be as simple as possible, considering the fidelity of the fabrication result.

First, the simple-structured silicon metasurface is reported for the simultaneous full-space control of light for visible wavelength. For independent phase control at each space, the concept of generalized Kerker effect is proposed, and this is verified both analytically and numerically together. Spatially varied size of rectangular pillar composed of amorphous silicon is adopted as meta-atom, having benefits of well-known nanofabrication feasibility. The proposed scheme is tested by experimental result, applied in asymmetric beam deflection as well as hologram generation.

Thanks to versatility of proposed metasurface, the generalized Snell's law is extended to transmission and reflection together, allowing phase gradient values. Hologram generation is also demonstrated, reinforcing its ability to be employed in further optic applications. The metasurface research is paving its way to consumer electronics and commercial optics applications such as biomedical imaging or augmented reality platform. Researchers are using the metasurface in a way that replaces one part of the bulk optics to keep up with this trend. In this context, considering the versatile nature of proposed method to control both spaces, the scheme presented in this article can be advantageous in further miniaturization and advance in light-weight future devices.

Second, platform having polarization dependent operation that is completely new is presented. Using L-shaped structure as unit, the magnitude variation of cross-polarized component according to the handedness of CP light is achieved. Especially, it is designed so that when right-handed CP light is incident, cross-polarized transmission is suppressed, and when left-handed CP light is used as excitation light source, cross-polarized reflection becomes zero. Using geometric phase and interleaving it with enantiomeric counterpart, independent phase control at transmission and reflection is achieved. Notably, as novel operation, by handedness change of incident CP light, the transmitted phase profile can be transferred to reflection space and at the same time, the reflected phase goes to transmission, which is called space conversion. Using asymmetric beam deflection and holographic image generation, the unique property of proposed metasurface is presented. Also, by polarization change of incident light, the space conversion is verified experimentally. We are

expecting this scheme can contribute to the suggestion of new form factor in existent optical design by virtue of novel operation.

Thirdly, the author designs and experimentally demonstrates metasurfaces which are capable of controlling the full-space of incident light. Unlike previous studies, the controlled space is flipped by the polarization states of incident light, which is possible by linearly birefringent rectangular nanopillars and integer parity design to realize induced reflection. Transmissive and linearly birefringent nanopillars are employed for distinct phase shift to any pair of orthogonal polarization states, involved with reversed handedness. Two nanopillars are multiplexed into unit cell, and using GSL, critical angle condition with normally incident light is used for mediating reflective operation from transmissive PGM. Next, beam deflection and hologram generation samples are fabricated for experimental verification of proposed scheme. For each operation, three samples operating in linear, circular and elliptical polarization pair are fabricated. They are in good agreements with simulation results, offering their potential to be utilized in various optical applications as novel type PBS.

In summary, the author proposed methodologies to make platform achieving independent wavefront control in transmission and reflection spaces, respectively. Despite the novelty of these studies, however, there are still several problems to be dealt with for application to future optic devices. First, the benefits of controlling both spaces at the same time are still ambiguous. Among the proposed studies in this dissertation, only Chapter 4 can be replaced by surpassing the existing PBS, and further studies for application of the remaining platforms of Chapter 2 and 3 should be

conducted in the future. Second, there exist several problems on Chapter 2 and 3, such as efficiency and polarization. In terms of efficiency, due to the limit of silicon in visible wavelength, the performance is severely low, which is about 40% and 50% in maximum, respectively. Also, they need polarizer at input and output end simultaneously. It can affect (increase) the volume of the entire system when the corresponding platforms are applied, and the form factor can increase despite the use of metasurfaces.

In future studies, when designing a device where efficiency is important, it is necessary to be able to control the efficiency between the reflected light and the transmitted light. In Chapter 2, the portion of transmitted and reflected light is randomly chosen, but this factor is crucial in real-life device so fine-tuning the balance is necessary. Considering the abovementioned problems, development in terms of efficiency is essential so that the polarizer can be removed. This is because the need for a polarizer may also disappear if it can have high performance in efficiency. Not only this, but it would be better if we could design it to work with different polarization pairs for Chapters 2 and 3. Like platform proposed in Chapter 4, free choice of polarization pair will accelerate the application of full-space metasurface to optic systems. In terms of application, demonstrations rather than beam deflection and holographic image generation are required. Only for operational test and consistency, these two identical experimental demonstrations are conducted throughout this dissertation. However, the demonstration that may attract research groups exists such as 360° vectorial holograms (Chapter 4) since it was never possible with conventional platforms. Especially for Chapter 3 of L-shaped meta-atom, since the concept of space conversion is new, the more intriguing

experimental demonstration with improved performance may pave the way to design novel modulation platform with metasurfaces. The platform of Chapter 4 was designed in 980 nm wavelength, which is not the visible light band, but this could be designed to easily operate in the visible light band when simply replaced with a material with a low absorption rate in corresponded wavelength as mentioned in that chapter.

Bibliography

1. H. T. Chen, A. J. Taylor, and N. Yu, "A review of metasurfaces: physics and applications," *Rep Prog Phys* **79**, 076401 (2016).
2. S. M. Kamali, E. Arbabi, A. Arbabi, and A. Faraon, "A review of dielectric optical metasurfaces for wavefront control," *Nanophotonics* **7**, 1041-1068 (2018).
3. L. Zhang, S. Mei, K. Huang, and C.-W. Qiu, "Advances in Full Control of Electromagnetic Waves with Metasurfaces," *Adv. Opt. Mater.* **4**, 818-833 (2016).
4. H.-H. Hsiao, C. H. Chu, and D. P. Tsai, "Fundamentals and Applications of Metasurfaces," *Small Methods* **1,** 1600064 (2017).
5. G. Y. Lee, J. Sung, and B. Lee, "Recent advances in metasurface hologram technologies," *ETRI Journal* **41**, 10-22 (2019).
6. M. Chen, M. Kim, A. M. H. Wong, and G. V. Eleftheriades, "Huygens' metasurfaces from microwaves to optics: a review," *Nanophotonics* **7**, 1207-1231 (2018).
7. S. B. Glybovski, S. A. Tretyakov, P. A. Belov, Y. S. Kivshar, and C. R. Simovski, "Metasurfaces: From microwaves to visible," *Physics Reports* **634**, 1-72 (2016).
8. V. C. Su, C. H. Chu, G. Sun, and D. P. Tsai, "Advances in optical metasurfaces: fabrication and applications," *Opt. Express* **26**, 13148-13182 (2018).
9. A. She, S. Zhang, S. Shian, D. R. Clarke, and F. Capasso, "Large area metalenses: design, characterization, and mass manufacturing," *Opt. Express* **26**, 1573-1585 (2018).
10. I. Kim, G. Yoon, J. Jang, P. Genevet, K. T. Nam, and J. Rho, "Outfitting Next Generation Displays with Optical Metasurfaces," *ACS Photonics* **5**, 3876-3895 (2018).
11. Z. Li, E. Palacios, S. Butun, and K. Aydin, "Visible-frequency metasurfaces for broadband anomalous reflection and high-efficiency spectrum splitting," *Nano Lett.* **15**, 1615-1621 (2015).
12. X. Ni, A. V. Kildishev, and V. M. Shalaev, "Metasurface holograms for visible light," *Nat. Commun.* **4**, 1-6 (2013).
13. G. Y. Lee, G. Yoon, S. Y. Lee, H. Yun, J. Cho, K. Lee, H. Kim, J. Rho, and B. Lee, "Complete amplitude and phase control of light using broadband holographic metasurfaces," *Nanoscale* **10**, 4237-4245 (2018).
14. D. Lin, P. Fan, E. Hasman, and M. L. Brongersma, "Dielectric gradient metasurface optical elements," *Science* **345**, 298-302 (2014).

15. M. Khorasaninejad, W. T. Chen, R. C. Devlin, J. Oh, A. Y. Zhu, and F. Capasso, "Metalenses at visible wavelengths: Diffraction-limited focusing and subwavelength resolution imaging," *Science* **352**, 1190-1194 (2016).
16. S. Wang, P. C. Wu, V.-C. Su, Y.-C. Lai, M.-K. Chen, H. Y. Kuo, B. H. Chen, Y. H. Chen, T.-T. Huang, J.-H. Wang, R.-M. Lin, C.-H. Kuan, T. Li, Z. Wang, S. Zhu, and D. P. Tsai, "A broadband achromatic metalens in the visible," *Nat. Nanotechnol.* **13**, 227-232 (2018).
17. W. T. Chen, A. Y. Zhu, V. Sanjeev, M. Khorasaninejad, Z. Shi, E. Lee, and F. Capasso, "A broadband achromatic metalens for focusing and imaging in the visible," *Nat. Nanotechnol.* **13**, 220-226 (2018).
18. B. Wang, F. Dong, Q. T. Li, D. Yang, C. Sun, J. Chen, Z. Song, L. Xu, W. Chu, Y. F. Xiao, Q. Gong, and Y. Li, "Visible-Frequency Dielectric Metasurfaces for Multiwavelength Achromatic and Highly Dispersive Holograms," *Nano Lett.* **16**, 5235-5240 (2016).
19. E. Maguid, I. Yulevich, M. Yannai, V. Kleiner, L. B. M, and E. Hasman, "Multifunctional interleaved geometric-phase dielectric metasurfaces," *Light Sci. Appl.* **6**, e17027 (2017).
20. D. Wen, F. Yue, G. Li, G. Zheng, K. Chan, S. Chen, M. Chen, K. F. Li, P. W. Wong, K. W. Cheah, E. Y. Pun, S. Zhang, and X. Chen, "Helicity multiplexed broadband metasurface holograms," *Nat. Commun.* **6**, 8241 (2015).
21. J. P. Balthasar Mueller, N. A. Rubin, R. C. Devlin, B. Groever, and F. Capasso, "Metasurface Polarization Optics: Independent Phase Control of Arbitrary Orthogonal States of Polarization," *Phys. Rev. Lett.* **118**, 113901 (2017).
22. E. Arbabi, A. Arbabi, S. M. Kamali, Y. Horie, and A. Faraon, "Controlling the sign of chromatic dispersion in diffractive optics with dielectric metasurfaces," *Optica* **4,** 625-632 (2017).
23. M. Jang, Y. Horie, A. Shibukawa, J. Brake, Y. Liu, S. M. Kamali, A. Arbabi, H. Ruan, A. Faraon, and C. Yang, "Wavefront shaping with disorder-engineered metasurfaces," *Nat Photonics* **12**, 84-90 (2018).
24. S. W. Tang, T. Cai, H. X. Xu, Q. He, S. L. Sun, and L. Zhou, "Multifunctional Metasurfaces Based on the "Merging" Concept and Anisotropic Single-Structure Meta-Atoms," *Appl. Sci.-Basel.* **8,** 555 (2018).
25. S. Chen, W. Liu, Z. Li, H. Cheng, and J. Tian, "Metasurface-Empowered Optical Multiplexing and Multifunction," *Adv. Mater.* **32**, e1805912 (2020).

26. S. M. Kamali, E. Arbabi, A. Arbabi, Y. Horie, M. Faraji-Dana, and A. Faraon, "Angle-Multiplexed Metasurfaces: Encoding Independent Wavefronts in a Single Metasurface under Different Illumination Angles," *Phys. Rev. X* **7**(2017).
27. A. Leitis, A. Tittl, M. Liu, B. H. Lee, M. B. Gu, Y. S. Kivshar, and H. Altug, "Angle-multiplexed all-dielectric metasurfaces for broadband molecular fingerprint retrieval," *Sci. Adv.* **5**, eaaw2871 (2019).
28. A. Arbabi, Y. Horie, M. Bagheri, and A. Faraon, "Dielectric metasurfaces for complete control of phase and polarization with subwavelength spatial resolution and high transmission," *Nat. Nanotechnol.* **10**, 937-943 (2015).
29. A. Arbabi, Y. Horie, A. J. Ball, M. Bagheri, and A. Faraon, "Subwavelength-thick lenses with high numerical apertures and large efficiency based on high-contrast transmitarrays," *Nat. Commun.* **6**, 7069 (2015).
30. E. Arbabi, A. Arbabi, S. M. Kamali, Y. Horie, and A. Faraon, "Multiwavelength polarization-insensitive lenses based on dielectric metasurfaces with meta-molecules," *Optica* **3**, 628-633 (2016).
31. K. E. Chong, L. Wang, I. Staude, A. R. James, J. Dominguez, S. Liu, G. S. Subramania, M. Decker, D. N. Neshev, I. Brener, and Y. S. Kiyshar, "Efficient Polarization-Insensitive Complex Wavefront Control Using Huygens' Metasurfaces Based on Dielectric Resonant Meta-atoms," *ACS Photonics* **3**, 514-519 (2016).
32. L. Jin, Z. Dong, S. Mei, Y. F. Yu, Z. Wei, Z. Pan, S. D. Rezaei, X. Li, A. I. Kuznetsov, Y. S. Kivshar, J. K. W. Yang, and C. W. Qiu, "Noninterleaved Metasurface for (2^6-1) Spin- and Wavelength-Encoded Holograms," *Nano Lett.* **18**, 8016-8024 (2018).
33. X. Li, L. Chen, Y. Li, X. Zhang, M. Pu, Z. Zhao, X. Ma, Y. Wang, M. Hong, and X. Luo, "Multicolor 3D meta-holography by broadband plasmonic modulation," *Sci. Adv.* **2**, e1601102 (2016).
34. S. Gao, C. S. Park, C. Zhou, S. S. Lee, and D. Y. Choi, "Twofold Polarization-Selective All-Dielectric Trifoci Metalens for Linearly Polarized Visible Light," *Adv. Opt. Mater.* **7**(2019).
35. R. Zhao, B. Sain, Q. Wei, C. Tang, X. Li, T. Weiss, L. Huang, Y. Wang, and T. Zentgraf, "Multichannel vectorial holographic display and encryption," *Light Sci. Appl.* **7**, 95 (2018).
36. R. Mao, G. Wang, T. Cai, K. Liu, D. Wang, and B. Wu, "Ultra-thin and high-efficiency full-space Pancharatnam-Berry metasurface," *Opt. Express* **28**, 31216-31225 (2020).
37. L. Zhang, R. Y. Wu, G. D. Bai, H. T. Wu, Q. Ma, X. Q. Chen, and T. J. Cui, "Transmission-Reflection-Integrated Multifunctional

Coding Metasurface for Full-Space Controls of Electromagnetic Waves," *Adv. Funct. Mater.* **28**(2018).
38. J. Sung, G. Y. Lee, C. Choi, J. Hong, and B. Lee, "Single-Layer Bifacial Metasurface: Full-Space Visible Light Control," *Adv. Opt. Mater.* **7**, 1801748 (2019).
39. S. J. Kim, I. Kim, S. Choi, H. Yoon, C. Kim, Y. Lee, C. Choi, J. Son, Y. W. Lee, J. Rho, and B. Lee, "Reconfigurable all-dielectric Fano metasurfaces for strong full-space intensity modulation of visible light," *Nanoscale Horiz.* **5**, 1088-1095 (2020).
40. J. Sung, G. Y. Lee, C. Choi, J. Hong, and B. Lee, "Polarization-dependent asymmetric transmission using a bifacial metasurface," *Nanoscale Horiz.* **5**, 1487-1495 (2020).
41. J. P. Fan, Y. Z. Cheng, and B. He, "High-efficiency ultrathin terahertz geometric metasurface for full-space wavefront manipulation at two frequencies," *J. Phys. D* **54,** 115101 (2021).
42. T. Cai, G. M. Wang, S. W. Tang, H. X. Xu, J. W. Duan, H. J. Guo, F. X. Guan, S. L. Sun, Q. He, and L. Zhou, "High-Efficiency and Full-Space Manipulation of Electromagnetic Wave Fronts with Metasurfaces," *Phys. Rev. Appl.* **8,** 034033 (2017).
43. C. B. Zhang, G. M. Wang, H. X. Xu, X. Zhang, and H. P. Li, "Helicity-Dependent Multifunctional Metasurfaces for Full-Space Wave Control," *Adv. Opt. Mater.* **8,** 1901719 (2020).
44. H. Hou, G. Wang, H. Li, W. Guo, and T. Cai, "Helicity-dependent metasurfaces employing receiver-transmitter meta-atoms for full-space wavefront manipulation," *Opt. Express* **28**, 27575-27587 (2020).
45. G. Zheng, N. Zhou, L. Deng, G. Li, J. Tao, and Z. Li, "Full-space metasurface holograms in the visible range," *Opt. Express* **29**, 2920-2930 (2021).
46. Z. Li, Q. Dai, M. Q. Mehmood, G. Hu, B. L. Yanchuk, J. Tao, C. Hao, I. Kim, H. Jeong, G. Zheng, S. Yu, A. Alu, J. Rho, and C. W. Qiu, "Full-space Cloud of Random Points with a Scrambling Metasurface," *Light Sci. Appl.* **7**, 63 (2018).
47. J. Yang, X. Wu, J. Song, C. Huang, Y. Huang, and X. Luo, "Cascaded metasurface for simultaneous control of transmission and reflection," *Opt. Express* **27**, 9061-9070 (2019).
48. F. Zhang, M. B. Pu, X. Li, P. Gao, X. L. Ma, J. Luo, H. L. Yu, and X. G. Luo, "All-Dielectric Metasurfaces for Simultaneous Giant Circular Asymmetric Transmission and Wavefront Shaping Based on Asymmetric Photonic Spin-Orbit Interactions," *Adv. Funct. Mater*. **27,** 1704295(2017).

49. X. H. Zhang, M. B. Pu, Y. H. Guo, J. J. Jin, X. Li, X. L. Ma, J. Luo, C. T. Wang, and X. G. Luo, "Colorful Metahologram with Independently Controlled Images in Transmission and Reflection Spaces," *Adv. Funct. Mater.* **29,** 1809145 (2019).
50. M. Kerker, D. S. Wang, and C. L. Giles, "Electromagnetic scattering by magnetic spheres," *J. Opt. Soc. Am.* **73,** 765-767 (1983).
51. J. D. Jackson, "Classical electrodynamics," Wiley, New York, (1975).
52. W. Liu and Y. S. Kivshar, "Generalized Kerker effects in nanophotonics and meta-optics," *Opt. express* **26**, 13085-13105 (2018).
53. W. Liu and Y. S. Kivshar, "Multipolar interference effects in nanophotonics," *Philos. Trans. A Math Phys. Eng. Sci.* **375**, 20160317 (2017).
54. S. Kruk and Y. Kivshar, "Functional Meta-Optics and Nanophotonics Governed by Mie Resonances," *ACS Photonics* **4**, 2638-2649 (2017).
55. A. I. Kuznetsov, A. E. Miroshnichenko, Y. H. Fu, J. Zhang, and B. Luk'Yanchuk, "Magnetic light," *Sci. rep.* **2**, 1-6 (2012).
56. H. Wang, P. Liu, Y. Ke, Y. Su, L. Zhang, N. Xu, S. Deng, and H. Chen, "Janus magneto–electric nanosphere dimers exhibiting unidirectional visible light scattering and strong electromagnetic field enhancement," *ACS nano* **9**, 436-448 (2015).
57. L. Wei, A. E. Miroshnichenko, and Y. S. Kivshar, "Control of light scattering by nanoparticles with optically-induced magnetic responses," *Chin. Phys. B* **23**, 047806 (2014).
58. R. W. Ziolkowski, "Using Huygens multipole arrays to realize unidirectional needle-like radiation," *Phys Rev X* **7**, 031017 (2017).
59. M. Decker, I. Staude, M. Falkner, J. Dominguez, D. N. Neshev, I. Brener, T. Pertsch, and Y. S. Kivshar, "High-efficiency dielectric Huygens' surfaces," *Adv. Opt. Mater.* **3**, 813-820 (2015).
60. J. Li, N. Verellen, D. Vercruysse, T. Bearda, L. Lagae, and P. Van Dorpe, "All-dielectric antenna wavelength router with bidirectional scattering of visible light," *Nano lett* **16**, 4396-4403 (2016).
61. S. Kruk, B. Hopkins, I. I. Kravchenko, A. Miroshnichenko, D. N. Neshev, and Y. S. Kivshar, "Invited Article: Broadband highly efficient dielectric metadevices for polarization control," *APL Photonics* **1**, 030801 (2016).
62. W. Liu and A. E. Miroshnichenko, "Beam steering with dielectric metalattices," *ACS Photonics* **5**, 1733-1741 (2017).

63. P. Grahn, A. Shevchenko, and M. Kaivola, "Electromagnetic multipole theory for optical nanomaterials," *New J. Phys.* **14**, 093033 (2012).
64. G.-Y. Lee, J.-Y. Hong, S. Hwang, S. Moon, H. Kang, S. Jeon, H. Kim, J.-H. Jeong, and B. Lee, "Metasurface eyepiece for augmented reality," *Nat commun* **9**, 1-10 (2018).
65. C. Menzel, C. Rockstuhl, and F. Lederer, "Advanced Jones calculus for the classification of periodic metamaterials," *Phys Rev A* **82**, 053811 (2010).
66. V. Savinov, V. Fedotov, and N. I. Zheludev, "Toroidal dipolar excitation and macroscopic electromagnetic properties of metamaterials," *Phys Rev B* **89**, 205112 (2014).
67. S. Sun, K.-Y. Yang, C.-M. Wang, T.-K. Juan, W. T. Chen, C. Y. Liao, Q. He, S. Xiao, W.-T. Kung, and G.-Y. Guo, "High-efficiency broadband anomalous reflection by gradient meta-surfaces," *Nano lett.* **12**, 6223-6229 (2012).
68. F. Ding, A. Pors, and S. I. Bozhevolnyi, "Gradient metasurfaces: a review of fundamentals and applications," *Rep. Prog. Phys.* **81**, 026401 (2017).
69. Z. Li, M.-H. Kim, C. Wang, Z. Han, S. Shrestha, A. C. Overvig, M. Lu, A. Stein, A. M. Agarwal, and M. Lončar, "Controlling propagation and coupling of waveguide modes using phase-gradient metasurfaces," *Nat. Nanotechnol.* **12**, 675 (2017).
70. N. Yu, P. Genevet, M. A. Kats, F. Aieta, J.-P. Tetienne, F. Capasso, and Z. Gaburro, "Light propagation with phase discontinuities: generalized laws of reflection and refraction," *Science* **334**, 333-337 (2011).
71. C. Shen and S. A. Cummer, "Harnessing multiple internal reflections to design highly absorptive acoustic metasurfaces," *Phys. Rev. Appl.* **9**, 054009 (2018).
72. Y. Cao, Y. Fu, Q. Zhou, X. Ou, L. Gao, H. Chen, and Y. Xu, "Mechanism behind angularly asymmetric diffraction in phase-gradient metasurfaces," *Phys. Rev. Appl.* **12**, 024006 (2019).
73. Y. Fu, C. Shen, Y. Cao, L. Gao, H. Chen, C. T. Chan, S. A. Cummer, and Y. Xu, "Reversal of transmission and reflection based on acoustic metagratings with integer parity design," *Nat. commun.* **10**, 1-8 (2019).
74. Y. Fu, Y. Cao, and Y. Xu, "Multifunctional reflection in acoustic metagratings with simplified design," *Appl. Phys. Lett.* **114**, 053502 (2019).
75. S. Zhu, Y. Cao, Y. Fu, X. Li, L. Gao, H. Chen, and Y. Xu, "Switchable bifunctional metasurfaces: nearly perfect retroreflection

and absorption at the terahertz regime," *Opt. Lett*. **45**, 3989-3992 (2020).
76. Y.-Y. Fu, J.-Q. Tao, A.-L. Song, Y.-W. Liu, and Y.-D. Xu, "Controllably asymmetric beam splitting via gap-induced diffraction channel transition in dual-layer binary metagratings," *Front. Phys.* **15**, 1-6 (2020).

Appendix

Portions of the work discussed in this dissertation were also presented in the following publications:

[Chapter 2] J. Sung, G. Y. Lee, C. Choi, J. Hong, and B. Lee, "Single-Layer Bifacial Metasurface: Full-Space Visible Light Control," *Advanced Optical Materials* **7**, 1801748 (2019).

[Chapter 4] J. Sung, G. Y. Lee, C. Choi, J. Hong, and B. Lee, "Polarization-dependent asymmetric transmission using a bifacial metasurface," *Nanoscale Horizons* **5**, 1487-1495 (2020).

초 록

메타표면은 다양한 주파수 영역에서 빛의 전자기적 특성을 자유롭게 조절할 수 있다는 고유한 능력 덕분에 많은 관심을 받았습니다. 최근 반도체 공정의 발전에 힘입어, 메타표면을 통해 가시광선 대역에서 기존의 광학 장치를 능가하는 전례 없는 독특하고도 성능이 월등한 광 제어가 제안되었습니다. 또한 메타표면은 평면형 폼 팩터라는 장점까지 있으므로 사용될 경우 전체 광학 시스템에서 무게 및 부피를 줄일 수 있는 미래형 광학 소자로 여겨집니다. 현재의 웨어러블 기기와 스마트 기기는 더 가볍고 더 나은 광학 부품을 필요로 한다는 점을 감안할 때 미래의 광학 기기에 대해 메타표면이 없이 이야기할 수 없다고 해도 과언이 아닙니다.

이와 관련하여 이 박사 논문에서는 투과 및 반사 공간을 모두 제어하도록 설계된 독특한 메타 표면을 제시합니다. 투과 또는 반사된 빛만 고려하는 기존의 메타 표면과 비교하여 제안된 플랫폼은 메타 표면의 정보 용량을 전체 공간으로 향상시킵니다. 이는 메타표면 설계와 시스템 설계에서도 새로운 패러다임을 제공할 수 있음을 의미합니다. 직관적인 관점과는 달리 단층 및 단순한 구조로 제작된 메타 표면을 통해 전 공간으로 산란되는 광 제어, 특히 그 중에서도 파면 조절을 위한 위상 제어를 할 수 있도록 설계되었습니다.

이 논문에서는 총 세 가지 유형의 메타 표면이 제안안됩니다. 첫 번째로, 메타표면에 빛이 입사하였을 때에 투과 및 반사되는 빛을 동시에 조절할 수 있는 플랫폼이 제안되었습니다. 물리적인 기반으로서 Multipole interference 및 Pancharatnam–Berry 위상을 통해 어떤 원리로 이것이 가능한 지 설명되었습니다. 기능 검증의 예시로 비대칭적으로 빔이 꺾이는 현상과 투과 및 반사 공간에 서로 다른 홀로그램을 생성하는 현상을 실험적으로 측정하였습니다. 알려진 한, 이것은 가시 광선 대역에서 독립적 위상 제어를 달성한 최초의 연구입니다.

두 번째로, L 자형 메타 원자로 구성된 메타 표면 플랫폼이 제시됩니다. L 자 메타 표면은 이전 챕터의 플랫폼처럼 Pancharatnam–Berry 위상에 의해 작동하도록 설계되었으며 투과 및 반사 방향으로 서로 다른 위상 값을 전달합니다. 또한 입사되는 빛이 원 편광일 때에 그 스핀 방향을 바꾸면 투과와 반사 공간 쪽으로 전달되는 위상이 서로 반전되도록 설계되었습니다. 이는 이전에 제안된 적이 없는 새로운 형태의 광 조절 플랫폼이라는 점에서 의미가 있습니다. 이 역시 공정 및 실험을 통한 검증을 전과 같은 방법으로 진행했습니다.

마지막으로 임의의 편광 짝을 지정하였을 때, 입사되는 편광에 따라서 투과될 지 반사될 지 사용자가 결정할 수 있는 메타표면 플랫폼이 제안되었습니다. 직사각형 나노 기둥이 메타 원자로 활용되었는데, 이를 사용하여 어떠한 편광 짝에 대해서도

원하는 동작이 가능하도록 설계되었습니다. 설계된 투과형 메타표면을 기반으로 하여, 임계각 조건에서 유도 반사되는 현상을 활용해 한 쪽 편광에서만 반사형 동작을 유도하여 제안된 동작을 실현했습니다. 제안된 방식으로는 편광 짝을 마음대로 선택할 수 있으므로, 선 편광, 원 편광, 타원 편광에 대해 동작할 수 있는 서로 다른 세 가지 샘플을 제작하여 실험적으로 검증도 마쳤습니다.

결론적으로 제안된 메타표면 플랫폼을 통해서 기존 광학 장치로 불가능한 제어 방법을 제안하였으며, 전 공간으로 메타표면의 정보량을 늘렸습니다. 양면형 메타표면을 통해서 새로운 광학 시스템의 패러다임이 제안될 수 있으며, 다기능성 측면에서도 새로운 연구로 활용될 수 있을 것으로 기대됩니다.

주요어 : 메타표면, 전공간 제어, 위상 조절, 나노구조체, 공간 반전, 편광 제어

학 번 : 2016-20921